

UNIVERSITY OF CALIFORNIA

Santa Barbara

Solid-State NMR Analysis of the Surfaces and Interfaces in Nanoscale Materials

A Dissertation submitted in partial satisfaction of the
requirements for the degree Doctor of Philosophy
in Organic Materials Chemistry

by

Mia G. Berrettini

Committee in charge:

Professor Geoffrey F. Strouse

Professor Guillermo Bazan, Chair

Professor William Kaska

Professor Nicola Spaldin

June 2005

The dissertation of Mia G. Berrettini is approved.

Professor Geoffrey F. Strouse

Professor William Kaska

Professor Nicola Spaldin

Professor Guillermo Bazan, Committee Chair

June 2005

Solid-State NMR Analysis of the Surfaces and Interfaces in Nanoscale Materials

Copyright © 2005

by

Mia G. Berrettini

ACKNOWLEDGEMENTS

I would to thank and acknowledge many of my colleagues and professors at UCSB. To begin, I would like to acknowledge Dr. Jerry Hu and Professor Brad Chmelka for inspiring and teaching me so much knowledge of NMR. I would like to thank Christina Raab and Gary Braun for being so wonderful to work and collaborate with and also good friends. From my research group, I would like to give a special thanks to Melissa Fisher, Artjay Javier, Travis Jennings, and Daniel Neuman for their support and friendship throughout the years. To my research advisor, Professor Geoff Strouse: These last four years have been some of the most life-changing years I could ever imagine. I could never possibly thank you enough for everything you have done for me intellectually and personally, as a mentor and a friend, allowing and preparing me for the type of career and life I never imagined possible. Thank you for believing in me.

I would also like send my deepest love and thanks to my family and friends for being so wonderful and supportive. Special thanks to my friends Carolyn Selenski, Bree Guerrero, Jay Schweitzer, Dave Lopez, and Deric Esquivel for all the laughs, memories, and love throughout the years. Thanks to my grandparents, my sister, and my Dad. I would also like to give a special thanks to the entire Nylund family for their kindness, love and support during a time when I needed it the most. And to my Mom, thank you so much for your love, support and being the best role model I could ask for.

Vita of Mia G. Berrettini

Research Interests:

Main Field: Materials Chemistry, Analytical Chemistry

Research Interests: Synthesis, surface engineering, and solid-state NMR analysis of metal and semiconductor materials at the nanoscale.

Education:

Ph.D, Organic Materials Chemistry **Spring 2005 (expected)**

Thesis Title: “*Solid-state NMR Analysis of the Surfaces and Interfaces in Nanoscale Materials*”

University of California, Santa Barbara

Advisor: Professor Geoffrey F. Strouse

B.S. Chemistry

December 1999

Sonoma State University

Magna cum laude with Distinction

Undergraduate research: Synthetic Organic Chemistry, Santa Clara University; Advisor: Professor John D. Thoburn

Experience:

Graduate Research (MC-CAM), UCSB 1/01-present

Supervisor/mentor for undergraduate researchers: Material Research Laboratory Internship Program 2002-2003.

Teaching Assistant, UCSB, 9/00-6/02

Undergraduate Research, Santa Clara University, Summer 1998

Awards:

Presidential Scholarship, 1995

Thermochem Scholarship, 1998

SSU Chemistry Scholarship, 1997, 1998

The Mitsubishi Chemical Center for Advanced Materials Distinguished Graduate Fellow 2002–2003

Brython Davis Endowment Graduate Fellowship 2003-2004

Publications:

- 1) "Synthesis and Characterization of a 1:6 Au: CdSe Nano-composite." Cumberland, S.L.; Berrettini, M.G.; Strouse, G.F. *Chem. Mater.*, **2003**, *15*, 1047-1056.
- 2) "NMR Analysis of Surfaces and Interfaces in 2nm CdSe Nanocrystals" Berrettini, M.G.; Braun, G.; Hu, J.G; Strouse, G.F, *J. Am. Chem. Soc.*, **2004** 126(22); 7063-7070.
- 3) "Size-Dependent ⁷⁷Se NMR Study of CdSe Nanocrystals" Berrettini, M.G.; Strouse, G.F, *manuscript in preparation*.
- 4) "Structural Characterization of InGaP Nanocrystals" Berrettini, M.G.; Raab C.; Chmelka B.; Strouse, G.F. *manuscript in preparation*.

Presentations:

- 1) "Structural Characterization of InGaP Nanocrystals by Solid-State NMR Techniques" Berrettini, M.G.; Raab C.; Gerbec J.; Chmelka B.; Strouse, G.F., National American Chemical Society Meeting, Philadelphia, PA. August 2004.
- 2) "NMR Analysis of Surfaces and Interfaces in 2nm CdSe Nanocrystals" Berrettini, M.G.; Braun, G.; Hu, J.G; Strouse, G.F., National American Chemical Society Meeting, Anaheim, CA. April 2004.
- 3) "NMR Analysis of 2nm CdSe Nanocrystals" Berrettini, M.G.; Strouse, G.F, Southern California Users of Magnets Conference (SCUM), Pomona, CA, October 2003.
- 4) " Ion Assembly of CdSe Quantum Dots." Mia Berrettini, Geoffrey F. Strouse. SCIP conference, Catalina Island, June 2001.
- 5) "Synthesis of 3,7-Diazatricyclo[4.1.0.0_{2,4}]heptane." Mia Berrettini, John. D Thoburn. Undergraduate ACS Meeting, Santa Clara, May 1999

ABSTRACT

Solid-State NMR Analysis of the Surfaces and Interfaces in Nanoscale Materials

By

Mia G. Berrettini

Semiconductor nanocrystals, with unique size-dependent properties, give promise for successful innovation of new technologies including solid-state lighting and biological labeling. Therefore, characterization of the surfaces, interfaces and associated reconstruction in these materials becomes crucial for an understanding of structure-function relationships essential to this development. In this dissertation, powerful solid-state nuclear magnetic resonance (NMR) techniques, such as cross-polarization magic angle spinning (CPMAS), spin-echo, and two dimensional (2D) heteronuclear chemical shift correlation (HETCOR) experiments are utilized to probe these various regions in CdSe and InGaP nanocrystals. These experiments reveal fundamental structural information, including insight into atomic vacancies, discrete particle reconstruction with size, oxidation, passivation, and the nature and molecular order of the surface, near surface and core species. This knowledge gives rise to valuable direct correlations of the structural molecular models of reconstruction with the physical properties of CdSe and InGaP nanomaterials.

Table of Contents.

Chapter 1. Introduction.

1.1. Overview of Nanocrystal Regions and Reconstruction.....	1
1.2. NMR Pulse Techniques for Selective Analysis of Nanocrystal Regions.....	4
1.3. References.....	8

Chapter 2. NMR Characterization of the Surface Passivation in CdSe Nanocrystals

2.1. Introduction.....	13
2.2. Experimental Section.....	15
2.2.1. Synthesis of CdSe Nanocrystals (CdSe-HDA).....	15
2.2.2. Ligand Exchange with 2,4-Difluorothiophenol.....	15
2.2.3. Preparation of Water Soluble CdSe (CdSe-AET).....	16
2.2.4. NMR.....	17
2.3. Results and Discussion.....	18
2.3.1. Surface Passivation of CdSe-HDA.....	18
2.3.2. Thiophenol and HDA Proximities.....	22
2.3.3. Ligand Exchange with 2,4-difluorothiophenol.....	24
2.3.4. Ligand Exchange to produce Water Soluble CdSe (CdSe-AET).....	26
2.4. Conclusions.....	30
2.5. References.....	31

Chapter 3. NMR Analysis of Surfaces and Interfaces in 2-nm CdSe.

3.1. Introduction.....	34
3.2. Experimental Section.....	35
3.2.1. Synthesis of 2-nm CdSe Nanocrystals (CdSe-HDA).....	35
3.2.2. NMR.....	35
3.3. Results and Discussion.....	36
3.3.1. Cadmium and Selenium Surface Structure.....	36
3.3.2. Thiophenol vs HDA Site Occupation.....	48
3.3.3. Structural Model.....	51
3.4. Conclusions.....	54
3.5. References.....	55

Chapter 4. Size-Dependent Solid-State ⁷⁷Se NMR Study of CdSe Nanocrystals.

4.1. Introduction.....	57
4.2. Experimental Section.....	58
4.2.1. Synthesis of ⁷⁷ Se enriched CdSe nanocrystals (CdSe-HDA).....	58
4.2.2. NMR.....	58
4.3. Results and Conclusions.....	59
4.3.1. ⁷⁷ Se Spin-Echo NMR: Surface and Core Components.....	59
4.3.2. ⁷⁷ Se CPMAS NMR: Surface and Near Surface Species.....	67
4.3.3. ⁷⁷ Se Nuclear Shielding and Band-gap.....	74

4.4. Conclusions.....	85
4.5. References.....	86
Chapter 5. Oxidation Depth Profiling in InGaP Nanocrystals.	
5.1. Introduction.....	89
5.2. Experimental Section.....	91
5.2.1. Synthesis of InGaP Nanocrystals (unetched).....	91
5.2.2. Etching of InGaP Nanocrystals.....	92
5.2.3. NMR.....	96
5.3. Results and Conclusions.....	98
5.3.1. Total Phosphorous Site Identification (^{31}P MAS NMR).....	98
5.3.2. Surface ^{31}P Oxidation Identification by 2D $^{31}\text{P}\{^1\text{H}\}$ HETCOR NMR.....	103
5.3.3. Oxidation Site Characterization using ^{31}P CPMAS.....	107
5.3.4. Spatial Proximities of PO_4 and PO_3 on the Surface.....	114
5.4. Conclusions.....	117
5.5. References.....	120
Chapter 6. HF etching and the Surface Structure of InGaP Nanocrystals.	
6.1. Introduction.....	128
6.2. Experimental Section.....	130
6.2.1. Synthesis of InGaP Nanocrystals.....	130

6.2.2. Etching of InGaP Nanocrystals.....	130
6.2.3. NMR.....	131
6.3. Results and Discussion.....	131
6.3.1. Gallium Occupation and Molecular Order.....	131
6.3.2. Indium Occupation.....	139
6.4. Conclusions.....	142
6.5. References.....	144

List of Figures.

Chapter 1.

1.1. Domains of Nanocrystals.....	2
1.2. Schematic representations of solid-state NMR pulse techniques.....	6

Chapter 2.

2.1. ^{13}C NMR spectra of the passivating layer in CdSe-HDA.....	19
2.2. 2D $^{13}\text{C}\{^1\text{H}\}$ HETCOR NMR of 2nm CdSe-HDA.....	23
2.3. ^{13}C MAS of 2 nm CdSe-HDA in which the thiophenol has been ligand exchanged with 2,4-difluorothiophenol.....	25
2.4. ^{13}C NMR of highly water soluble CdSe-AET.....	27

Chapter 3.

3.1. ^{113}Cd spin-echo and CPMAS NMR spectra of 2 nm CdSe-HDA.....	38
3.2. ^{113}Cd NMR spectrum of the precursor, $[\text{Li}]_4[\text{Cd}_{10}\text{Se}_4(\text{SC}_6\text{H}_5)_{16}]$, and bulk CdSe.....	39
3.3. ^{77}Se spin-echo and CPMAS NMR spectra of 2 nm CdSe-HDA.....	41
3.4. ^{77}Se NMR spectrum of the precursor, $[\text{Li}]_4[\text{Cd}_{10}\text{Se}_4(\text{SC}_6\text{H}_5)_{16}]$, and bulk CdSe.....	43
3.5. Integrated ^{77}Se peak intensities from ^1H - ^{77}Se CPMAS plotted as a function of contact time.....	45
3.6. 2D $^{113}\text{Cd}\{^1\text{H}\}$ HETCOR NMR of 2nm CdSe-HDA.....	50

3.7. 2D $^{77}\text{Se}\{^1\text{H}\}$ HETCOR NMR of 2nm CdSe-HDA.....	52
3.8. Structural Model of 2 nm CdSe-HDA.....	53

Chapter 4.

4.1. ^{77}Se spin-echo MAS NMR spectra of 2 nm, 2.5 nm, 2.9 nm, 3.7 nm, and 4 nm CdSe nanocrystals.....	60
4.2. ^{77}Se spin-echo MAS NMR spectra with fitted gaussian peaks separating the spectra into surface and core selenium components.....	62
4.3. ^{77}Se spin-echo MAS and CPMAS NMR spectra of 2nm, 2.5 nm, 2.9 nm, 3.7 nm, and 4 nm CdSe-HDA nanocrystals.....	68
4.4. Example of a 2.9 nm ^{77}Se CPMAS spectrum fit to 4 gaussians.....	70
4.5. Integrated ^{77}Se peak intensities from ^1H - ^{77}Se CPMAS for 2.9 nm CdSe-HDA plotted as a function of contact time.....	71
4.6. Plot of the ^{77}Se chemical shift from surface and core components (spin-echo) and Se near surface (CPMAS) for 2 nm, 2.5 nm, 2.9 nm, 3.7 nm, 4 nm and bulk CdSe versus the inverse band-gap energy.....	77
4.7. Plot of the number of Cd and Se in the material versus the ^{77}Se chemical shift values from the surface and core components and from Se near surface.....	80
4.8. Plot of the ^{77}Se center of gravity from the spin-echo spectra and CPMAS for 2 nm, 2.5 nm, 2.9 nm, 3.7 nm, 4 nm and bulk CdSe versus the inverse band-gap energy.....	82

4.9. Plot of the number of Cd and Se atoms in the material versus the ^{77}Se chemical shift values for the center of gravity from spin-echo and CPMAS.....	84
--	----

Chapter 5.

5.1. Absorbance spectra of unetched and HF etched 4.5 nm InGaP nanocrystals.....	93
5.2. TEM image of unetched 4.5 nm InGaP nanocrystals.....	94
5.3. TEM image of etched 4.5 nm InGaP nanocrystals.....	95
5.4. Solid-state ^{31}P single-pulse spectra of unetched and HF etched InGaP nanocrystals.....	99
5.5. $^{31}\text{P}\{^1\text{H}\}$ FSLG HETCOR spectrum of unetched InGaP nanocrystals.....	104
5.6. Solid-state ^{13}C single pulse spectra of HDA capped InGaP nanocrystals.....	106
5.7. ^{31}P CPMAS spectra of unetched InGaP nanocrystals.....	109
5.8. The InGaP nanocrystal integrated ^{31}P peak intensities from ^1H - ^{31}P CPMAS plotted as a function of contact time.....	111
5.9. 2D Double-Quantum $^{31}\text{P}\{^{31}\text{P}\}$ NMR spectrum of unetched InGaP nanocrystals.....	115
5.10. Solid-state ^{19}F single-pulse spectrum of etched InGaP nanocrystals.....	118

Chapter 6.

6.1. Solid-state ^{71}Ga spin-echo MAS NMR spectra of InGaP nanocrystals.....	133
6.2. ^{71}Ga MAS NMR spectra of bulk GaP.....	134
6.3. ^{115}In spin-echo MAS NMR spectra of InGaP nanocrystals.....	140

6.4. ^{115}In MAS NMR spectra of bulk InP.....	141
---	-----

List of Tables.

Chapter 3.

3.1. Analysis of the ^{77}Se sites frequency, line-width, and population.....	42
3.2. 2 nm CdSe-HDA ^{77}Se cross-relaxation time constants.....	47

Chapter 4.

4.1. Summary of ^{77}Se chemical shifts, linewidths, center of gravity, and calculated and measured surface to core ratios for spin-echo and CPMAS data for $\text{Li}_4[\text{Cd}_{10}\text{Se}_4(\text{SC}_6\text{H}_5)_{16}]$, 2 nm, 2.5 nm, 2.9 nm, 3.7 nm, 4 nm and bulk CdSe.....	65
4.2. 2.9 nm CdSe-HDA ^1H - ^{77}Se cross-relaxation time constants.....	72

Chapter 5.

5.1. InGaP nanocrystal ^1H - ^{31}P cross-relaxation time constants.....	112
5.2. Summary of ^{31}P site assignments, positions and corresponding methods of characterization for HF etched and unetched InGaP Nanocrystals.....	113

Chapter 1. Introduction.

1.1. Overview of Nanocrystal Regions and Reconstruction.

Nanotechnology is one of the most prominent disciplines in science and technology today, bridging the fields of biology, physics, chemistry, and engineering. Semiconductor nanocrystals have attracted considerable attention since they offer a unique opportunity to observe the evolution of their physical properties with size. This has led to applications in a wide range of areas, including solid-state lighting, light emitting diodes, and biological labeling.¹⁻¹⁰ For a successful development of nanotechnology, many key challenges in nanoscience must be tackled and a number of fundamental problems must be scientifically explored and solved. Understanding the correlation between the thermodynamic stability and fundamental structural properties of nanomaterials, which is influenced by the nanocrystal (NC) type, size, and passivating layer, is an important area. Of particular interest is the understanding of the surface chemistry, reconstruction and inorganic/organic interface associated with the electronic and optical properties in nanoscale materials.¹¹⁻¹⁷

The structure of a nanomaterial can be envisioned as consisting of a core inorganic structure reminiscent of a bulk structure, surrounded by a reconstructed inorganic surface shell, and capped by an organic passivating layer, reminiscent of a self-assembled monolayer.¹⁸⁻²² The impact on the structural attributes of nanocrystals

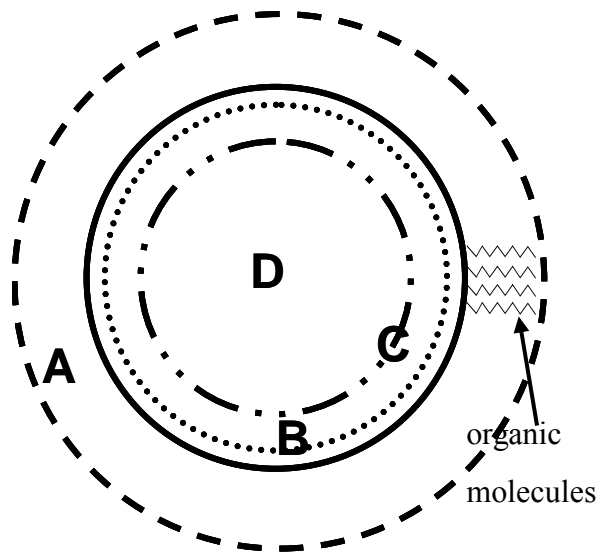


Figure 1.1. Domains of Nanocrystals
(A) Passivating layer, (B) Surface of particle, (C) Near-surface of particle, (D) Core of particle.

can be delineated into four distinct regions of the NC (Figure 1.1). The passivation layer, region A, can be envisioned as a three-dimensionally constrained monolayer of tightly packed organic amphiphiles that act to thermodynamically stabilize the surface through a headgroup-surface interaction,^{21,22} as well as provide solubility in various solvents. Region B consists of the molecular level interaction between the surface atoms and the headgroup of the passivant and the outermost surface sites, which is at the inorganic-organic interface.^{23,24} Region C encompasses the top layer of the nanomaterials and one crystallographic plane down that are prone to reconstruction,²⁵⁻²⁸ and region D consists of the NC core, which is predicted to be minimally affected by surface interactions. Although particle reconstruction may occur in the core, passivant-driven surface reconstruction has recently been suggested to be influential to the observed optical properties of CdSe and InP nanomaterials.²⁵⁻³³

Although the need for a thorough understanding of the surface interfacial region has been established, it nevertheless represents the most difficult to analyze experimentally, because of the low ratio of surface species relative to core species in nanoscale materials. This leaves the development of a deeper understanding of the correlation between optical response and surface reconstruction as a difficult but important task. Many standard spectroscopic techniques, such as photoluminescence, X-ray diffraction and transmission electron microscopy (TEM), have provided vital information about the optical nature, size, facets, and crystal structure of many types of nanomaterials. However, do to lack of long-range order and small size of the

particles, these studies do not reveal any clear surface structural features or detail. Nuclear magnetic resonance (NMR) spectroscopy, however, is highly sensitive to local chemical and electronic environment, element-specific, quantitative, and with utilization of special pulse techniques, can selectively probe distances and the various surfaces and interfaces of the nanocrystal (Figure 1.1). This gives rise to NMR as an invaluable analytical method for observation of reconstruction of nanomaterials.

1.2. NMR Pulse Techniques for Selective Analysis of Nanocrystal Regions.

Recent studies using ^{113}Cd have suggested the surface cadmium atoms can be clearly distinguished from the core cadmium atoms.^{34,35} These in depth studies in NMR on CdSe and other nanomaterials provide an ideal platform to test predictions of structural reconstruction of the different regions in a CdSe nanomaterial. By conducting ^{13}C , ^1H , ^{113}Cd , and ^{77}Se NMR (for example in CdSe), direct insight into regions A, B, and C can be gained, providing further correlating experimental data for the development of a model of the passivant layer interactions on the nanocrystal surface. Application of cross-polarization magic angle spinning (CPMAS) in the solid-state allows the surface to be selectively studied, while other techniques such as spin-echo sequences allow the entire nanomaterial to be addressed.³⁴⁻³⁸ As observed in previous studies on layered silicate surfactant mesophases, NMR can provide insight into the degree of crystallinity and reconstruction of the material, as well as

knowledge of the connectivities of surface atoms through two-dimensional techniques.³²

The principal solid-state NMR pulse sequences extremely useful in the study of nanomaterials and present in this dissertation are given below Figure 1.2 A-C. The spin-echo (Figure 2.1A) MAS NMR pulse sequence ($\pi/2$ - τ - π - τ -acquisition) measures all of the nuclei of interest (core and surface) in the isolated particle. It is beneficial for materials with broad NMR peaks and minimizes problems due to rf bleeding and receiver recovery. It can provide valuable information regarding the structural differences within the particles, as well as size-dependent shielding parameters with average bandgap energy and ionicity changes of the core lattice. The spin-echo experiment is very important for such nuclei as ^{113}Cd , ^{77}Se , ^{71}Ga , and ^{115}In which possess short T_2 relaxations and broad NMR peaks..

The CPMAS NMR pulse sequence is shown in Figure 1.2 B. It involves a proton $\pi/2$ pulse, spin-locking of the protons, followed by a polarization transfer to the nuclei of choice, and detection in this dimension. In this dissertation, the polarization transfer is from the abundant ^1H spins on the passivating ligands to the spins of the inorganic particle via through space nuclear dipole-dipole interactions.³⁴⁻³⁶ These interactions follow a $1/R^3$ distance dependence allowing only spacially nearby species to be measured. Therefore only atoms at or near the surface of the particle are measured, establishing a surface selective analysis. Also extremely significant with the CPMAS pulse technique is the ability to vary the contact time of cross-polarization which can allow for a depth profile of the material to be established.

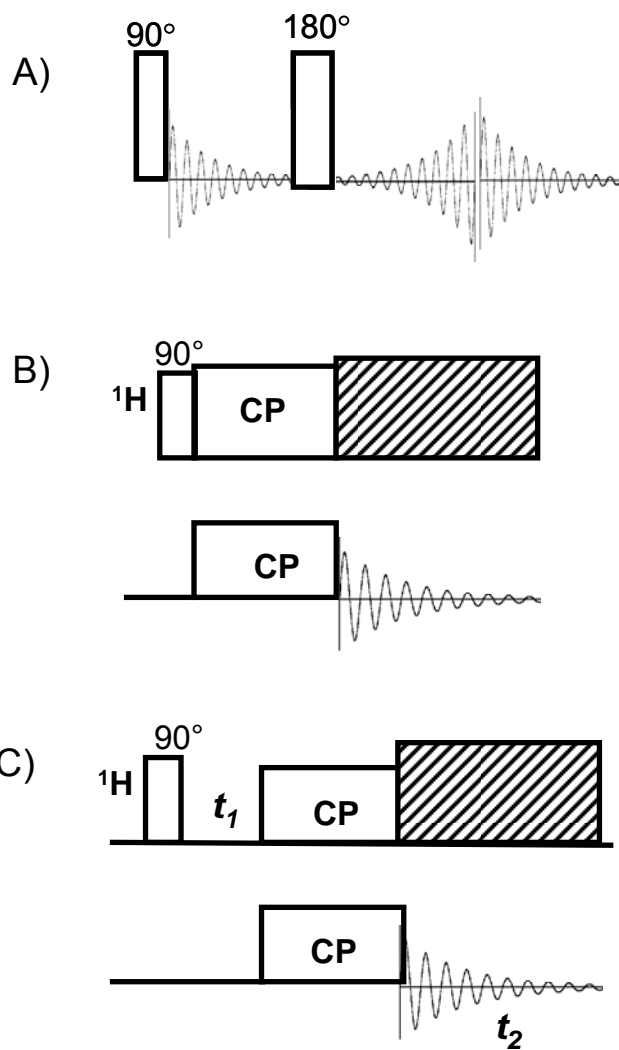


Figure 1.2. Schematic representations of solid-state NMR pulse techniques. (A) Spin-echo. (B) CPMAS. (C) HETCOR.

The 2-dimensional (2D) heteronuclear chemical shift correlation^{38,39} (HETCOR) NMR sequence is depicted in Figure 1.2C. For this technique the sequence involves a proton $\pi/2$ pulse, an evolution period, t_1 , where all the forces acting upon the nuclei are allowed to evolve, cross-polarization to the nuclei of choice and detection in this dimension. By expansion of the spectrum in two dimensions, and utilization of the through space distance dependent dipole-dipole interactions, an extremely powerful tool for structural elucidation is developed which provides a detailed distinction of passivating ligands in close proximity to surface and near surface sites as well as spatial determination of interacting surface ligands.

In this dissertation, solid-state NMR is used to analyze crucial structural information regarding the surfaces and interfaces in nanoscale materials. Through specific pulse techniques including spin-echo, CPMAS, and HETCOR, species determination, molecular order, surface vacancies, spatial proximities, ionicity changes, and structure-function correlations are revealed. Chapters 2, 3 and 4 investigate the fundamental structure and nature of the organic surface passivating layer, surface and core species, as well as the evolution of these sites with size in CdSe nanocrystals. Chapters 5 and 6 provide detailed studies of the oxidation layer and molecular transformation with hydrogen fluoride treatment of InGaP nanocrystals. In both materials, structural models of the various regions of the nanocrystal (Figure 1.1), essential to the advancement of nanotechnology, are developed.

References

1. Bhargava, R. N.; Chhabra, V.; Som, T.; Ekimov, A.; Taskar, N. *Phys. Status Solidi B* **2002**, *229*, 897-901.
2. De la Torre, J.; Souifi, A.; Lemiti, M.; Poncet, A.; Busseret, C.; Guillot, G.; Bremond, G.; Gonzalez, O.; Garrido, B.; Morante, J. R. *Physica E* **2003**, *17*, 604-606.
3. Modreanu, M.; Gartner, M.; Aperathitis, E.; Tomozeiu, N.; Androulidaki, M.; Cristea, D.; Hurley, P.; Maltins, L. *Physica E* **2003**, *16*, 461-466.
4. Irrera, A.; Pacifici, D.; Miritello, M.; Franzo, G.; Priolo, F.; Iacona, F.; Sanfilippo, D.; Di Stefano, G.; Fallica, P. G. *Physica E* **2003**, *16*, 395-399.
5. Pacifici, D.; Irrera, A.; Franzo, G.; Miritello, M.; Iacona, F.; Priolo, F. *Physica E* **2003**, *16*, 331-340.
6. Milliron, D. J.; Alivisatos, A. P.; Pitois, C.; Edder, C.; Frechet, Jean, M. J. *Adv. Mater.* **2003**, *15*, 58-61.
7. Yang, H.; Holloway, P. H.; Ratna, B. B. *J. Appl. Phys.* **2003**, *93*, 586-592.
8. Wang, D.; Rogach, A. L.; Caruso, F. *Nano Lett.* **2002**, *2*, 857-861.

9. Michalet, X.; Pinaud, F.; Lacoste, T. D.; Dahan, M.; Bruchez, M. P.; Alivisatos, A. P.; Weiss, S. *Single Mol.* **2001**, *2*, 261-276.
10. Tran, P. T.; Goldman, E. R.; Anderson, G. P.; Mauro, J. M.; Mattoussi, H. *Phys. Status Solidi B* **2002**, *229*, 427-432.
11. Tolbert, S. H.; Alivisatos, A. P. *Science* **1994**, *265*, 373.
12. Bowen Katari, J. E.; Colvin, V. L.; Alivisatos, A. P. *J. Phys. Chem.* **1994**, *98*, 4109-4117.
13. Dai, Y.; Han, S.; Dadi D.; Zhang, Y.; Qi, Y. *Solid State Commun.* **2003**, *126*, 103-106.
14. Pellegrino, P.; Garrido, B.; Garcia, C.; Ferre, R.; Moreno, J. A.; Morante, J. R. *Physica E* **2003**, *16*, 424-428.
15. Ispasoiu, R. G.; Lee, J.; Papadimitrakopoulos, F.; Goodson, T. *Chem. Phys. Lett.*
16. Koberling, F.; Mews, A.; Basche, T. *Adv. Mater.* **2001**, *13*, 672-676.
17. Cordero, S. R.; Carson, P. J.; Estabrook, R. A.; Strouse, G. F.; Buratto, S. K. *J. Phys. Chem. B* **2000**, *104*, 12137-12142.
18. Becerra, L. R.; Murray, C. B.; Griffin, R. G.; Bawendi, M. G. *J. Chem. Phys.* **1994**, *100*, 3297-3300.

19. Luedtke, W. D.; Landman, U. *J. Phys Chem.* **1996**, *100*, 13323-13329.
20. Hostetler, M. J.; Wingate, J. E.; Zhong, C.-J.; Harris, J. E.; Vachet, R. W.; Clark, M. R.; Londono, J. D.; Green, S. J.; Stokes, J. J.; Wignall, G. D.; Glish, G. L.; Porter, M. D.; Evans, N. D.; Murray, R. W. *Langmuir* **1998**, *14*, 17-30.
21. Meulenber, R. W.; Bryan, S.; Yun, C. S.; Strouse, G. F. *J. Phys. Chem B* **2002**, *106*, 7774-7780.
22. Meulenber, R. W.; Strouse, G. F. *J. Phys. Chem. B* **2001**, *105*, 7438-7445.
23. Sachleben, J. R.; Colvin, V.; Emsley, L.; Wooten, E. W.; Alivisatos, A. P. *J. Phys. Chem. B* **1998**, *102*, 10117-10128.
24. Sachleben, J. R.; Wooten, E. W.; Emsley, L.; Pines, A.; Colvin, V.; Alivisatos, A. P. *Chem. Phys. Lett.* **1992**, *198*, 431-436.
25. Aldana, J.; Wang Y. A.; Peng, X. *J. Am. Chem. Soc.* **2001**, *123*, 8844-8850.
26. Meulenber, R. W.; Strouse, G. F. *Phys. Rev. B* **2002**, *66*, 035317.
27. Carter, A. C.; Bouldin, C. E.; Kenner, K. M.; Bell, M. I.; Woicik, J. C.; Majetich, S. A. *Phys. Rev. B.* **1997**, *55*, 13822-13828.
28. Micic, O.I.; Sprague, J.; Lu, Z.; Nozik, A.J. *Appl. Phys. Lett.* **1996**, *68*, 3150-3152.

29. Adam, S.; Weller, H. et al. *Eur. Phys. J. D.* **2003**, *24*, 373-376.
30. Fu, H.; Zunger, A. *Phys. Rev. B.* **1997**, *56*, 1496-1508.
31. Langof. L.; Ehrenfreund, E.; Lifshitz, E.; Micic, O.I.; Nozik, A.J. *J. Phys. Chem. B.* **2002**, *106*, 1606-1612.
32. Micic, O.I.; Nozik, A.J.; Lifshitz, E.; Rajh. T.; Poluektov, O.G.; Thurnauer, M.C. *J. Phys. Chem. B.* **2002**, *106*, 4390-4395.
33. Talapin, D.; Gaponik. N.; Borchert, H.; Rogach. A. L.; Haase, M. ; Weller, H. *J. Phys. Chem. B.* **2002**, *106*, 12659-12663.
34. Ladizhansky, V.; Hodes, G.; Vega, S. *J. Phys. Chem. B* **1998**, *102*, 8505-8509.
35. Elbaum, R.; Vega, S.; Hodes, G. *Chem. Mater.* **2001**, *13*, 2272-2280.
36. Berrettini, M.G.; Braun, G.; Hu, J.G.; Strouse, G.F. *J. Am. Chem. Soc.*, **2004**, *22*, 7063 -7070.
37. Tomaselli, M; Yarger, J.L.; Bruchez, M.; Havlin, R.H.; deGraw D.; Pines, A.; Alivisatos, A.P. *J. Chem. Phys.* **1999**, *110*, 8861-8864.

38. Vega, A.J. *J. Am. Chem. Soc.*, **1988**, *110*, 1049-1054.

39. Janicke, M. T.; Landry, C.C.; Christiansen, S.C.; Kumar, D.; Stucky, G.D.;
Chmelka, B.F.; *J. Am. Chem. Soc.*, **1998**, *120*, 6940-6951.

Chapter 2. NMR Characterization of the Surface Passivation in CdSe

Nanocrystals

2.1 Introduction.

Nanocrystals, which are often modeled using a "spherical" approximation, are crystalline and faceted. The exposed atoms on the facets dictate the nature of the organic passivant interaction and can lead to surface reconstruction following passivant binding. This interaction has been shown to effect important aspects of the materials including size, shape, stability, photoluminescence and oxidation.¹⁻⁸ Also important for technological applications, is the ability of the passivant layer to provide stability in appropriate solvents as well as possess terminal functionalities that allow for selective interactions for fabrication of nanoscale 2- and 3-dimensional architectures.⁸⁻¹²

Due to the significance of the passivation layer and the corresponding inorganic/organic interface, investigation into of the nature of the organic ligands on the surface of the particles is necessary. Solution and solid-state ¹³C and ¹H NMR has proven an excellent characterization probe for the binding site (chemical shift) and freedom of rotation (line width) of the passivant layer in nanocrystals because of the sensitivity of the technique to electronic local environment and mobility^{7,8,13-19}.

Notably, Sachleben *et al.* have shown that the T_2 in thiols appended to CdS is sensitive to the chemical environment of binding¹³⁻¹⁴ and Pan *et al.* has indicated rapid amine exchange as well as a suggested structural binding motif on the surface of Ru particles observable by solution ^{13}C solution NMR⁷; also, interestingly, Elbaum *et al.* has utilized solid-state ^{13}C NMR to identify a bridging carboxylate passivant on the surface of CdS¹⁸.

In this chapter, the passivating layer of single source precursor prepared CdSe nanocrystals (CdSe-HDA) is investigated by solution and solid-state ^1H and ^{13}C NMR experiments to obtain vital information about the nature, binding motif, ligand exchange, solubility, and spatial proximities of the corresponding organic ligands. Intriguingly, in this material, hexadecylamine (HDA) and thiophenol are found to selectively bind on the isolated nanocrystal. Powerful 2D $^{13}\text{C}\{^1\text{H}\}$ heteronuclear chemical shift correlation (HETCOR) NMR was utilized to probe the spatial proximities of the two passivants on the surface of CdSe-HDA; in conjunction with ligand exchange experiments this study provides direct knowledge of a special binding site for thiophenol.

2.2 Experimental Section.

2.2.1 Synthesis of CdSe Nanocrystals (CdSe-HDA).

CdSe nanocrystals were prepared by a previously published single source precursor method.²⁰ Approximately 2.1 g of $\text{Li}_4[\text{Cd}_{10}\text{Se}_4(\text{SC}_6\text{H}_5)_{16}]$ (0.653 mmol) was heated in 75 g of n-hexadecylamine (HDA) to 120 °C under argon. The reaction progress was followed by UV-vis absorbance spectroscopy and removal from heat when the desired nanocrystal size was reached. UV-vis experiments were carried out on the hot reaction mixture by direct sampling of the reaction mixture (1-5 μL) and dilution of the aliquot into 3 mL of chloroform. The onset of the absorption profile was characteristic of the size of the nanocrystals. After cooling to 50 °C when the appropriate size nanocrystal was reached, the CdSe sample was precipitated by the addition of approximately 200 mL of methanol and was collected by centrifugation. Purification and size selection was accomplished by dissolution in a minimum amount of chloroform, re-precipitation by addition of methanol, and centrifugation (3 \times).

2.2.2 Ligand Exchange with 2,4-Difluorothiophenol.

Surface ligand exchange of thiophenol on CdSe-HDA was accomplished by the addition of approximately 2 mL of 2,4-difluorothiophenol to 100 mg of CdSe-HDA. The mixture was stirred for 5-10 min at 60 °C under argon. After being

cooled to room temperature, approximately 5 mL of methanol was added, and the material was collected by centrifugation. The sample was then dissolved in a minimum amount of chloroform and precipitated via the addition of methanol. This washing sequence was repeated three times, followed by a final rinse with methanol and being dried overnight under vacuum.

2.2.3 Preparation of Water Soluble CdSe (CdSe-AET).

Surface ligand exchange of the hexadecylamine (HDA) passivant layer on CdSe (CdSe-HDA) by 2-aminoethanethiol (AET) was accomplished by dispersing 20 mg of CdSe-HDA in 0.5 mL of N,N-dimethylformamide (DMF) with light sonication. The hydrochloride salt of AET was added (approximately 200 mg) and the suspension was heated in an oil bath at 70 °C for 5 min under N₂ with stirring. Complete dissolution of the CdSe into the DMF occurs during the ligand exchange process. The product was isolated by precipitation via the addition of methanol and the procedure was repeated in order to accomplish complete ligand exchange. After the final precipitation with methanol, the product was washed with methanol (3×), and dissolved in D₂O. Minimal insoluble products (<5%), if any, were removed by centrifugation. The ligand exchange yields a water-soluble CdSe-AET material with a pH of ~5.5 when dissolved in Nanopure water.

2.2.4 NMR.

Solution NMR experiments were performed at room temperature on a Bruker 500 MHz Avance spectrometer with a HX double resonance broadband probe operating at 125.8 and 500.1 MHz for ^{13}C and ^1H , respectively. The ^{13}C experiments were performed with a single pulse on ^{13}C while decoupling ^1H during acquisition. Typical parameters were: acquisition time 0.33 s, recycling delay 10 s, and a 90° pulse length of 15.3 s.

Solid-state magic angle spinning (MAS) NMR experiments were performed at room temperature on a Bruker 300 MHz Avance spectrometer with a 4-mm broadband MAS probe double tuned to ^1H (300.1 MHz) and the X channel to ^{13}C (75.5 MHz). A spinning speed of 12 kHz was used in all experiments. The MAS ^{13}C NMR experiments on CdSe-HDA and ligand-exchanged CdSe-HDA were performed under the conditions of two pulse phase modulated (TPPM) ^1H decoupling, an acquisition time of 24 ms, and a recycling delay of 20 s.

The 2D $^{13}\text{C}\{^1\text{H}\}$ HETCOR experiment was performed with a frequency-switched Lee-Goldberg (FSLG) irradiation of 85 kHz applied to the ^1H spins during the t_1 evolution period, ramp CP during mixing with a contact time of 6 ms, a TPPM ^1H decoupling during the data acquisition of 20.6 ms, 1280 scans for each t_1 point for a total of 256 t_1 points, a dwell time of 20 s, a recycling delay of 1 s, and a ^1H 90° pulse length of $3\mu\text{s}$.

The chemical shifts of ^1H and ^{13}C were referenced to TMS in all solution and solid-state NMR experiments.

2.3 Results and Discussion.

2.3.1 Surface Passivation of CdSe-HDA.

^{13}C NMR measurements on HDA-passivated 2-nm CdSe in solution and the solid state are shown in Figure 2.1. The α -, β -, and γ -carbons in free HDA appear at chemical shifts of 42.5, 34.3, and 27.0 ppm, respectively (Figure 2.1A). The solution ^{13}C NMR of CdSe-HDA (Figure 2.1B), shows a broadened α -carbon at the identical chemical shift position as free HDA. The β - and γ -carbons are broadened and poorly resolved because of overlapping peaks with the methylene carbons between 29 and 32 ppm. The observation of an unshifted α -carbon is in contrast to previously published work on alkanethiols⁸ on the surface of CdSe nanocrystals, (discussed in 2.3.4), where the chemical shift of the α -carbon is shifted downfield by approximately 5 ppm from that of free ligand. This is not surprising because of the differences in π -back-bonding for a thiol versus an amine ligand and the expected weaker interaction with the surface for

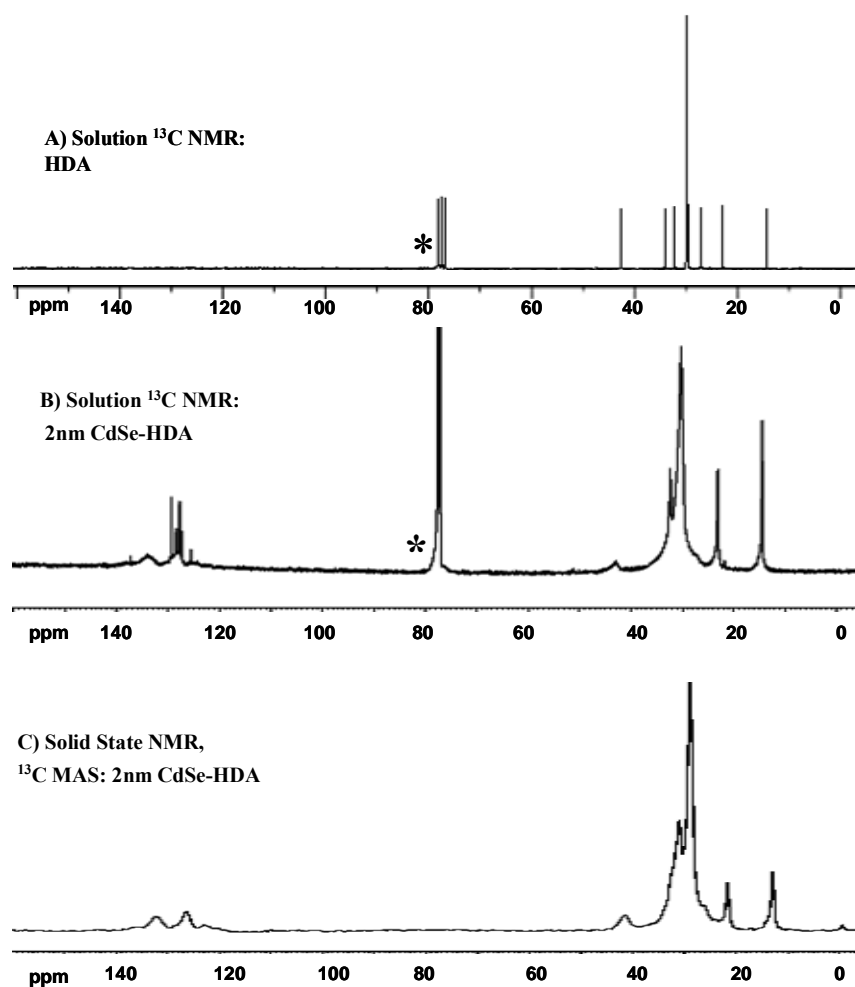


Figure 2.1. ^{13}C NMR spectra of the passivating layer on CdSe-HDA. (A) ^{13}C spectrum of HDA ($^*\text{CDCl}_3$) (B) ^{13}C spectrum of 2 nm CdSe-HDA ($^*\text{CDCl}_3$). This spectra shows HDA on the surface of the particle as well as bound and unbound thiophenol. (C) ^{13}C MAS spectrum of 2 nm CdSe-HDA. The alpha carbon of HDA is more pronounced than in solution and is at the same chemical shift as free HDA.

alkylamines relative to the thiol passivant. In addition to the HDA resonances, two broad peaks at 127.2 and 132.9 ppm (Figure 2B) are observed, which can be assigned to carbons of thiophenol bound to the surface of the particle. The narrow peaks between 127 and 129 ppm represent a small amount of free thiophenol in solution and are indicative of thiophenol being in slow exchange on the NMR time scale.

In the solid-state, the α -carbon of bound thiophenol (Figure 2.1C) can be more clearly distinguished than in solution NMR and appears at \sim 135 ppm, while the α -carbon of free thiophenol appears at 130.7 ppm, consistent with the expected shift for an α -carbon on a thiol binding to a CdSe surface. The presence of thiophenol on the surface was surprising because of the molar ratio of \sim 30:1 HDA/thiophenol for a typical reaction. However, it is known that thiols are better back-bonding ligands than amines, which suggests that either the thiophenol is a better ligator for CdSe or that thiophenol occupies a unique site stabilized under the reaction conditions. The possibility of a unique site for thiophenol is explored by correlation methods in the following section, and in more depth in Chapter 2. Although this data is resulting from 2 nm CdSe-HDA, thiophenol and HDA passivation on the isolated nanocrystal, as well as the corresponding broadening and shifts of particular carbon peaks is evident regardless of the size of the nanocrystal. These studies included CdSe-HDA nanocrystals with diameters ranging from 2-6 nm.

The broadening of the carbon peaks for thiophenol, as well as α -, β -, and γ -carbons on HDA in solution NMR (Figure 2.1B), can be attributed to chemical shift

distribution and a decreased T_2 relaxation time due to a lack of rotation upon binding to the CdSe surface.^{7,8,21} Chemical shift distribution was concluded as a likely factor in the broadening of the peaks due to the asymmetry of the line shape of the broadened peaks, although chemical shift anisotropy was concluded to be improbable because of identical line shapes of the broadened peaks in the solution and solid-state NMR spectra. As seen in Figure 2.1C, the carbons of thiophenol and the α -carbon of HDA become more pronounced in the solid-state than in solution NMR because of external averaging by MAS the dipolar interactions from the decreased rotation. In the MAS spectra, the β -, and γ -carbons of HDA are unresolved because of instrumental resolution limits giving rise to an overlap with the methylene chain carbons. As can be seen by comparison of the line widths for the carbon atoms in solution and solid-state NMR of CdSe-HDA, the rotation in the chain increases as you move down the chain toward the methyl group, as evidenced by the observation of narrowing lines. Carbon 15 and the methyl carbon at 22.9 and 14.2 ppm, respectively, are similar to the line width of free HDA, indicating that the terminal carbons do not experience hindered rotation and therefore are likely rotationally disordered with respect to the surface of the nanomaterial. A loss of signal intensity and a broadening for the α -, β -, and γ - ^{13}C peaks, which are closest to the NC surface, when compared to C_{15} is predicted for these materials because of rotational constraints for the passivants on the nanomaterial surface, as previously observed by FT-IR measurements of packing motifs on CdSe surfaces.^{2,23} Amorphous packing could lead to shifts in the NMR position also, but only a small change in the line

widths for the α -, β -, and γ -carbons because of the increased rotational freedom of amorphously structured surfaces.

2.3.2 Thiophenol and HDA Proximities.

The occurrence of both thiophenol and HDA binding in 2-nm CdSe-HDA raises the possibility of site or face selective binding on the CdSe surface. Using correlated NMR methods, the passivant site proximities were obtained through the use of 2D $^{13}\text{C}\{^1\text{H}\}$ HETCOR NMR experiments which provides direct insight into the possibilities of these binding motifs. The $^{13}\text{C}\{^1\text{H}\}$ frequency-switched Lee-Goldberg (FSLG) HETCOR experiment is shown in Figure 2.2, with separately measured single pulse ^1H MAS on the vertical axis in a traditional and magnified view and ^{13}C MAS spectra on the horizontal axis. The protons on the HDA chain appear between -0.8 and 1.8 ppm, and the protons on thiophenol appear between \sim 5.8 and 7.4 ppm, as seen from the correlations with their respective carbons in Figure 2.2. The amine protons are not seen because of broadening to the baseline from lack of rotation. FSLG HETCOR, which significantly increases homonuclear decoupling in the ^1H dimension, was chosen for this experiment to increase resolution to clearly distinguish the region of the HDA chain that is interacting with thiophenol by the correlations of thiophenol to HDA and to eliminate the ^1H spin diffusion mechanism.

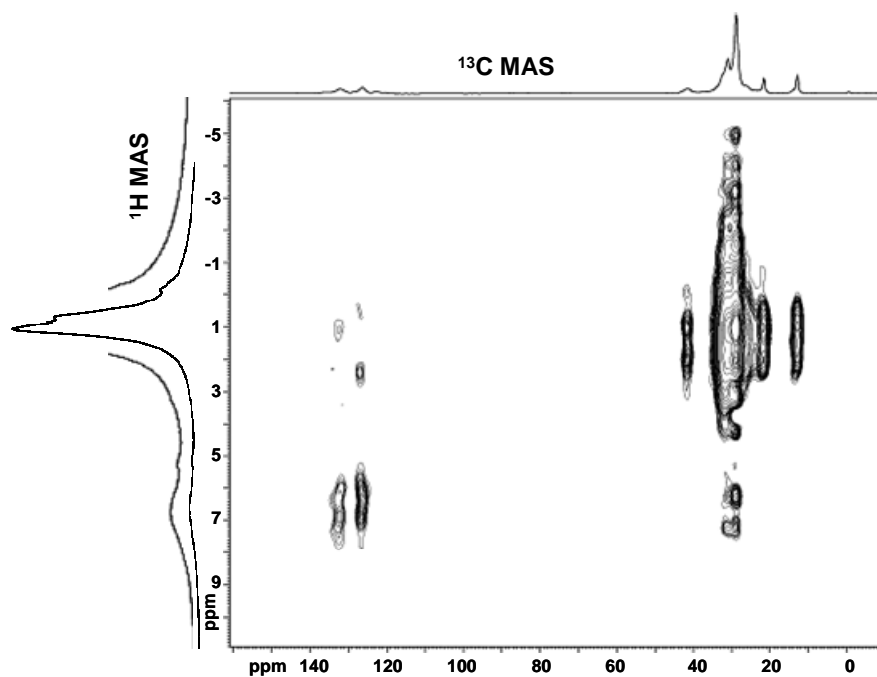


Figure 2.2. 2D $^{13}\text{C}\{^1\text{H}\}$ HETCOR NMR of 2nm CdSe-HDA. Separate single pulse ^1H MAS (traditional and magnified view), and ^{13}C MAS spectra reside along the vertical and horizontal axes of the contour plot, respectively. The correlation between thiophenol and HDA indicates that thiophenol is interacting with the middle of the HDA chain. (Spinning speed, 12 kHz; contact time, 6 ms)

As seen in Figure 2.2, the correlation from thiophenol protons at 6.8 ppm in the ^1H dimension to the carbons of HDA at approximately 30 ppm in the ^{13}C dimension indicates that thiophenol is strongly interacting with the middle of the HDA chain. This information establishes that thiophenol is in close proximity to the middle of the HDA chain. On the basis of this observation, it appears the ligands are residing on the same face rather than face selective capping of the two species, which would presumably give no correlation. There is the possibility if the ligands were on neighboring faces and with the proper tilt angles that there could be an interaction with the middle of the chain, but this would only be at the intersections leading to the observation of a weak correlation.

2.3.3 Ligand Exchange with 2,4-difluorothiophenol.

Face-selective capping of thiophenol in the isolated crystal can be disregarded from the results of the 2D correlation spectra in Figure 2.2 but the exact nature of the site is still not known from these results directly. More evidence for this positional assignment arises from data obtained by ^{13}C MAS of 2-nm CdSe-HDA that has been ligand-exchanged with 2,4-difluorothiophenol (Figure 3). Ligand exchange with thiophenol was first attempted and no change in the ^{13}C MAS spectra was noticed; therefore, a similar ligand, 2,4-difluorothiophenol, was used for its differing ^{13}C peaks in the MAS spectra. Following ligand exchange with 2,4-difluorothiophenol, HDA is still present but thiophenol has been completely replaced. The peaks at 159 and 162 ppm represent the 2 and 4 carbons with attached fluorines, respectively.

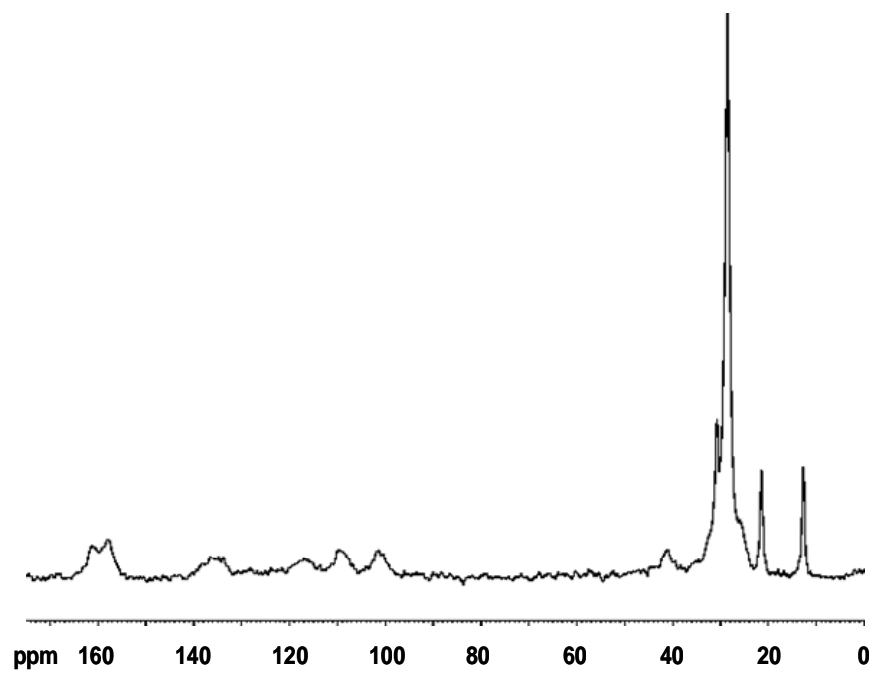


Figure 2.3. ^{13}C MAS of 2 nm CdSe-HDA in which the thiophenol has been ligand exchanged with 2,4- difluorothiophenol. (Spinning speed, 12 kHz)

Carbons 1, 3, 5, and 6 appear at 138, 102, 110, and 118 ppm, respectively. To our surprise, adding a fluorinated-thiophenol derivative to the material, followed by the usual ligand exchange protocol, does not displace the HDA as a strong binding ligand would be expected to do; instead, the fluorinated thiophenol only displaces bound thiophenol as evidenced by recapping with 2,4-difluorothiophenol (Figure 2.3). Therefore, it can be concluded that the presence of thiophenol on the nanocrystal does not come from a higher affinity for ligation on CdSe than HDA, most likely due to the electron withdrawing properties of the benzene ring diminishing the strong Lewis base and back-bonding characteristics of simple alkane thiols. Ligand exchange to replace the thiophenol on the surface of CdSe-HDA by HDA and pyridine utilizing usual protocols was also attempted. Interestingly, neither ligand was successful with the replacement and led to a conclusion of a special site for thiophenol on the surface of the material.

2.3.4. Ligand Exchange to produce Water Soluble CdSe (CdSe-AET).

More insight into the nature of the surface sites on CdSe, as well as the strength of bonding of ligands can come from recapping with an alkane thiol. It is well known that alkane thiols are better back-bonding ligands than amines, which suggests that these ligands will have a higher affinity for the surface of CdSe. Therefore, through standard recapping protocols we expect an alkane thiol to completely recap the surface of the particle; and with this knowledge, the use of a

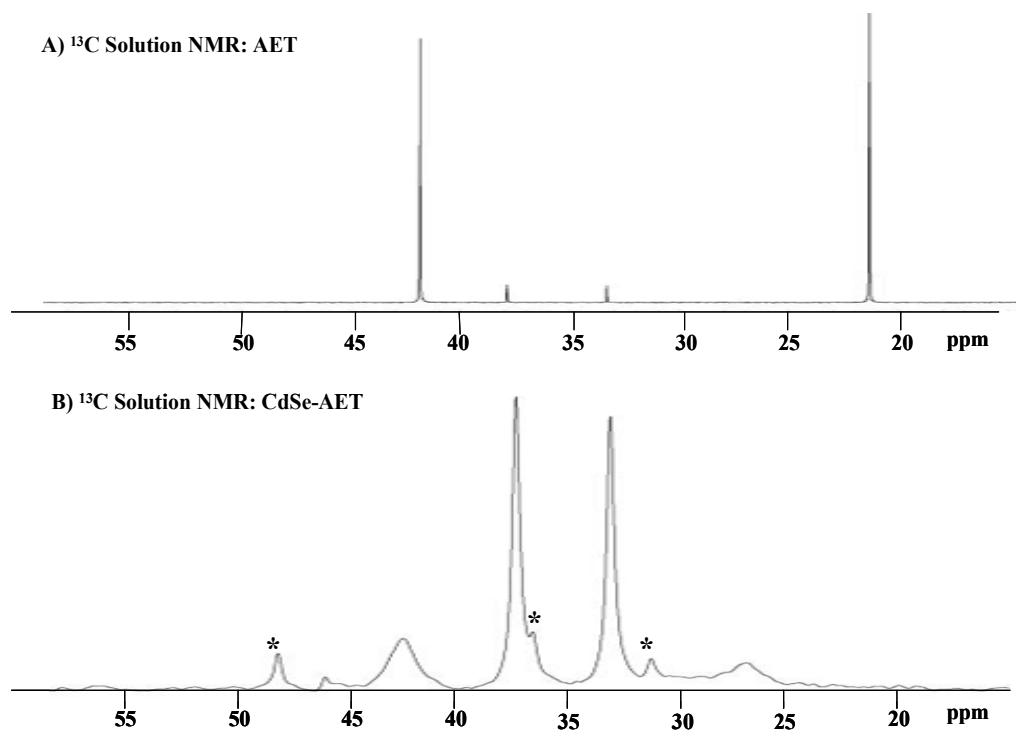


Figure 2.4. ^{13}C NMR of highly water soluble CdSe-AET.
(A) ^{13}C NMR spectrum in D_2O of aminoethanethiol (AET).
(B) ^{13}C NMR spectrum in D_2O of CdSe-AET. The peaks observed at 34.3 and 38.9 ppm in both spectra correspond to the disulfide of AET. Solvent impurities are labeled by and asterisk (*).

amine-functionalized alkane thiol on CdSe-HDA can be utilized to make highly water soluble CdSe.

The hydrochloride salt of 2-aminoethanethiol (AET) is water soluble and was therefore chosen as a good model ligand to demonstrate the complete recapping, preferential binding moieties, and change in solubility of the nanocrystals from the original organic soluble ligands on CdSe-HDA. Evidence for the complete exchange of HDA and thiophenol for AET and the nature of the binding of terminal AET moieties to the CdSe surface in AET was analyzed by solution ^{13}C NMR spectroscopy (Figure 2.4). Consistent with a high percentage of ligand exchange of HDA by AET on CdSe, no evidence for the ^{13}C peaks corresponding to HDA at 29-32, 22.9, and 14.2 ppm or between 127-133 ppm for thiophenol, are present in the spectrum. ^{13}C NMR analysis of the hydrochloride salt of AET dissolved in D_2O yields a peak at 42.8 ppm corresponding to the carbon alpha to the nitrogen and a peak at 22.3 ppm corresponding to the carbon alpha to the sulfur (Figure 2.4A).²⁴ The peaks at 34.3 and 38.9 ppm correspond to small amounts of the disulfide of AET present in the sample.

Upon binding to the CdSe surface, the chemical shift of the carbon alpha to the nitrogen remains at 42.8 ppm but is broadened from that of free AET. The carbon alpha to the sulfur shifts downfield to 27.3 ppm and displays a broadening greater than that of the carbon alpha to the nitrogen (Figure 2.4B). Preferential binding of the thiolate moiety to the CdSe surface without scrambling is supported by the

observation of a lack of 4 peaks or sets of carbon peaks in the NMR, expected for a system exhibiting both -S and -NH₂ binding of the AET at the CdSe surface. The broadening of the peaks can be attributed to a decreased T_2 relaxation time attributed to a lack of rotation upon binding to the CdSe surface. Broadening of the NMR signals for organic amphiphiles bound to surfaces has previously been observed for both CdSe and Au nanomaterials in earlier studies.^{7,21,25} The greater broadening and the large shift of the carbon alpha to the sulfur suggest preferential R-S binding to the CdSe surface. Binding of the sulfur to the CdSe instead of the ammonium functionality is further supported by the observation of the water solubility, which is predicted for a terminal ammonium group interacting with water.

Solution NMR was chosen for analysis of the organic surface ligands for CdSe-AET because it provided direct evidence of disulfide formation of the AET ligands from the surface of the particle. In the ¹³C spectra of CdSe-AET (Figure 4B), a significant amount of the disulfide of AET is present as evidenced by the peaks 34.3 and 38.9 ppm; this is likely due to instability of the short chain ligand on the surface of the particle or photo-oxidation of AET as has been reported for thiols on CdSe surfaces.³ Impurities due to DMF at 31.8 and 38.1 ppm and methanol at 49.3 ppm are also identified in the spectra arising from the recapping protocol. The peaks corresponding to the disulfide, DMF, and methanol are artificially broadened due to data processing from the line-broadening of 50 Hz in order to enhance the broadened signals of the bound AET.

2.4 Conclusions.

Solution and solid-state ^{13}C NMR indicates the interesting presence of thiophenol and HDA ligands binding selectively on the surface of lyothermally prepared CdSe-HDA. The freedom of rotation decreases as chemical shift distribution of the corresponding carbon increases from movement from the methyl carbon to the α -carbon of the HDA chain. In contrast to thiol ligands, the α -carbon of HDA remains at the same position as free ligand. Exploration into the presence of thiophenol on the particle post synthesis was accomplished by recapping with a 2,4-difluorothiophenol which, interestingly, only replaces thiophenol indicating a special site for thiophenol binding. 2D $^{13}\text{C}\{^1\text{H}\}$ HETCOR NMR experiments supported this hypothesis with direct evidence of close proximities of thiophenol and HDA on the surface of the particles ruling out face-selective binding. This chapter also demonstrated utilizing the preferential binding of an alkane thiol over an amine to produce highly water soluble particles capped with AET. This passivating layer study indicates the need for exploration into the selenium and cadmium sites in the material (Chapter 3) to fully explore the nature of the site of binding of thiophenol on the isolated particle.

2.5 References.

1. Cheon, J.; Kang, N.; Lee, S.; Lee, J.; Yoon, J. Oh, S. *J. Am. Chem. Soc.* **2004**, *126*, 1950-1951.
2. Pokrant, S.; Whaley, K. B. *Eur. Phys. J. D* **1999**, *6*, 255-267.
3. Aldana, J.; Wang Y. A.; Peng, X. *J. Am. Chem. Soc.* **2001**, *123*, 8844-8850.
4. Kubo, T.; Isobe, T. Senna, M. *J. Lumin.* **2002**, *99*, 39-45.
5. Talabin, D.V.; Rogach, A.L.; Mekis, I.; Haubold, S.; Kornowski, A.; Haase, M. Weller, H. *Colloids Surf.*, **2002**, *202*, 145-154.
6. Adam, S.; Weller, H. et al. *Eur. Phys. J. D.* **2003**, *24*, 373-376.
7. Pan, C.; Pelzer, K.; Philippot, K.; Chaudret, B.; Dassenoy, F.; Lecante, P.; Casanove, M. *J. Am. Chem. Soc.* **2001**, *123*, 7584-7593.
8. Cumberland, S. L.; Berrettini, M. G.; Javier, A.; Strouse, G. F. *Chem. Mater.* **2003**, *15*, 1047-1056.

9. Chen, S. W.; Murray, R. W. *J. Phys. Chem. B* **1999**, *103*, 9996.
10. Warner, M. G.; Reed, S. M.; Hutchison, J. E. *Chem. Mater.* **2000**, *12*, 3316.
11. Polleux, J.; Pinna, N.; Antonietti, M.; Niederberger, M. *Adv. Mater.* **2004**, *16*, 436-439.
12. Harfenist, S.; Wang, Z. L.; Alvarez, M.; Vezmar, I.; Whetten, R. *J. Phys. Chem.* **1996**, *100*, 13904-13910.
13. Sachleben, J. R.; Colvin, V.; Emsley, L.; Wooten, E. W.; Alivisatos, A. P. *J. Phys. Chem. B* **1998**, *102*, 10117-10128.
14. Sachleben, J. R.; Wooten, E. W., et al. *Chem. Phys. Lett.* **1992**, *198* (5), 431.
15. Mayeri, D.; Phillips, B.L.; Augustine, M.P.; Kauzlarich, S.M. *Chem. Mater.* **2001**, *13*, 765-770.
16. Ladizhansky, V.; Hodes, G.; Vega, S. *J. Phys. Chem. B* **1998**, *102*, 8505-8509.
17. Ladizhansky, V.; Hodes, G.; Vega, S. *J. Phys. Chem. B* **2000**, *104*, 5237-5241
18. Elbaum, R.; Vega, S.; Hodes, G. *Chem. Mater.* **2001**, *13*, 2272-2280.

19. Berrettini, M.G.; Braun, G.; Hu, J.G.; Strouse, G.F. *J. Am. Chem. Soc.* **2004**, *126* (22), 7063 -7070.
20. Cumberland, S. L.; Hanif, K. A.; Khitrov, G. A.; Javier, A.; Strouse, G. F.; Woessner, S. M.; Yun, C. S. *Chem. Mater.* **2002**, *14*, 1576-1584.
21. Badia, A.; Gao, W.; Singh, S.; Demers, L.; Cuccia, L.; Reven, L. *Langmuir* **1996**, *12*, 1262-1269.
22. Meulenber, R. W.; Bryan, S.; Yun, C. S.; Strouse, G. F. *J. Phys. Chem B* **2002**, *106*, 7774-7780.
23. Meulenber, R. W.; Strouse, G. F. *J. Phys. Chem. B* **2001**, *105*, 7438-7445.
24. Silverstein, R. M.; Bassler, G. C.; Morrill, T. C. *Spectrometric Identification of Organic Compounds*, 5th ed.; Wiley: New York, 1991.
25. Becerra, L. R.; Murray, C. B. et al. *J. Chem. Phys.* **1994**, *100*, 3297.

Chapter 3. NMR Analysis of Surfaces and Interfaces in 2-nm CdSe.

3.1. Introduction

CdSe nanocrystals, which are widely studied in the nanoscience community, provide a great model system to investigate the surface structure and interfaces for semiconductor nanocrystals, because of the presence of NMR active ^{113}Cd and ^{77}Se . As the nanomaterial is reduced in size, the contribution from surface to core species changes, leading to a condition where surface reconstruction should be observable by solid-state NMR methods, such as spin-echo and cross-polarization magic angle spinning (CPMAS) techniques. For this reason, a 2 nm CdSe-HDA particle was chosen in order to enhance our ability for a large surface to volume ratio.

In this chapter, 2-nm hexadecylamine-capped CdSe nanocrystals (CdSe-HDA) prepared by a single source precursor route¹ are studied through solid-state NMR experiments to further enhance our knowledge of the appearance of thiophenol and HDA passivation in the isolated particle (Chapter 2). The study also allowed for selective analysis of the nature of the internal and surface sites of cadmium and selenium, with regards to such important factors as crystallinity and atomic vacancies in the materials. Through analysis solid-state ^{77}Se and ^{113}Cd spin-echo, and CPMAS NMR experiments, as well as $^{113}\text{Cd}\{^1\text{H}\}$, and $^{77}\text{Se}\{^1\text{H}\}$ 2D heteronuclear chemical shift correlation (HETCOR) NMR experiments, a model of the surface and interfaces of this material was developed.

3.2 Experimental Section.

3.2.1. Synthesis of 2-nm CdSe Nanocrystals (CdSe-HDA).

CdSe nanocrystals were prepared by a previously published single source precursor method.¹ Approximately 2.1 g of $\text{Li}_4[\text{Cd}_{10}\text{Se}_4(\text{SC}_6\text{H}_5)_{16}]$ (0.653 mmol) was heated in 75 g of HDA to 120 °C under argon. The reaction progress was followed by UV-vis absorbance spectroscopy and removal from heat when the desired nanocrystal size of 2-nm was reached. After cooling to 50°C, the CdSe sample was precipitated by the addition of approximately 200 mL of methanol and was collected by centrifugation. Purification and size selection was accomplished by dissolution in a minimum amount of chloroform, reprecipitation by addition of methanol, and centrifugation (3×).

3.2.2 NMR.

Solid-state MAS NMR experiments were performed at room temperature on a Bruker 300 MHz Avance spectrometer with a 4-mm broadband MAS probe double tuned to ^1H (300.1 MHz) and the X channel to ^{77}Se (57.2 MHz), or ^{113}Cd (66.6 MHz). A spinning speed of 12 kHz was used in all experiments.

The chemical shifts of ^1H , ^{77}Se , and ^{113}Cd were referenced to TMS, $(\text{NH}_4)_2\text{SeO}_4$ (1040 ppm relative to $\text{Se}(\text{CH}_3)_2$ at 0 ppm), and $\text{Cd}(\text{ClO}_4)_2$, respectively.

The ^{113}Cd spin-echo experiment was performed with an acquisition time of 2.1 ms, a recycling delay of 120 s, and a 90° and 180° pulse length of 4.5 μs and 9 μs , respectively. The ^{77}Se spin-echo experiment was performed with an acquisition time of 1.6 ms, a recycling delay of 30 s, and a 90° and 180° pulse length of 5.6 μs and 11.2 μs , respectively.

The ^{113}Cd and ^{77}Se CPMAS experiments were acquired using TPPM ^1H decoupling, ramp cross-polarization (CP), an acquisition time of 2.1 ms, a recycling delay of 3 s, contact time ranging from 1 to 25 ms, and a ^1H 90° pulse length of 3 μs .

The 2D $^{113}\text{Cd}\{^1\text{H}\}$ HETCOR and 2D $^{77}\text{Se}\{^1\text{H}\}$ HETCOR experiments were acquired using ramp CP, TPPM ^1H decoupling, 14 400 scans for each t_1 point for a total of 64 t_1 points, an acquisition time of 1.1 ms, a dwell time of 2 μs , a recycling delay of 1 s, a contact time of 12 ms, and a ^1H 90° pulse length of 3 μs .

3.3. Results and Discussion.

3.3.1. Cadmium and Selenium Surface Structure.

Knowledge of the site homogeneity of cadmium and selenium on the surface and in the core of the particle can be gained by ^{113}Cd and ^{77}Se NMR experiments, including spin-echo and CPMAS. In Figure 3.1A, the ^{113}Cd spin-echo experiment for

CdSe-HDA measures all of the ^{113}Cd in the nanocrystal (core and surface) and was chosen because of its pulse sequence ($\pi/2$ - τ - π - τ -acquisition) being useful for materials with broad NMR peaks. The pulse sequence minimizes problems due to *rf* bleeding and receiver recovery. The ^1H - ^{113}Cd CPMAS experiment was conducted with contact times between 1 and 25 ms; a typical CPMAS spectra for 15 ms contact time is shown in Figure 3.1B. CPMAS measures only cadmium atoms at or near the surface of the particle because of polarization transfer from the abundant ^1H spins on the ligands to the ^{113}Cd spins via nuclear dipole-dipole interaction,^{2,3} which follows a $1/R^3$ distance dependence (normally $\sim 5 \text{ \AA}$ maximum). The peak shape and chemical shift is consistent throughout the various mixing times, while only the intensity changes because of building up of the signal with increasing mixing time, followed by a decrease through ^1H $T_{1\rho}$ relaxation.⁴⁻⁶

The main peak in both the spin-echo experiment and the CPMAS experiment is centered at 595 ppm, which is very near the bulk hexagonal CdSe value of 585 ppm (Figure 3.2B), suggesting a low level of reconstruction of cadmium in the particle or an insensitivity of cadmium to its chemical environment. Because of the chemical shift range of only 87 ppm between bulk and the precursor, $[\text{Li}]_4[\text{Cd}_{10}\text{Se}_4(\text{SC}_6\text{H}_5)_{16}]$ (Figure 3.2A), the latter appears to be most likely, which limits the usefulness of ^{113}Cd NMR for analysis of the reconstruction of cadmium sites. The broad feature of the ^{113}Cd spectra indicate chemical shift distribution and fast relaxation of cadmium atoms in the solid state. The spin-echo peak is broader than the CPMAS peak, which

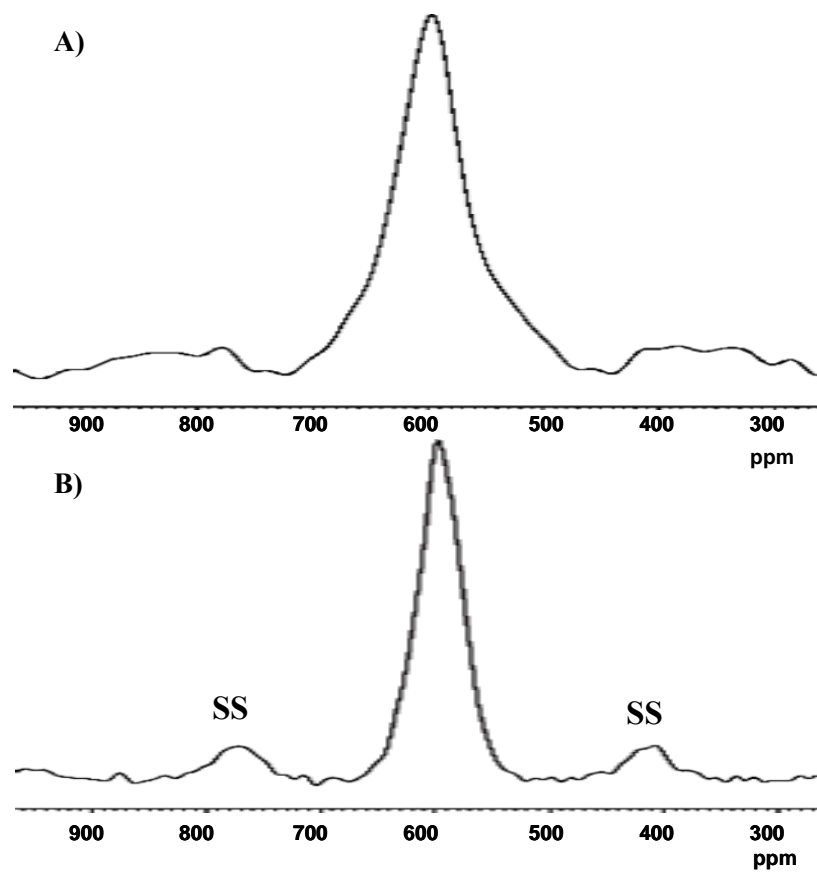


Figure 3.1. ^{113}Cd spin-echo and CPMAS NMR spectra of 2 nm CdSe-HDA. (A) ^{113}Cd spin-echo spectrum measures all the cadmium in the particle. (B) ^1H - ^{113}Cd CPMAS spectrum (15 ms contact time, τ) measures the surface or near-surface cadmium in the particle. Spinning side bands are marked with SS. (Spinning speed in A and B, 12 kHz)

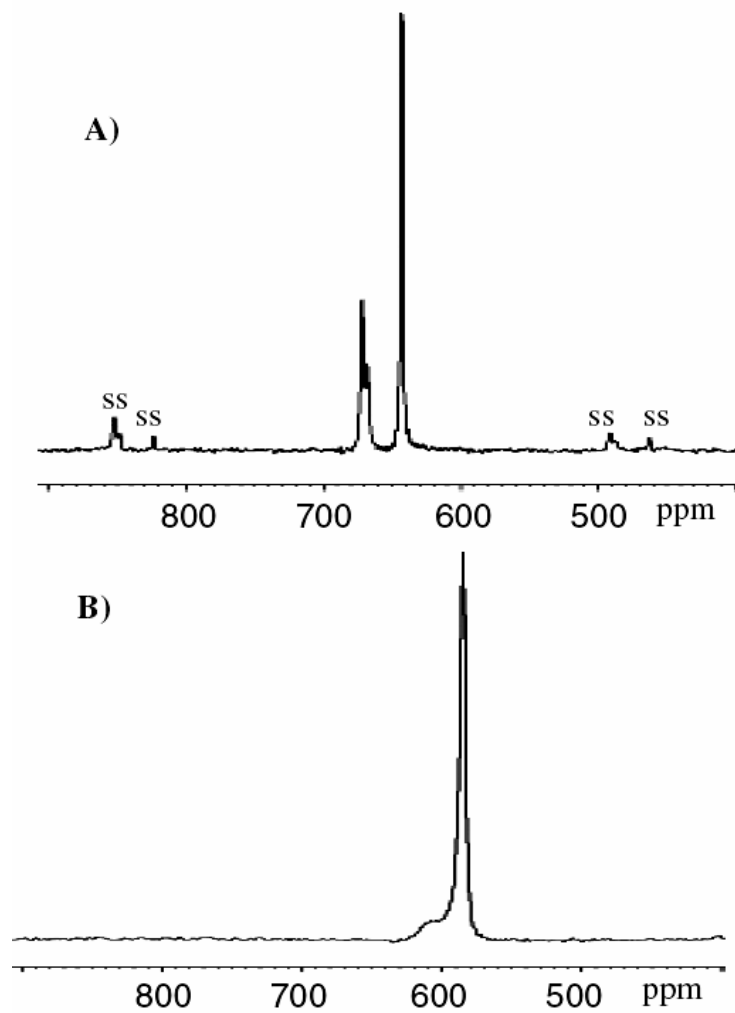


Figure 3.2. (A) ^{113}Cd CPMAS NMR spectrum of the precursor, $\text{Li}_4[\text{Se}_4\text{Cd}_{10}(\text{SPH})_{16}]$. The peak at 643 represents cadmium tetrahedrally coordinated to thiophenol. The peaks at 668 and 672 ppm represent axial and equatorial cadmium, respectively, that are coordinated to selenium and thiophenol; the spinning side bands of these cadmiums are marked with ss. (B) ^{113}Cd spin-echo NMR spectrum of bulk hexagonal CdSe. (Spinning speed in A and B, 12kHz)

arises from the larger distribution of chemical sites in the total particle (core and surface) relative to just the Cd sites on or near the surface probed by CPMAS spectra.⁷ Spinning sidebands, appearing at 410 and 775 ppm, are more pronounced in the ¹¹³Cd CPMAS spectra due to a more uneven electron density surrounding the cadmium atoms at the surface in comparison to the tetrahedral coordination surrounding the internal cadmium atoms.

The selenium NMR of the total Se atoms in the nanoparticle (spin-echo) and the Se atoms on or near the surface (CPMAS) for 2-nm CdSe-HDA are shown in Figure 3.3, with a line width and population analysis generated from a least-squares fit of the data in Table 3.1. Considering the error arising from a combination of instrumental and statistical contributions, the predicted error on the Se site shifts, line widths, and percentages are ± 2 ppm, ± 100 Hz, and $\pm 3\%$, respectively. This includes contributions from signal-to-noise and deconvolution of peaks. The percentage site occupancy error is determined by standard deviation analysis of data from all mixing times measured. The population is corrected for the ¹H-⁷⁷Se cross-relaxation time constants, T_{SeH} , which are shown in Table 3.2. To our knowledge, these are the first solid-state ⁷⁷Se NMR experiments on lyothermally prepared CdSe nanocrystals reported in the literature. In contrast to ¹¹³Cd NMR, the ⁷⁷Se spin-echo spectrum (Figure 3.3A) reveals a series of selenium sites at various chemical shifts with contributions from both the core and surface selenium atoms. This is not surprising since the sensitivity of the ⁷⁷Se to the chemical environment is more significant, as

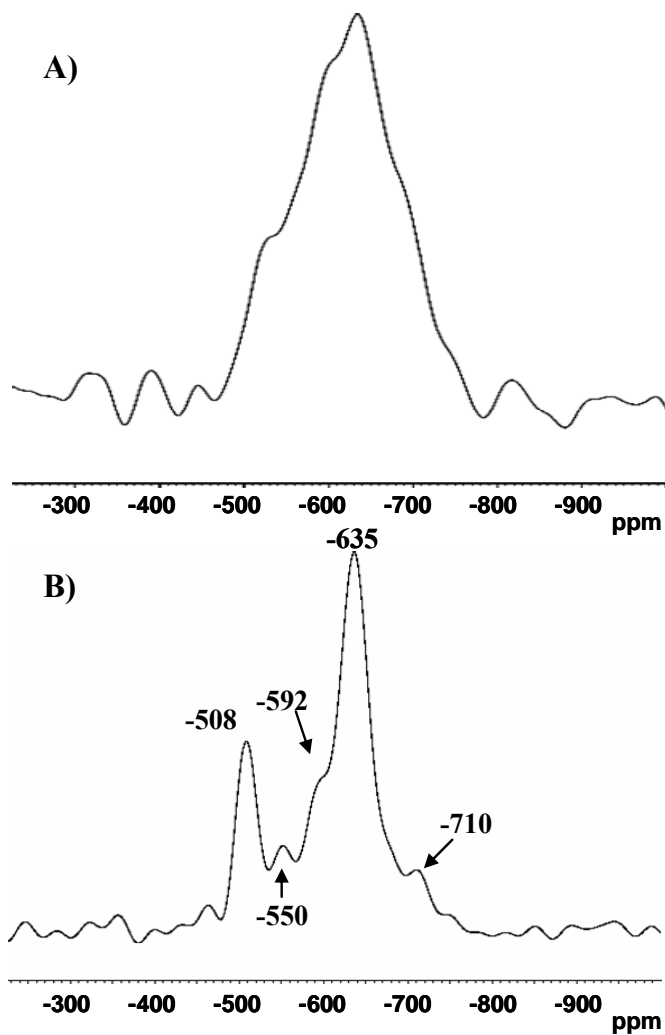


Figure 3.3. ^{77}Se spin-echo and CPMAS NMR spectra of 2 nm CdSe-HDA. (A) ^{77}Se spin-echo spectrum measures all of the selenium in the particle. (B) ^1H - ^{77}Se CPMAS spectrum (15 ms contact time, τ) measures the surface or near-surface selenium in the particle. (Spinning speed in A and B, 12 kHz)

Table 3.1. Analysis of the CPMAS ^{77}Se Sites Frequency, Line-Width, and Population Using a Linear Least Squares Fit of the Data at 15 ms Mixing Time *a*

Se site (ppm)	line width (Hz)	percentage
-508	1688	16
-550	1860	10
-592	1997	14
-635	2232	55
-676 ^b	1803	<5
-710 ^b	1946	<5

a The population is corrected for the ^1H - ^{77}Se cross-relaxation time constant T_{SeH} .

b The shoulder at -676 ppm and the less intense peak at -710 ppm are included in the deconvolution of the total spectra. However, because of the magnitude of error in measurement of this peak and estimation of T_{SeH} , no attempt to assign a percentage to the peak has been made.

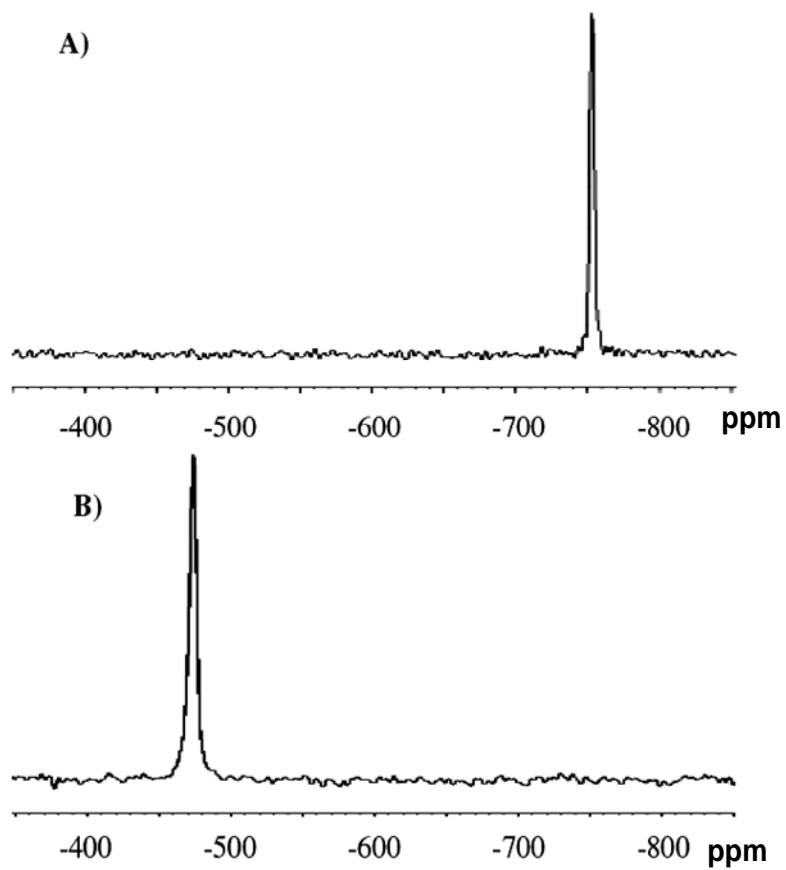


Figure 3.4. (A) ^{77}Se CPMAS NMR spectrum of the precursor, $\text{Li}_4[\text{Se}_4\text{Cd}_{10}(\text{SPH})_{16}]$.
(B) ^{77}Se spin-echo NMR spectrum of bulk hexagonal CdSe.
(Spinning speed in A and B, 12kHz)

seen by a larger chemical shift range of 275 ppm between selenium in bulk CdSe and selenium in the precursor (Figure 3.4). The center of the largest peak in the spin-echo spectrum is at -635 ppm (Figure 3.3A) and correlates with the largest peak observed in the ^1H - ^{77}Se CPMAS (Figure 3.3B) spectra. This suggests that the signal arises from selenium at or near the surface of the 2-nm particle, with the spin-echo signature reflecting the ~48% of the particle being attributable to surface atoms relative to the core atoms in this size regime.⁸

The presence of five narrow ^{77}Se peaks being observed in the ^1H - ^{77}Se CPMAS spectra (Figure 3.3B), at -508, -550, -592, -635, and -710 ppm is surprising. This observation suggests that the surfaces of the 2-nm particles represent reconstructed sites that remain largely ordered in the structure rather than forming an amorphous ensemble structure. If the nanomaterials were amorphous, a single broad peak would have been expected. Repeating this experiment while varying the contact time, τ , between 1 and 25 ms, indicates no new features and only intensity changes due to building up of the signal with increasing contact time followed by a decrease due to $T_{1\rho}$ relaxation.

The nature and position of the five sites can be investigated by the ^1H - ^{77}Se cross-relaxation time constants, T_{SeH} . The integrated ^{77}Se peak intensities from ^1H - ^{77}Se CPMAS were plotted as a function of the contact time, τ . The proton spin-lattice time constant, $T_{1\rho}$, was determined following a procedure from a previous publication.⁵ The plot was fit to equation 3.1⁹ using nonlinear least-squares analysis to determine T_{SeH} . The fitted plots are shown in Figure 3.5.

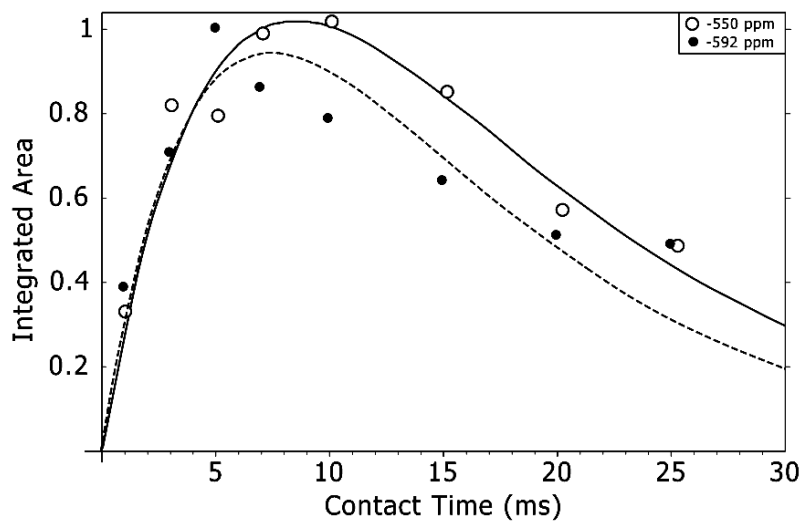
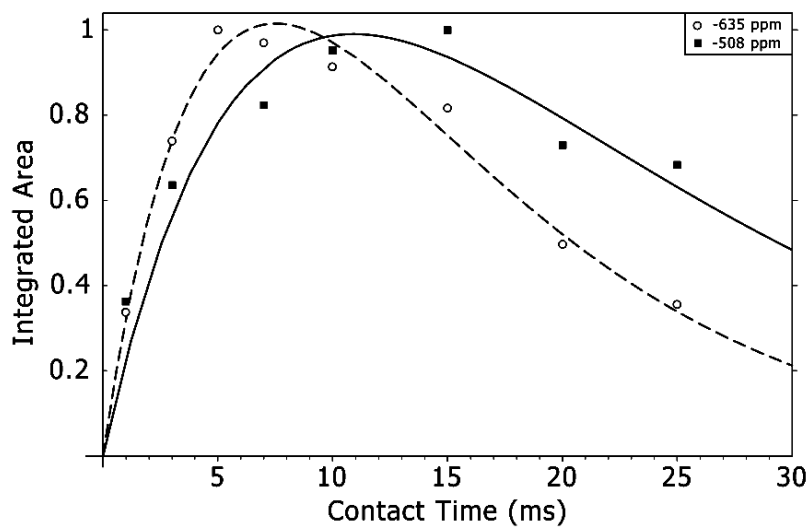


Figure 3.5. The integrated ^{77}Se peak intensities from ^1H - ^{77}Se CPMAS were plotted as a function of contact time, τ . The plot was fit to equation 1 using a nonlinear least squares analysis to determine the cross-relaxation time constants, T_{SeH} .

$$M(\tau) = M_0(\exp(-\tau/T_{1\rho\text{H}}) - \exp(-\tau/T_{\text{SeH}}))/(1 - T_{\text{SeH}}/T_{1\rho\text{H}}) \quad (3.1)$$

The magnitude of T_{SeH} is dependent on the intermolecular distance between ^1H and ^{77}Se centers. Assuming that the surface seleniums have similar mobility, the cross-relaxation time constant has a $1/R^6$ distance dependence and can be used to compare distances.⁶ The values of T_{SeH} for four out of the five sites of selenium are summarized in Table 3.2.

The plot of intensity versus contact time for the ^{77}Se peak at -710 ppm was not fit because of the poor signal-to-noise ratio. The peaks at -550, -592, and -635 ppm all have similar cross-relaxation time constants, with T_{SeH} values of 8.0, 5.9, and 6.4 ms (Table 3.2), respectively, indicating similar average distances between these Se sites and the ligand protons.

In addition, these Se sites are closer to ligand protons than the Se sites at -508 ppm, as reflected by the larger T_{SeH} value (13.5 ms) of the latter. This is consistent with the assignment of -508 ppm as an internal Se site (one layer down). With this information, we conclude that the peaks at -550, -592, and -635 ppm all represent surface sites. If we approximate the intensity of the peaks as a measure of the number of seleniums in each site (Table 3.1), which is reasonable based on the similar value for T_{SeH} for these sites, then the series of peaks from -550 to -635 ppm would represent increasing selenium occupation in each site. Considering the site

Table 3.2.
2-nm CdSe-HDA ^{77}Se Cross-Relaxation
Time Constants, T_{SeH} , (milliseconds)

^{77}Se peak (ppm)	T_{SeH} (ms)
-508	13.5 ± 0.5
-550	8.0 ± 0.5
-592	5.9 ± 0.5
-635	6.4 ± 0.5

occupation and available types of sites on a 2-nm CdSe, we believe that the sites at -550, -592, and -635 ppm represent selenium occupying a vertex, edge, and facet site on the nanoparticle, respectively. The chemical shift decrease from vertex to facet site also supports the assignment because of a facet site most likely being more shielded from increased ligand density than a vertex or edge; using the same argument, an edge site will be more shielded than a vertex. From the chemical shift of the peak at -710 ppm, a likely assignment for this peak would be a facet site reconstructed differently than the peak at -635 ppm. Taking into account that the peak at -508 ppm is at a longer distance from the ligand protons and that its chemical shift is closest to the bulk ^{77}Se value of -474 ppm (Figure 3.4A), we conclude that the -508 ppm site arises from the tetrahedrally coordinated selenium site one layer down from the surface. The observation of shift in the NMR signatures for the selenium sites from bulk supports particle reconstruction both at the surface and within the 2-nm CdSe nanoparticle.

3.3.2 Thiophenol vs HDA Site Occupation.

As shown in Chapter 2 by investigation of the $^{13}\text{C}\{^1\text{H}\}$ frequency-switched Lee-Goldberg (FSLG) HETCOR experiment, thiophenol and HDA appear to be residing on the same facets in CdSe-HDA. The lack of face selective binding in conjunction with the interesting recapping results (Chapter 2) indicate a special site of binding for thiophenol in the material. Correlated $^{113}\text{Cd}\{^1\text{H}\}$ and $^{77}\text{Se}\{^1\text{H}\}$ NMR

experiments provide direct evidence of the interaction and site occupation and of the thiophenol and HDA ligands with cadmium and selenium surface and near surface atoms.

The $^{113}\text{Cd}\{^1\text{H}\}$ HETCOR experiment is shown in Figure 3.6, with separately measured single pulse ^1H MAS in a traditional and magnified view and ^1H - ^{113}Cd CPMAS spectra on the vertical and horizontal axes, respectively. There is a correlation of the ^1H region of HDA between approximately -0.8 to 1.8 ppm, with the surface cadmium centered at 595 ppm. There is also a correlation with the thiophenol protons centered at 6.79 ppm to this cadmium peak. This information provides direct proof that the protons on HDA and thiophenol are strongly interacting with the surface cadmium, which is consistent with both ligands being bound to cadmiums on the surface of the particle.

The $^{77}\text{Se}\{^1\text{H}\}$ HETCOR experiment is shown in Figure 3.7, with separately measured single pulse ^1H MAS on the vertical axis in a traditional and magnified view and ^1H - ^{77}Se CPMAS spectra on the horizontal axis, respectively. There are five correlation peaks between the methylene chain of HDA and the five selenium sites. An amine-selenium bond is unlikely; therefore, we have concluded that these correlations signify that the methylene protons of HDA strongly interact with the selenium sites, arising from a chain tilt of HDA on nearby cadmium atoms toward the surface. This type of configuration would allow the chain to be in a close proximity to selenium as shown in Figure 3.8A, consistent with previous work on CdSe that

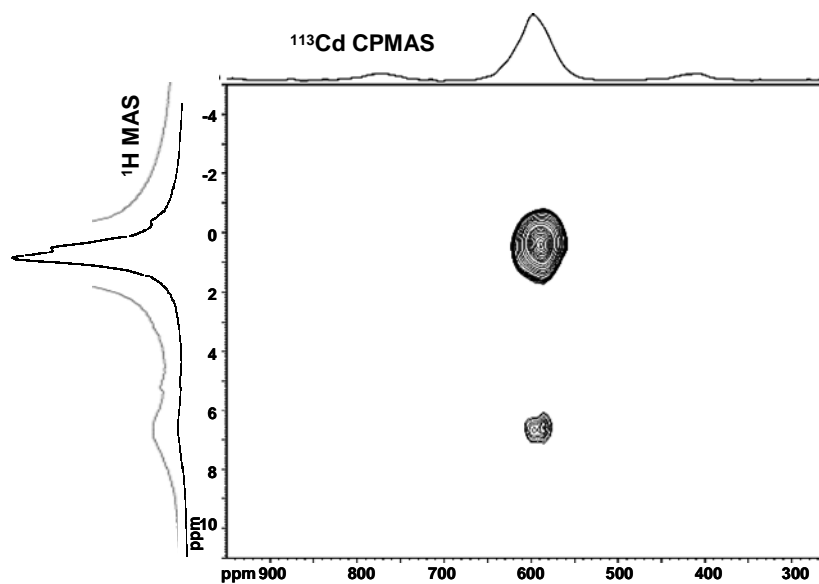


Figure 3.6. 2D $^{113}\text{Cd}\{^1\text{H}\}$ HETCOR NMR of 2nm CdSe-HDA. Separate single pulse ^1H MAS and ^1H - ^{113}Cd CPMAS spectra reside along the vertical and horizontal axes of the contour plot, respectively. The HETCOR correlations show that the surface cadmium are interacting strongly with the HDA methylene chain protons and with the protons of thiophenol, consistent with HDA and thiophenol bound to cadmium on the surface of the particle. (Spinning speed, 12 kHz; contact time, 12 ms.)

indicated a maximum chain tilt toward the surface at small nanocrystal sizes.¹⁰ Unfortunately, because of the length of time for this experiment (504 h), it was not possible to repeat the experimental measurements at various mixing times; however, we believe spin diffusion is not a significant contribution to the observation because of the high spinning speed, different $T_{1\rho}$ values for protons on the HDA chain, and that FSLG homonuclear ^1H decoupling does not significantly improve ^1H resolution in the indirect dimension in ^{13}C and ^{113}Cd HETCOR NMR. There are no correlations between the selenium sites and thiophenol, which indicates that the thiophenol protons are not in close proximity to selenium, and more importantly, the five observed selenium sites in the 2-nm CdSe nanocrystal do not arise from thiophenol binding.

3.3.3. Structural Model.

The combined experimental results lead to a structural model for the surface of a 2-nm CdSe as shown in Figure 3.8. The site occupation of thiophenol on cadmium and the information that the thiophenol protons are not in close proximity to any of the selenium sites from the $^{77}\text{Se}\{^1\text{H}\}$ HETCOR experiment strongly suggests a unique cadmium site occupation. A likely model would be thiophenol filling selenium vacancies (Figure 3.8B,C) on the surface of the particle. In this configuration, the protons on thiophenol would not be in close proximity to selenium on the surface of the particle as seen in the $^{77}\text{Se}\{^1\text{H}\}$ HETCOR experiment (Figure 7). This type of interaction also supports the presence of thiophenol from the reaction and the

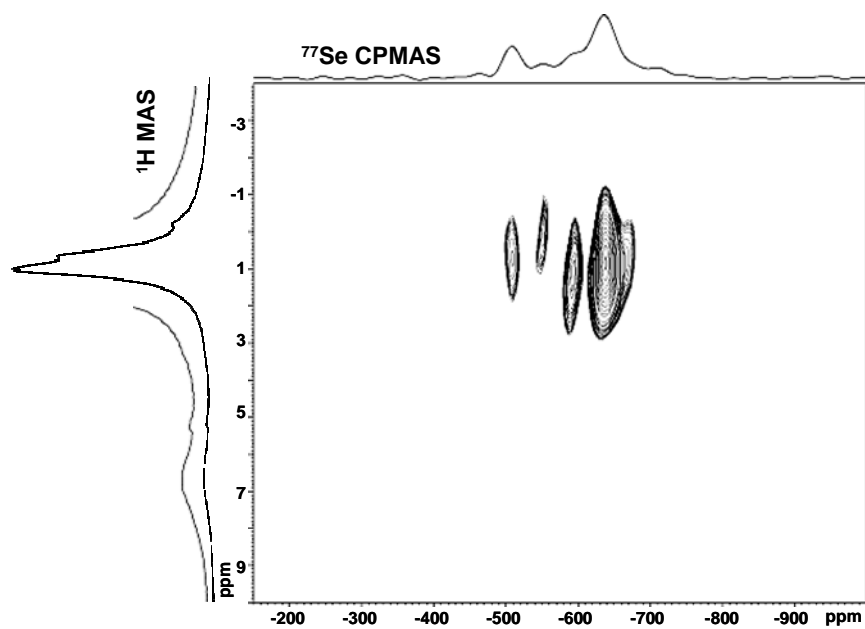


Figure 3.7. 2D $^{77}\text{Se}\{^1\text{H}\}$ HETCOR NMR of 2nm CdSe-HDA. Separate single pulse $^1\text{H MAS}$ and $^1\text{H}\text{-}^{77}\text{Se CPMAS}$ spectra reside along the vertical and horizontal axes of the contour plot, respectively. The HETCOR correlations determine that the five separate Se sites are interacting strongly with the HDA methylene chain protons consistent with a chain tilt of HDA to the surface. (Spinning speed, 12 kHz; contact time, 12 ms.)

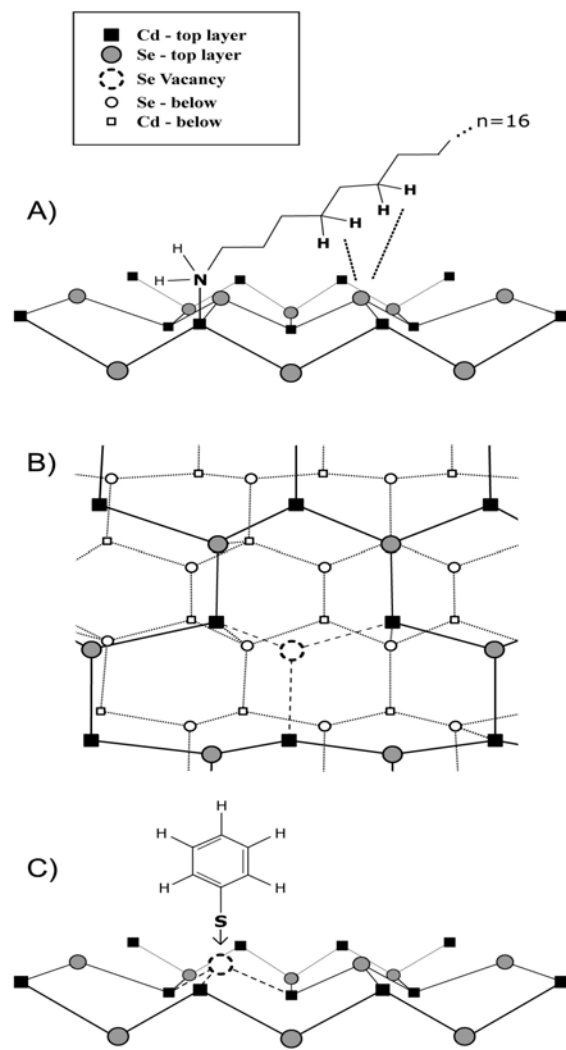


Figure 3.8. Structural Model of 2 nm CdSe-HDA **(A)** Chain tilt of HDA to the surface of the particle. **(B)** Selenium vacancy on the surface of a CdSe nanocrystal. **(C)** A thiophenol molecule filling a selenium vacancy.

recapping results since HDA (or pyridine) would not be able to fill a vacancy due to bonding restraints. Therefore, although thiophenol is not a strong ligand and is in a small amount in the reaction mixture, it is the only ligand available to fill a selenium vacancy.

3.4. Conclusions.

A model of the surfaces and interfaces of 2-nm CdSe nanocrystals synthesized from a single source precursor method has been constructed by solid-state NMR experiments. This model includes the presence of thiophenol and HDA ligands on the surface of the particle characterized by solution and solid-state ^{13}C NMR (Chapter 2). It was established through $^{113}\text{Cd}\{^1\text{H}\}$ HETCOR NMR that these ligands are bound to the surface through bonds to surface cadmium atoms. ^{77}Se CPMAS NMR indicates five sites for selenium, which can be correlated to facet, edge, or vertex sites and to selenium a layer deep. This technique also suggests a largely crystalline surface with selenium site reconstruction. $^{77}\text{Se}\{^1\text{H}\}$ HETCOR NMR establishes the close proximity of selenium to the HDA chain, which supports a chain tilt of the HDA to the surface of the particle. This experiment also establishes that thiophenol is not in close proximity to the five selenium sites. The combination of these results and various ligand exchange results (Chapter 2) suggest that thiophenol is filling selenium vacancies on the surface.

3.5. References

1. Cumberland, S. L.; Hanif, K. A.; Khitrov, G. A.; Javier, A.; Strouse, G. F.; Woessner, S. M.; Yun, C. S. *Chem. Mater.* **2002**, *14*, 1576-1584.
2. Ladizhansky, V.; Hodes, G.; Vega, S. *J. Phys. Chem. B* **1998**, *102*, 8505-8509.
3. Elbaum, R.; Vega, S.; Hodes, G. *Chem. Mater.* **2001**, *13*, 2272-2280.
4. Gabrielse, W.; Gaur, A. G.; Feyen, F. C.; Veeman, W. S. *Macromolecules* **1994**, *27*, 5811-5820.
5. Voelkel, R. *Angew. Chem., Int. Ed. Engl.* **1988**, *27*, 1468-1483.
6. Klein Douwel, C. H.; Maas, W. E. J. R.; Veeman, W. S.; Werumeus Buning, G. H.; Vankan, J. M. J. *Macromolecules* **1990**, *23*, 406-412.
7. Mikulec, F. V.; Kuno, M.; Bennati, M.; Hall, D. A.; Griffin, R. G.; Bawendi, M. G. *J. Am. Chem. Soc.* **2000**, *122*, 2532-2540.
8. The value of 46-50% surface atoms, defined as the ratio of atoms with dangling bonds to total atoms, was determined from analyzing several near-spherical, faceted ~2-nm CdSe wurtzite crystals (170-195 atoms) created in Crystal Impact's Diamond

software, with singly bound atoms removed. C_{3v} point group symmetry and the lattice parameters $a = 4.3\text{\AA}$, $c = 7.0\text{\AA}$ were used for this estimate.

9. Mehring, M. *High-Resolution NMR Spectroscopy in Solids*; Springer-Verlag: New York, 1976.

10. Meulenberg, R. W.; Strouse, G. F. *J. Phys. Chem. B* **2001**, *105*, 7438-7445.

Chapter 4. Size-Dependent Solid-State ^{77}Se NMR Study of CdSe Nanocrystals.

4.1. Introduction.

Semiconductor nanocrystals, which are widely studied by optical spectroscopies, exhibit unique size-dependent properties that are strongly influenced by reconstruction of the surface and lattice of the material.¹⁻⁵ Although these studies have provided vital information for these materials, the optical excitations are delocalized and therefore respond to an average environment of the nanocrystal. Solid-state nuclear magnetic spectroscopy (NMR) in contrast, is sensitive to local electronic and chemical environments and, by utilizing special pulse sequences, has been shown to selectively probe distinct regions of the nanocrystal.⁶⁻¹¹ This technique therefore provides an extremely powerful and complimentary tool to optical spectroscopies for probing the surface, near surface, and core species of semiconductor nanocrystals to better understand the distinct size-dependent properties of these selective regions in relation to the particle as a whole.

In this chapter, a solid-state ^{77}Se NMR study of CdSe nanocrystals ranging in size from 2 – 4 nm, prepared by a single-source precursor route¹² is reported. Through ^{77}Se spin-echo and cross-polarization (CP) magic angle spinning (MAS) NMR, selective regions of the nanocrystal were studied providing information on the differing nature of reconstruction of the surface, near-surface and core sites with nanocrystal size.

4.2. Experimental Section.

4.2.1. Synthesis of ^{77}Se enriched CdSe nanocrystals (CdSe-HDA).

^{77}Se enriched CdSe nanocrystals were prepared with a modification of a previously published single source precursor method.¹² Briefly, a ^{77}Se enriched precursor, $\text{Li}_4[\text{Cd}_{10}^{77}\text{Se}_4(\text{SC}_6\text{H}_5)_{16}]$, was synthesized by replacement of elemental Se with elemental ^{77}Se , in the reaction.¹³ The isotopically enriched precursor was used in conjunction with unenriched precursor following the literature preparation¹² to synthesize particles with diameters of 2.5 nm, 2.9 nm, 3.7 nm, and 4 nm CdSe with ~50 % ^{77}Se enrichment in the material in order to increase the signal to noise ratio in the NMR measurements. The 2 nm particles were prepared as previously reported⁶ and do not contain ^{77}Se enrichment.

4.2.2. NMR.

Solid-state MAS NMR experiments were performed at room temperature on a Varian 500 MHz wide-bore Unity/Inova spectrometer with a 4-mm broadband MAS probe double tuned to ^1H (500.1 MHz) and the X channel to ^{77}Se (95.4 MHz). A spinning speed of 14 kHz was used in all experiments. The chemical shift of ^{77}Se was referenced to $(\text{NH}_4)_2\text{SeO}_4$ (1040 ppm relative to $\text{Se}(\text{CH}_3)_2$ at 0 ppm).

The ^{77}Se spin-echo experiments were performed with an acquisition time of 1.6 ms, a recycling delay of 180 s, and a 90° and 180° pulse length of 3.25 μs and 6.5 μs , respectively. The ^{77}Se CPMAS experiments were acquired using TPPM ^1H

decoupling, ramp cross-polarization (CP), an acquisition time of 1 ms, a recycling delay of 3 s, contact times ranging 2 to 25 ms, and a ^1H 90° pulse length of 4 μs .

4.3. Results and Discussion.

4.3.1. ^{77}Se Spin-Echo NMR: Surface and Core Components.

The ^{77}Se spin-echo MAS spectra of 2.5 nm, 2.9 nm, 3.7 nm, and 4 nm CdSe-HDA are shown in Figure 4.1A-D, respectively, with bulk hexagonal CdSe shown in Figure 4.1E; the vertical dashed line is added to aid in interpretation of the data. Spin-echo NMR is useful for broad NMR resonances and probes the ^{77}Se in the entire nanocrystal. Therefore, Figure 4.1 compares the chemical shifts of the core and surface components of the nanocrystals. Inspection of the spectra indicates an apparent increasing chemical shift downfield towards the ^{77}Se bulk chemical shift value of -473 ppm, as well as a decreasing breadth of the signal with increasing nanocrystal size. To investigate these interesting observations, the surface selenium to core selenium contributions in these sizes must be taken into account. The ratio of surface atoms to core atoms for a 2 nm, 2.5 nm, 2.9 nm, 3.7 nm and 4 nm CdSe particle is $\sim 1.0, 0.71, 0.54, 0.37$ and 0.35 , respectively.¹⁴ Therefore, the contribution from surface sites to the total ^{77}Se spin-echo measurement largely decreases with increase in nanocrystal size. In order to analyze and attempt quantification of the

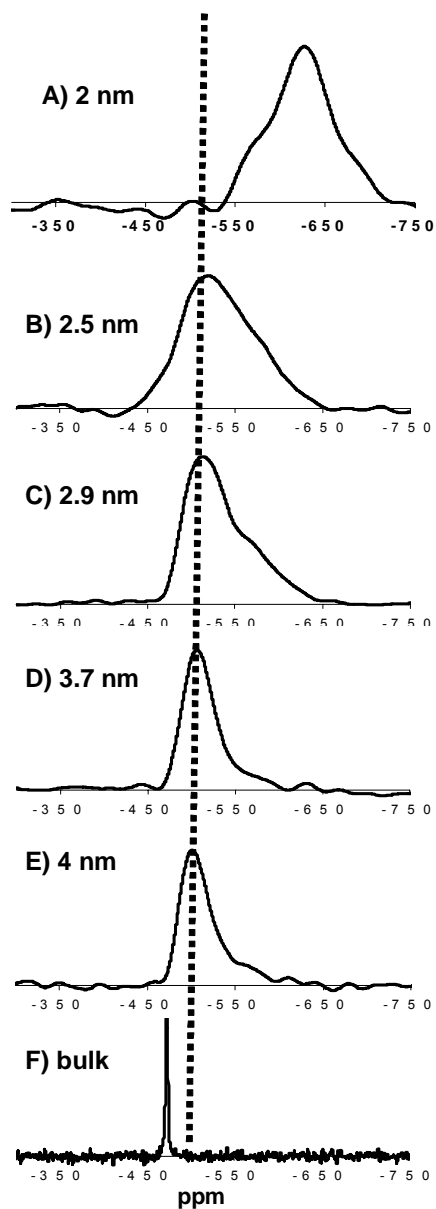


Figure 4.1. ^{77}Se spin-echo MAS NMR spectra of (A) 2 nm (B) 2.5 nm (C) 2.9 nm (D) 3.7 nm and (E) 4 nm CdSe nanocrystals, demonstrating a decreasing broadening and increasing chemical shift downfield with increasing nanocrystal size. Bulk CdSe ^{77}Se spin-echo MAS NMR spectrum is shown in (F). The vertical dashed line is added to aid in interpretation of the data. (Spinning speed, 14 kHz)

surface to core components from the ^{77}Se spin-echo results, the spectra were fit well to 2 gaussian peaks utilizing Igor software for 2.5 - 4 nm particles and 3 gaussian peaks for the 2 nm particles. Examples of the core and surface fitted peaks for the 2 – 4nm CdSe-HDA particles are shown in Figure 4.2A-D. The downfield component is characterized as the core species the upfield component represents surface and near surface selenium for 2.5- 4nm CdSe-HDA. These assignments are supported by of the chemical shift of the core species being nearest to the chemical shift of bulk CdSe and also due to the ratio of the upfield to downfield peak changing with size. This decreases the apparent broadness of the ^{77}Se signal as the surface component contribution decreases with increasing size. The chemical shift of the surface is expected to be furthest away from the bulk value of CdSe as more reconstruction is expected in this domain of the material due to strain and ligand effects. Also supporting this assignment is the results of CPMAS experiments (Figure 4.5-4.6), which selectively measure surface species, yielding selenium peaks most near the surface appearing upfield of selenium one or two monolayers within the particle surface. This assignment was also confirmed from a previous study on 2 nm CdSe-HDA.⁶ Therefore, the ^{77}Se spin-echo chemical shifts of the core components for 2.5 nm, 2.9 nm, 3.7 nm and 4 nm are -509 ppm, -510 ppm, -506 ppm, and -502 ppm with errors of ± 2 ppm taking instrumental drift and deconvolution into consideration. The linewidths of these respective peaks decrease with size from 70 ppm, 47 ppm, 39 ppm, and 34 ppm. Due to the extremely small amount of core atoms in the 2 nm size regime with $\sim 50\%$ ^{6,14} of the atoms residing on the surface and poor signal to noise in

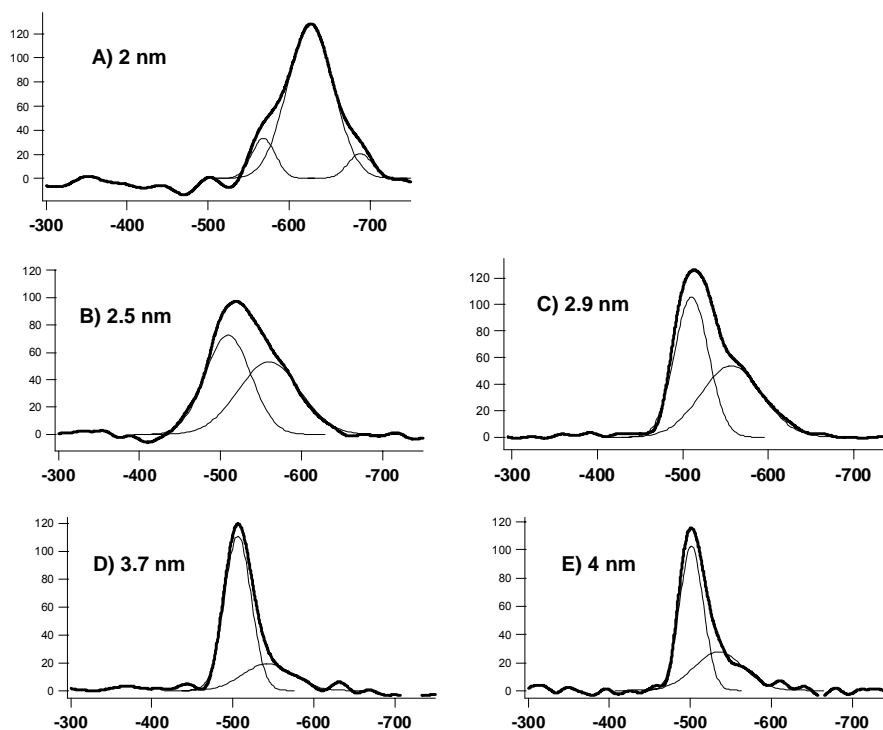


Figure 4.2. ^{77}Se spin-echo MAS NMR spectra with fitted gaussian peaks separating the spectra into surface and core selenium components for 2 nm (B) 2.5 (C) 2.9 nm (D) 3.7 nm and (E) 4 nm CdSe-HDA nanocrystals. For B-E the downfield peak represents the core components and the upfield peak represents surface components. Due to the small amount of core selenium in addition to poor S/N, the 2 nm particle is more difficult to characterize as two distinct regions and has been fit better to 3 gaussians. The small peak at -508 ppm is real due to appearance in the CPMAS spectra (Figure 4.5) and appears most “core” like as it is most near the ^{77}Se chemical shift of bulk CdSe.

the unenriched 2 nm spin-echo spectrum, the core chemical shift is difficult to characterize with this technique. But, inspection of the CPMAS data (Figure 4.3A) and data from a previous publication,⁶ the small peak at -508 ppm (Figure 4.1A) was concluded as real and chosen as the core component due to its chemical shift nearest of bulk and the distant dependence of the cross-polarization time constant, T_{SeH} indicating the species in a sub-surface lattice site.⁶ The linewidth of 20 ppm was taken from the CPMAS data due to the inability to fit the spin-echo for this peak and therefore may have much more error associated with it.

The surface components of the ⁷⁷Se spin-echo peaks shift downfield with increasing size from -568/-623 ppm, -560 ppm, -557 ppm, -544 pm, to -507 ppm (± 2 ppm) for the series of 2 nm - 4 nm CdSe-HDA. In analogy to the core components, the linewidths of these surface species also decrease with size for 2.5 nm - 4 nm particles with values of 70 ppm, 47 ppm, 39 ppm, and 34 ppm. This decrease in linewidth for the surface and core components with decreasing size indicates a decreasing chemical shift distribution in the core and surface components with size. Interesting, the size distribution of the particles are similar ($\sim 5\%$), and therefore, the decrease in chemical shift distribution with size suggests that as the particles grow larger, the selenium atoms contributing to the surface and core components become more ordered. This increased order with increasing size can be related to strain effects. With small sized nanocrystals, the surface is largely strained and with small numbers of core atoms, there is very little space for overcoming bond-changes and other reconstructions from the surface strain. But, as the particles get larger, surface

strain decreases and there is many more atoms internally to overcome any bond changes and yields more room for a crystalline ordered core not affected by the surface confinement. Hence, in the larger sizes, a more crystalline ordered surface and core can be expected.

Due to the large amount of surface sites dominating the 2 nm CdSe spin-echo spectrum, poor signal to noise, and the inability to fit well to a core and surface component, the peak at -568 ppm was chosen for the surface component used in plotting from correlating best with the data from the other sizes. Large amounts of surface reconstruction are likely at such small sizes and this site seems most closely related structurally and electronically with the surface components probed by spin-echo in the other sizes studied. The center of gravity of -623 ppm was also used for the 2 nm to give an overall surface component peak. The experimental ratio from the spin-echo spectra calculated from the area of the peaks representing surface and core components for 2.5, 2.9, 3.7, and 4 nm CdSe are 1.0, 0.91, 0.32, and 0.55 which differ quite significantly with the calculated values with the exception of the 3.7 nm particle. A ratio was not calculated for the 2 nm particle because of the inability to fit the spin-echo core component due to poor signal to noise. The chemical shifts, linewidths, experimental and calculated ratios of surface to core atoms from the ^{77}Se spin-echo results are summarized in Table 4.1; spin-echo NMR values for bulk CdSe and the precursor, $\text{Li}_4[\text{Cd}_{10}\text{Se}_4(\text{SC}_6\text{H}_5)_{16}]$, as well as the center of gravity of the ^{77}Se spin-echo spectra are also included.

Table 4.1. Summary of ^{77}Se chemical shifts, linewidths, center of gravity and calculated and measured surface to core ratios for spin-echo and CPMAS (15 ms contact time) data for $\text{Li}_4[\text{Cd}_{10}\text{Se}_4(\text{SC}_6\text{H}_5)_{16}]$, 2 nm, 2.5 nm, 2.9 nm, 3.7 nm, 4 nm and bulk CdSe.

Nanocrystal Size/ Material	^{77}Se Spin-Echo Chemical Shift (core component)	Linewidth (ppm)	^{77}Se Spin-Echo Chemical Shift (surface component)	Linewidth (ppm)	Calculated Surface to Core Ratio	Measured Surface to Core Ratio (spin-echo)	Center of Gravity (spin-echo)	^{77}Se CPMAS Chemical Shift (near surface peak)	Linewidth (ppm)	Center of Gravity (CPMAS)
2 nm	$-508 \pm 2 \text{ ppm}_a$	20_a	$-568/-623 \pm 2 \text{ ppm}_b$	35_b	1.0	c	-623 ppm	$-508 \pm 2 \text{ ppm}$	26	-605 ppm
2.5 nm	$-509 \pm 2 \text{ ppm}$	70	$-560 \pm 2 \text{ ppm}$	91	0.71	1.0	-533 ppm	$-513 \pm 2 \text{ ppm}$	35	-570 ppm
2.9 nm	$-510 \pm 2 \text{ ppm}$	47	$-557 \pm 2 \text{ ppm}$	84	0.55	0.91	-532 ppm	$-519 \pm 2 \text{ ppm}$	64	-566 ppm
3.7 nm	$-506 \pm 2 \text{ ppm}$	39	$-544 \pm 2 \text{ ppm}$	73	0.38	0.32	-515 ppm	$-511 \pm 2 \text{ ppm}$	47	-563 ppm
4 nm	$-502 \pm 2 \text{ ppm}$	34	$-507 \pm 2 \text{ ppm}$	51	0.35	0.55	-514 ppm	$-507 \pm 2 \text{ ppm}$	48	-553 ppm
Bulk CdSe	$-473 \pm 2 \text{ ppm}$	3	—	—	—	—	-473 ppm	—	—	—
$\text{Li}_4[\text{Cd}_{10}\text{Se}_4(\text{SC}_6\text{H}_5)_{16}]$	$-748 \pm 2 \text{ ppm}$	3	—	—	—	—	-748 ppm	—	3	-748 ppm_d

a Due to poor signal to noise in the 2 nm spin-echo spectrum and small amount of core peaks in this size regime, this peak was chosen based upon its appearance in the CPMAS spectrum and due to it being the most “core” like from its chemical shift. The linewidth was taken from the CPMAS data due to the inability to fit the spin-echo for this peak.

b Due to the large amount of surface sites dominating the 2 nm CdSe spin-echo spectrum, the spin-echo was not able to be fit to 2 peaks, and therefore -568 ppm was chosen from its correlating best with the data from the other sizes and -623 ppm (center of gravity) was chosen also for comparison. The linewidth is from the -568 ppm peak.

c A ratio was not calculated from the spin-echo because of the inability to fit the spin-echo core component due to poor signal to noise.

d All Se sites are equal in the CPMAS.

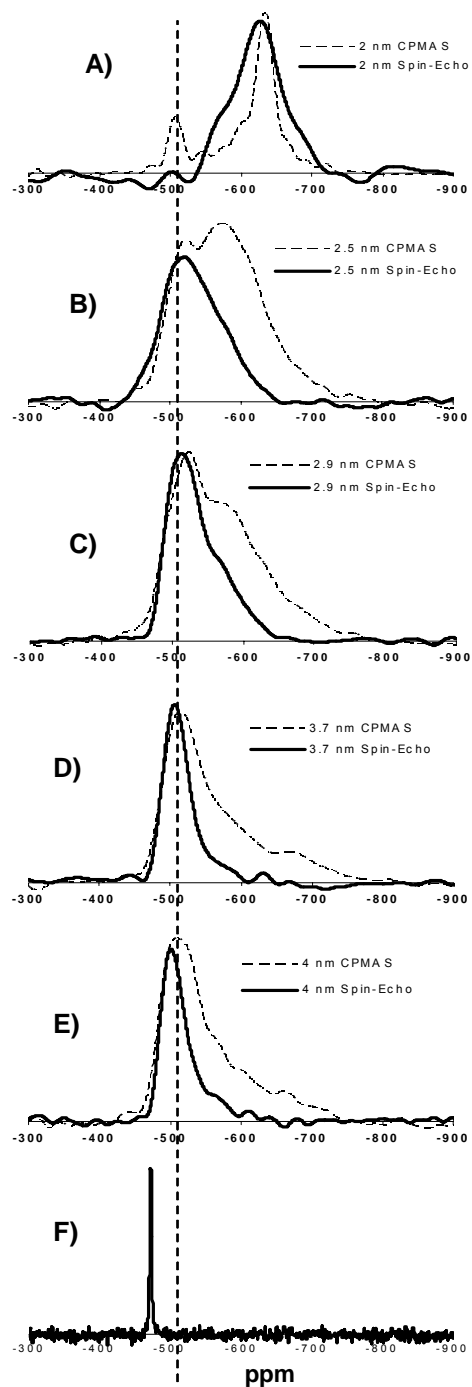
The values for the surface to core ratios for the 2.5 nm, 2.9 nm and 4 nm are much larger than expected suggesting that particle reconstruction is occurring within the particle. The chemical shift of the core in the sizes studied appearing upfield of bulk CdSe suggests a degree of reconstruction in this domain as the Se are more shielded in the NC's than bulk CdSe; but, with the bulk hexagonal crystal structure typically adopted in nanocrystalline CdSe sizes above 2 nm as evidenced by X-ray diffraction studies,¹⁵ the degree of reconstruction in the core can be postulated as less than the surface sites. With this assumption, we are considering the core domain (the downfield Gaussian in the spin-echos) as largely unreconstructed and the surface component (the upfield Gaussian peak in the spin-echo) as largely reconstructed from bulk hexagonal CdSe. Therefore, this ratio can be an indication to the extent of reconstruction (ie bond length, strain, electronic differences, ligand effects) within the particle by the more it differs from the calculated values. Only for the 3.7 nm particles, the ratio from the spin-echo is very similar to a calculated value for reconstruction occurring only on the surface atoms. This is very intriguing since we have seen a stalling in this single-source precursor synthesis at this size that entails dilute conditions and/or increased pressure to overcome. This could suggest that the stalling is the result of a very stable 3.7 nm particle from the very low degree of surface reconstruction within the particle. Inspection of the 2.9 nm particle reveals the most differing ratio than expected in the sizes studies suggesting the largest extent of particle reconstruction within the selenium sub-lattice of the material in this size

regime. To further investigate this reconstruction within specific domains of the surface, ^1H - ^{77}Se CPMAS experiments were acquired.

4.3.2. ^{77}Se CPMAS NMR: Surface and Near Surface Species.

The ^1H - ^{77}Se CPMAS experiments of the nanocrystals measure only selenium atoms at or near the surface of the particle due to polarization transfer from the abundant ^1H spins on the passivating ligands to the ^{77}Se spins through a nuclear dipole-dipole interaction,^{7,8} which follows a $1/R^3$ distance dependence. From a previous publication⁶, it was indicated through 2D $^{77}\text{Se}\{^1\text{H}\}$ HETCOR NMR that the surface Se in CdSe-HDA are interacting strongly the protons of the HDA chain. Therefore, this technique is more surface selective than the spin-echo with only the selenium in close spatial proximity to the HDA passivating layer being measured (~1-2 monolayers deep). Figure 4.3A-E presents CPMAS NMR spectra of 2 nm, 2.5 nm, 2.9 nm, 3.7 nm and 4 nm CdSe-HDA nanocrystals. A cross-polarization contact time of 15 ms was chosen from previous work on 2 nm CdSe-HDA which yielded optimal signal to noise by utilizing this parameter in the pulse sequence. The dashed vertical line and corresponding ^{77}Se spin-echo MAS NMR spectra of the particles (Figure 4.3A-E) and bulk hexagonal CdSe (Figure 4.3F) is shown in order to aid in interpretation of the chemical shift and peak comparisons.

Figure 4.3. ^{77}Se spin-echo MAS and CPMAS NMR spectra with a contact time of 15 ms, of (A) 2 nm (B) 2.5 nm (C) 2.9 nm (D) 3.7 nm and (E) 4 nm CdSe-HDA nanocrystals, demonstrating variations in core, surface, and near surface species with nanocrystal size. The CPMAS spectra consist of upfield surface sites and a downfield near surface site. ^{77}Se spin-echo NMR spectrum of bulk CdSe appears in (F). (Spinning speed, 14 kHz)



Interestingly, the CPMAS spectra for the 2.5 - 4 nm CdSe have a significant population of Se appearing upfield in relation to the spin-echo spectra. These surface/near selective experiments also appear to be composed of separate upfield/surface components and downfield/ core-like components from chemical shift and linewidth interpretations. From the previous work on 2 nm CdSe, the peak at -508 ppm (Figure 4.3A) is characterized as near surface Se with a suggested tetrahedral core-like structure and the upfield components as the most surface from the chemical shift and calculation of ^1H - ^{77}Se cross-relaxation time constants, T_{SeH} . In order to confirm that the downfield peaks in the CPMAS spectra of 2.5 - 4nm CdSe-HDA are near surface Se in agreement with the 2 nm particles, the cross-relaxation time constants, T_{SeH} , were calculated. An example of deconvolution of a CPMAS spectrum and CPMAS build-up curves for 2.9 nm CdSe-HDA are shown in Figures 4.4-4.5. These are used for T_{SeH} calculation (Table 4.2) which allows for distinguishing a depth determination of the Se sites. Figure 4 shows the 2.9 nm CPMAS spectra with a contact time of 20 ms, fit to 4 gaussians which were utilized with varying intensities for a series of cross-polarization contact times from 2-25 ms. These integrated ^{77}Se peak intensities from the fits were plotted as a function of the contact time, τ , and fit to equation 4.1¹⁶ using nonlinear least-squares analysis to determine T_{SeH} (Figure 4.5). The proton spin-lattice time constant, $T_{1\rho\text{H}}$, was determined following a procedure from a previous publication.¹⁷ As shown in Table 2, the upfield deconvoluted peaks at -574 ppm, -614 ppm, and -655 ppm (Figure 4.4), have similar T_{SeH} value of 4.8 (± 0.5) ms, 5.4 (± 0.5) ms and 4.1 (± 0.5) ms. The peak at

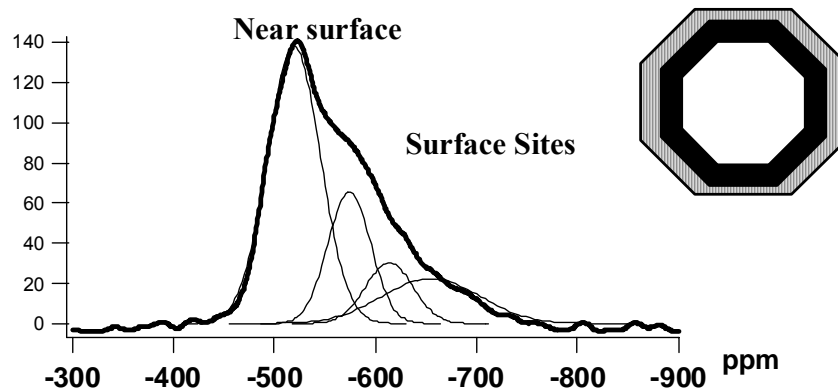


Figure 4.4. Example of a 2.9 nm ^{77}Se CPMAS spectrum fit to 4 gaussians. Measuring the CPMAS at various contact times in order to calculate the cross-relaxation time constants, T_{SeH} , confirms the most downfield component as near surface or selenium 1-2 monolayers from the surface. The black section of the NC image represents this area that is plotted in Figure 4.5-4.7 and correlates with the peak at -519 ppm. The peaks upfield of this peak correlate with the surface (striped) area of the NC image. (Contact time, 20 ms; Spinning speed, 14 kHz)

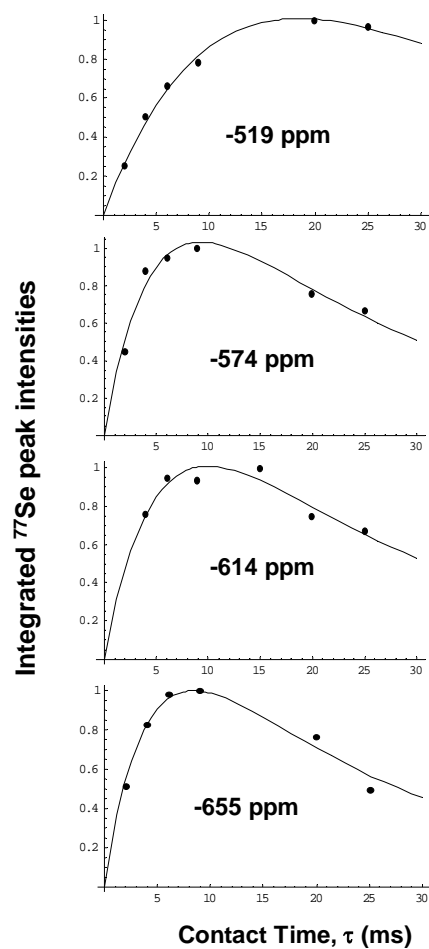


Figure 4.5. The integrated ^{77}Se peak intensities from ^1H - ^{77}Se CPMAS for 2.9 nm CdSe-HDA were plotted as a function of contact time, t . The plots were fit to equation 4.1 using a non linear least squares analysis to determine the cross-relaxation time constants, T_{SeH} .

Equation 4.1. $M(\tau) = M_0(\exp(-\tau/T_{1\rho H}) - \exp(-\tau/T_{\text{SeH}}))/(1 - T_{\text{SeH}}/T_{1\rho H})$

2.9 nm ^{77}Se CPMAS Peak (ppm)	T_{SeH} (ms) \pm 0.5 ms
-519	15.9
-574	4.8
-614	5.4
-655	4.1

Table 4.2. 2.9 nm CdSe-HDA ^1H - ^{77}Se cross-relaxation time constants, T_{SeH}

-519 ppm, however, differs substantially from the latter with a T_{SeH} value of 15.9 (± 0.5) ms. This difference can be attributed to stronger ^1H - ^{77}Se dipole-dipole couplings for the upfield sites and hence closer spatial proximity to the protons of the passivating layer than the site at -519 ppm in agreement with the previous study on 2 nm CdSe-HDA. Therefore, this analysis supports the upfield peaks in the CPMAS spectra (Figure 4.3A-E) as surface selenium and the downfield peaks in the CPMAS spectra as selenium near the surface (~ 1 -2 monolayers deep). This is also supported by the chemical shift of the near surface peaks being nearest the chemical shift of bulk hexagonal CdSe which suggests a tetrahedral symmetry surrounding these selenium consistent with the bulk material.

A summary of the chemical shift values and corresponding linewidths of this deconvoluted near surface peak as well as the center of gravity of the CPMAS spectra at (15 ms contact time) is given in Table 4.1. Interestingly, the chemical shifts of this peak increase with size from 508 ppm, -513 ppm, to -519 ppm (± 2 ppm) for 2 nm, 2.5 nm and 2.9 nm CdSe. After 2.9 nm, the chemical shift decreases to -511 ppm and -508 ppm (± 2 ppm) for 3.7 and 4 nm CdSe. This phenomenon is in analogy to the chemical shift increase followed by a subsequent decrease at 2.9 nm for the ^{77}Se spin-echo core component. Analysis of the linewidth of this site also follows the same trend with an increase with size from 25 ppm, 36 ppm, to 64 ppm for 2 nm, 2.5 nm and 2.9 nm CdSe. After 2.9 nm, the linewidth decreases to 47 ppm and 48 ppm for 3.7 and 4 nm CdSe. In agreement with the spin-echo results, these observations suggest a reconstruction in the surface and near surface sites of the material with a

maximum reconstruction event occurring near 2.9 nm which will be further investigated through nuclear shielding and band-gap exploration in the following section.

Also interesting in the CPMAS spectra is the population differences of surface sites with size. Although exact quantitative values for population comparisons between the various CdSe nanocrystals sizes from CPMAS is not possible due to possible differences in relaxation, mobility, and chain tilt which could effect the cross-polarization efficiency, a general qualitative description can be gained. Investigation of the population of upfield surface sites to the downfield near surface site in the CPMAS spectra (Figure 3A-E) indicate a general trend of a decreasing ratio with increasing size between these selenium species. As the particles increase in size, the ratio of the amount of surface selenium to selenium in a monolayer from the surface is expected⁴ to decrease and therefore this suggests that the population differences in these sites are reflected in the CPMAS spectra.

4.3.3. ⁷⁷Se Nuclear Shielding and Band-gap.

To further investigate this reconstruction phenomenon occurring at 2.9 nm as well as the change in the chemical shifts of the materials with size, there is a need for exploration into of the contributions to nuclear shielding of the Se nuclei. According to theory the chemical shift reflects the electronic environment of the nuclei and as a

general approximation, it is said that deshielding is associated with a decrease in electron density giving rise to a larger chemical shift value. In our system, the core component is downfield of the surface component (^{77}Se spin-echo and ^{77}Se CPMAS) and is therefore more deshielded or has less electron density than the surface component in the particles measured. The contribution to the observable nuclear shielding, σ_{obs} , is attributed to three terms as shown in Equation 4.2, where σ_{d} is the diamagnetic term dominant for nuclei with s -electrons (spherical electronic environment), σ_{p} is the paramagnetic term linked to non-spherical valence electrons, and σ' is associated with the contributions from atoms other than the one being measured.

$$\text{Equation 4.2. } \sigma_{\text{obs}} = \sigma_{\text{d}} + \sigma_{\text{p}} + \sigma'$$

For ^{77}Se , σ_{obs} is dominated by σ_{p} , which is associated with its four $4p$ -electrons, and according to the Ramsey equation (Equation 4.3), is related to three factors, where $\langle r^{-3} \rangle_{4p}$ is the inverse cube of the radius of the $4p$ -electrons, ΔE is the mean excitation energy, and ΣQ is the charge-density-bond order matrix.^{18,19}

$$\text{Equation 4.3. } \sigma_{\text{p}} \sim \langle r^{-3} \rangle_{4p} \cdot \Delta E^{-1} \cdot \Sigma Q$$

In analogy to the work here, Tomaselli¹⁰ and Thayer²⁰ *et. al* have demonstrated an an upfield chemical shift with decreasing particle size in InP and CdSe and correlated the respective ³¹P and ⁷⁷Se chemical shift with the average inverse lattice band gap energy. The overall ³¹P chemical shift data shows a fairly linear relationship while the overall ⁷⁷Se chemical shift demonstrates some curvature in the data extrapolating from the respective bulk compound. Due to the separation of surface and core components in the ⁷⁷Se spin-echo and the ability to investigate selenium in the near surface region with CPMAS, it was possible to examine the specific domains of the particle independently. Figure 4.6 shows the surface and core components from the spin-echo results (Table 4.1), and the near surface sites from CPMAS (Table 4.1) plotted versus the inverse band-gap energy of the material. The average inverse band-gap energy value in all plots was calculated by the absorption spectra of the corresponding size of particle.^{10,20} The straight lines for the core spin-echo plot and the near surface CPMAS plot are a linear regression, extrapolated from bulk CdSe and fit to the data points excluding the 2.5 nm and 2 nm values. The straight line for the surface component of the spin-echo is a linear regression extrapolated from bulk CdSe and fit to the all the sizes but the 2 nm. For the 2 nm, both the center of gravity and the deconvoluted peak at -568 ppm are included as surface components due to their closeness to the linear fit and the lack of a definite surface/core separation from the small size of the particle. The sizes left out of the linear regressions were done so because of the large deviance from the linear fit. The spin-echo core plot and near surface CPMAS plot both are linear to 2.9 and then

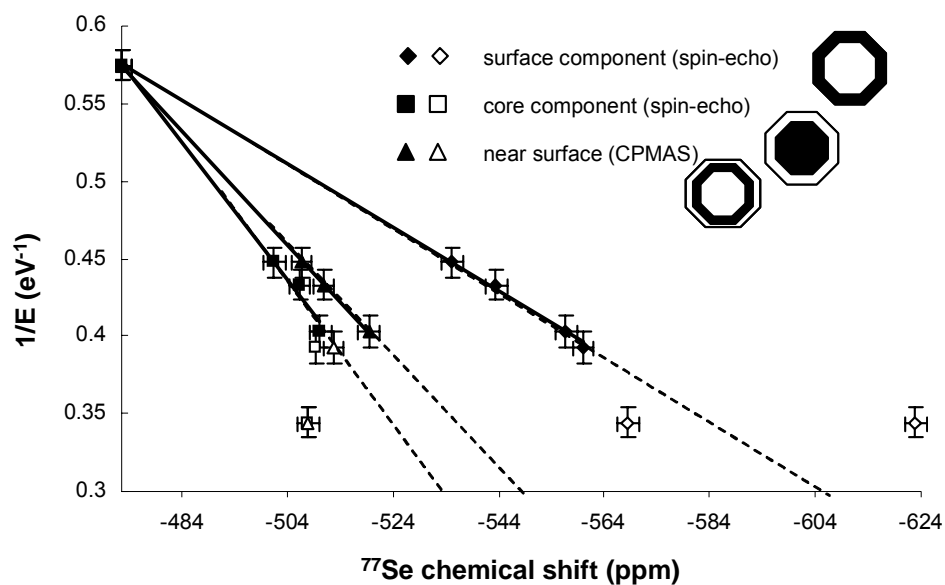


Figure 4.6. Plot of the ^{77}Se chemical shift from the surface and core components (spin-echo) and from Se near surface (CPMAS, 15 ms contact time) for 2 nm, 2.5 nm, 2.9 nm, 3.7 nm, 4 nm and bulk CdSe versus the inverse band-gap energy. The straight lines for the core component and near surface data is a linear regression, extrapolated from bulk CdSe, and fit to the data points of 4nm, 3.7 nm, and 2.9 nm particles. The dashed lines are extrapolated from the linear regression. The black area of the inset of the NC indicates the area plotted. The straight line for the surface component is a linear regression, extrapolated from bulk CdSe, and fit to the data points of 4 nm, 3.7 nm, 2.9 nm, and 2.5 nm CdSe.

deviate from the linear plot with chemical shifts downfield of the regression suggesting an electronic similarity between the core and near surface plot. The observation could be expected considering that the sites likely share similar environments with selenium tetrahedrally coordinated to cadmium and that the CPMAS near surface sites likely contribute to the core component signal in the spin-echo from the closeness of the chemical shift values. The surface component has a different behavior with only the 2 nm deviation from the linear regression. The nature of the deviation is difficult to assign with the -568 ppm peak appearing downfield and the -623 ppm center of gravity peak appearing upfield of the regression.

With respect to the Ramsey equation (Equation 4.3), linearity of the ^{77}Se chemical shift values with inverse band-gap implies constant or similar values for $\langle r^{-3} \rangle_{4p}$ and ΣQ . Therefore, the large deviation from linearity after 2.9 nm for Se tetrahedrally coordinated to Cd in the core and near surface sites suggests a dominating change in at least one of these factors with nanocrystal size. As indicated by H. Duddeck, only in rare cases is it possible to interpret any of the three factors from the Ramsey equation separately as a change in one will likely affect the other.¹⁹ And, in particular, $\langle r^{-3} \rangle_{4p}$ and ΣQ are closely connected suggesting the downfield chemical shift deviation indicating a lesser amount of electron density around these selenium are related to one or both of these factors. In physical terms, this observation could likely be connected to a change in the ionicity as the likely

reconstruction event of the CdSe lattice in sizes below 2.9 nm with the cadmium atoms tetrahedrally coordinated to the selenium atoms in these sites having a greater electronegativity than in the larger sizes and therefore pulling electron density from the selenium atoms being measured. In agreement with our data, this deshielding trend of attached atoms and electronegativity has been observed in ^{77}Se NMR.¹¹ With this argument, the surface sites do not behave the same with little or no change in $\langle r^{-3} \rangle_{4p}$ and ΣQ until smaller than 2.5 nm from the linearity of the inverse bandgap plot with nanoparticle size. This seems very likely considering the differing nature of the surface selenium which can have dangling bonds and be bound to surface cadmium with bound organic passivating ligands. The effect of ligands donating electron density to the surface cadmium atoms could possibly dominate the chemical shift of the attached selenium over a change in ionicity of the lattice more likely felt within the particle which could maintain the linearity of the plot of chemical versus inverse bandgap to smaller sizes.

In order to better view the change in electron density of the discrete selenium sites with size of the CdSe particles, the number of Cd and Se atoms of the material was plotted versus the ^{77}Se chemical shift (Figure 4.7). The precursor, $\text{Li}_4[\text{Cd}_{10}\text{Se}_4(\text{SC}_6\text{H}_5)_{16}]$, is also shown in the plot. The surface sites are the most upfield and show a trend of increasing upfield shift with decreasing size indicating an increasing electron density on these selenium species as the particles get smaller. The near surface selenium are more deshielded than the surface sites, followed by the

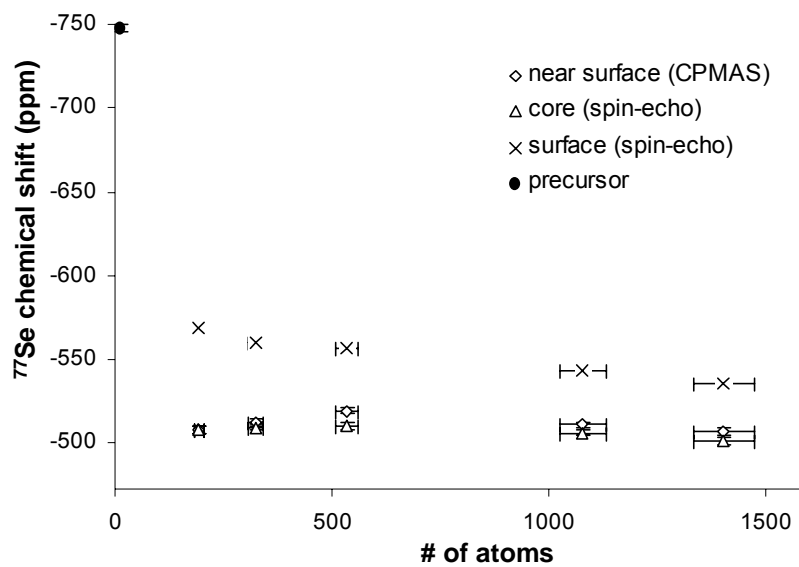


Figure 4.7. Plot of the number of Cd and Se in the material versus the ^{77}Se chemical shift values from the surface and core components (spin-echo) and from Se near surface (CPMAS, 15 ms contact time) for 2 nm, 2.5 nm, 2.9 nm, 3.7 nm, 4 nm and the NC precursor, $\text{Li}_4[\text{Cd}_{10}\text{Se}_4(\text{SC}_6\text{H}_5)_{16}]$.

internal selenium, which are the most deshielded. This is clearly demonstrated in Figure 4.7 by the decreasing height of the data points in these sites, signifying a decrease in electron density of the corresponding selenium atoms as you move within the particle. This plot also nicely demonstrates the similarity of the electron density surrounding selenium in near surface and core selenium with size as both plots have chemical shifts that increase upfield (chemical shift values become more negative) with a nearly linear trend with decreasing size to 2.9 nm. After 2.9 nm both plots, increase in a downfield direction (chemical shift values become less negative) also close to linear with decreasing size from 2.9 nm.

In order to analyze the overall ^{77}Se chemical shift of the entire particle and the entire surface region, neglecting structural variations within these areas, the center of gravity of the spin-echo spectra was plotted versus inverse bandgap and number of atoms. A plot of the ^{77}Se center of gravity from the spin-echo spectra and CPMAS for the CdSe nanocrystals and bulk CdSe versus the inverse band-gap energy is shown in Figure 4.8. The straight line for the spin-echo is a linear regression fit to the data points, extrapolated from bulk CdSe, excluding the 2 nm point. The straight line for the CPMAS is a linear regression fit to all the center of gravity data points. The dashed lines are extrapolations of the linear regressions.

The spin-echo center of gravity plot (total particle) fits well to a linear regression for all the data but the 2 nm center of gravity. This is in contrast to the deviation of the linear regression fit from the deconvoluted spin-echo spectra (Figure 4.6) which occurs in sizes < 2.9 nm. As you reduce the size of the particle, the

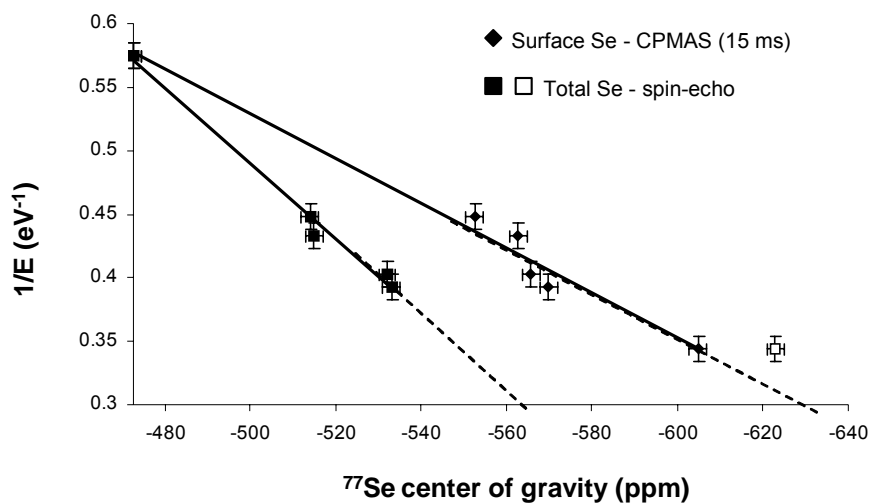


Figure 4.8. Plot of the ^{77}Se center of gravity from the spin-echo spectra and CPMAS for 2 nm, 2.5 nm, 2.9 nm, 3.7 nm, 4 nm and bulk CdSe versus the inverse band-gap energy. The straight line for the spin-echo is a linear regression, extrapolated from bulk CdSe, and fit to the data points excluding the 2 nm point. The straight line for the CPMAS is a linear regression fit to all the data points. The dashed lines are extrapolations of the linear regressions.

surface to core ratio gets much larger and therefore the surface components at small sizes contribute greatly to the center of gravity indicating a significance of the surface to the linearity of (Figure 4.8) overall ^{77}Se chemical shift with inverse bandgap. This linearity also suggests that the overall particle chemical shift has more constant average values for $\langle r^{-3} \rangle_{4p}$ and ΣQ while considering the ^{77}Se shielding for the entire particle. The 2 nm particle deviates greatly from the linear regression likely due to this size having such a large surface to volume ratio; the chemical shift fits more near to the surface center of gravity plot as could be expected for such a size. The CPMAS (15 ms contact time) center of gravity plot representing the overall surface/near surface sites (Figure 4.8) fits well to a linear regression for all the data points. This is similar to the deconvoluted spin-echo spectra for surface sites (Figure 6) which fits well to a linear regression excluding the 2 nm particle. This suggests, as discussed above, a constant or nearly constant average values for $\langle r^{-3} \rangle_{4p}$ and ΣQ in these sites.

The number of Cd and Se atoms of the material was plotted versus the ^{77}Se center of gravity chemical shift (Figure 4.9) to more easily view the change in overall electron density in the whole particle and the overall surface/near surface sites with size of the CdSe particles. The precursor, $\text{Li}_4[\text{Cd}_{10}\text{Se}_4(\text{SC}_6\text{H}_5)_{16}]$, is also shown in the plot. The center of gravity from the CPMAS (surface/near surface sites) are the most upfield and show a trend similar to the surface sites from the deconvoluted spin-echo with increasing electron density on these selenium species as the particles get smaller.

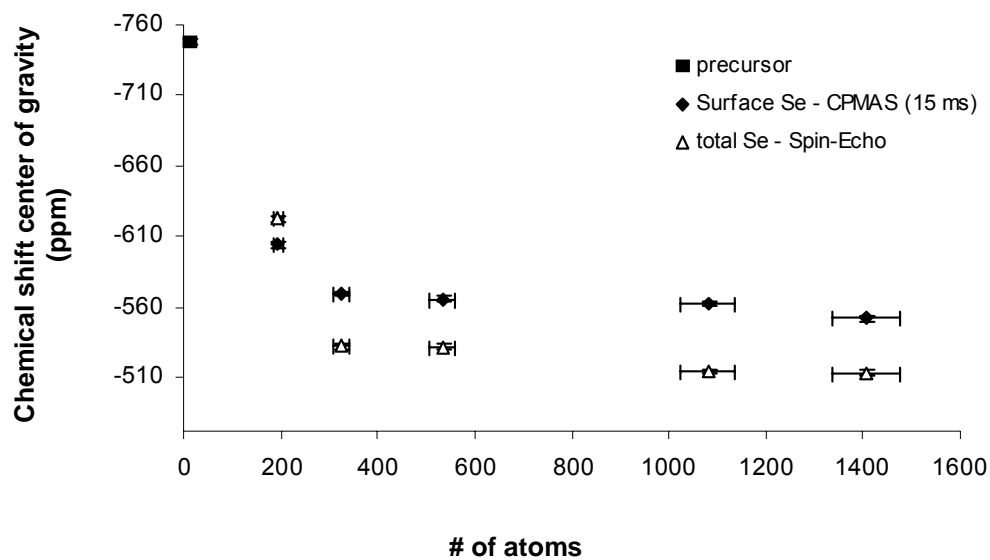


Figure 4.9. Plot of the number of Cd and Se atoms in the material versus the ^{77}Se chemical shift values for the center of gravity from spin-echo and CPMAS(15 ms contact time) for 2 nm, 2.5 nm, 2.9 nm, 3.7 nm, 4 nm and the NC precursor, $\text{Li}_4[\text{Cd}_{10}\text{Se}_4(\text{SC}_6\text{H}_5)_{16}]$.

The center of gravity chemical shifts from the spin-echo spectra, representing the overall chemical shift of the particles, exhibit more deshielding than the overall surface sites (CPMAS center of gravity), demonstrated by the decreased height of these data points, excluding the 2 nm point in Figure 4.9. The 2 nm point is slightly more upfield for the center of gravity spin-echo than the CPMAS which is likely due to the extremely large surface to core ratio and also is difficult to analyze from the large amount of noise in the spin-echo spectrum. Interestingly, the spin-echo center of gravity plot demonstrates a trend similar to the surface sites with increasing electron density on these selenium species as the particles get smaller. This is in contrast to selective examination of the near surface and core selenium with size (Figure 4.7) which increase in chemical shift to 2.9 nm and then decrease. This demonstrates the change in ^{77}Se chemical shift from selective site measurements to examining the particle as a whole entity.

4.4. Conclusions.

^{77}Se spin-echo and CPMAS NMR measurements provide vital knowledge of distinct surface, near surface and core regions of CdSe-HDA nanocrystals giving direct insight into particle reconstruction with size. At 2.9 nm, CdSe-HDA shows the largest degree of reconstruction, as well as the core and near surface surface selenium sites reaching a maximum shielding and change in trend of the plot of ^{77}Se chemical shift versus inverse bandgap energy. These observations suggest a special reconstruction within the particle at this size. With examination of the Ramsey

equation, this could likely be related to a change in ionicity of the particle lattice. The surface selenium sites behave differently than the core, with increasing shielding with decreasing size and following a nearly linear relationship with inverse bandgap energy.

4.5. References.

1. Talabin, D.V.; Rogach, A.L.; Mekis, I.; Haubold, S.; Kornowski, A.; Haase, M. Weller, H. *Colloids and Surfaces*, **2002**, *202*, 145-154.
2. Jang, E.; Jun S.; Chung, Y.; Pu, L. *J. Phys. Chem. B*. **2004**, *108*, 4597-4600.
3. Fu, H.; Zunger, A. *Phys. Rev. B*. **1997**, *56*, 1496-1508.
4. Blackburn, J.L; Ellingson, R.; Micic, O; Nozik, A. *J. Phys. Chem. B*. **2003**, *107*, 102-109.
5. Li,R; Lee, J.; Yang B.; Horspool, D.; Papadimitrakopoulos, F. *J. Am. Chem. Soc.* **2005**, *127*, 2524-2532.
6. Berrettini, M.G.; Braun, G.; Hu, J.G.; Strouse, G.F. *J. Am. Chem. Soc.* **2004**, *126* (22), 7063 -7070.

7. Ladizhansky, V.; Hodes, G.; Vega, S. *J. Phys. Chem. B* **1998**, *102*, 8505-8509.
8. Elbaum, R.; Vega, S.; Hodes, G. *Chem. Mater.* **2001**, *13*, 2272-2280.
9. Mayeri, D.; Phillips, B.L.; Augustine, M.; Kauzlarich, S.M. *Chem. Mater.* **2001**, *13*, 765-770.
10. Tomaselli, M; Yarger, J.L.; Bruchez, M.; Havlin, R.H.; deGraw D.; Pines, A.; Alivisatos, A.P. *J. Chem. Phys.* **1999**, *110*, 8861-8864.
11. Becerra, L. R.; Murray, C. B. et al. *J. Chem. Phys.* **1994**, *100*, 3297.
12. Cumberland, S. L.; Hanif, K. A.; Khitrov, G. A.; Javier, A.; Strouse, G. F.; Woessner, S. M.; Yun, C. S. *Chem. Mater.* **2002**, *14*, 1576-1584.
13. Dance, I. G.; Choy, A.; Scudder, M. L. *J. Am. Chem. Soc.* **1984**, *106* (21), 6285.3.
14. The ratio of surface to core atoms, defined as the ratio of atoms with dangling bonds to those with 4-fold coordination, was determined from analyzing several near-spherical, faceted CdSe wurtzite crystals created in Crystal Impact's Diamond

software, with singly bound atoms removed. C_{3v} point group symmetry and the lattice parameters $a = 4.3\text{\AA}$, $c = 7.0\text{\AA}$ were used for this estimate.

15. Raola, O.; Strouse, G.F. *Nano Lett.*, **2002**, 2, 1443-1447.

16. Mehring, M. *High-Resolution NMR Spectroscopy in Solids*; Springer-Verlag: New York, 1976.

17. Voelkel, R. *Angew. Chem., Int. Ed. Engl.* **1988**, 27, 1468-1483.

18. Ramsey, N.F. *Phys. Rev.*, **1950**, 78, 699.

19. Duddeck, H. *Prog. Nucl. Magn. Reson. Spectrosc.* **1995**, 27, 1-323.

20. Thayer, A.; Stiegerwald, M.; Duncan, T.; Douglass, D. *Phys. Rev. Lett.* **1988**, 60, 2673-2676.

Chapter 5. Oxidation Depth Profiling in InGaP Nanocrystals.

5.1. Introduction.

The decreased industrial concern for the toxicity^{1,2} associated with III-V systems compared to Se and Te based II-VI materials has led to an interest in developing the chemistry of III-V semiconductor nanocrystals (InP, GaP, InN, GaN) and their ternary analogs (i.e InGaP, InAlP, etc).³⁻¹¹ The surfaces of nanocrystals including ligand effects, oxidation, and atomic vacancies are prominent features in controlling the physical properties of the nanocrystal, including the photoluminescence and stability.^{6-7,12-17} In CdSe, extensive investigation of the surfaces and the influence of the passivant ligand have led to a model which invoke surface reconstruction events as a critical manipulator of the physical properties of these systems (Chapters 2-4).¹⁷⁻²³ Recent efforts in the literature have probed the nature of these processes using X-ray Absorption (XAS) and neutron techniques,²³⁻²⁷ X-ray photoelectron spectroscopy (XPS),^{6,7,15,28-29} transmission electron microscopy (TEM),^{30,31} and solid-state NMR^{8,17,32-35} in order to develop an atomistic picture of the nanocrystal surface, near-surface, and core atoms. The lack of knowledge about the nature of the surface reconstruction, vacancies, and oxidation process in nanoscale materials leads to an inability currently to systematically design desired physical properties into these materials, such as commonly carried out for molecular beam epitaxial grown quantum well structures.

The influence of surface states in InP materials has been investigated in both bulk and nanoscale materials.^{6-11,36-43} In bulk InP wafers, chemical or thermal treatment of the materials leads to surface oxidation and reconstruction.³⁶⁻⁴² In nanocrystalline InP, it has been suggested that the photoluminescence (PL) quantum efficiency can be enhanced by wet-chemical etching of the nanoparticle surfaces.^{5,7,10-11} Alivisatos *et al.*⁶ suggested that a thin oxide layer in lyothermally prepared InP nanomaterials may be important for observation of PL. Weller *et al.*⁷ carried out photoelectron spectroscopy (PES) with synchrotron radiation on trioctylphosphine oxide (TOPO) passivated InP and concluded that an oxide layer is present both prior to and after etching, attributing the enhanced PL following etching to a reduction of phosphorus dangling bonds (vacancies) and improved surface passivation. These results clearly identify changes in the surface states following HF etching, but do not address the nature of the surface oxide or reconstruction events following chemical treatment. It is well-established that hydrogen fluoride (HF) wet-chemical etching of bulk InP wafers results in a self-terminating oxide layer of ~ 2 nm⁴² with the formation of In₂O₃, InPO₄, and InPO₃ at the air-surface interface following exposure to air.³⁶⁻⁴² Inspection of the work on nanocrystalline InP suggests that the oxidation depth is below the native oxide thickness of bulk materials which could potentially be due to strain at the interfacial layer. Assessing the chemical nature of the oxide and the changes in the nanomaterial surface are critical to drawing conclusions about the PL enhancement observed following chemical treatment of the InP surface. Unfortunately, this is a difficult process to achieve using traditional analytical

methods due to the low number of atoms in the nanomaterial and the high surface to volume ratio for these systems. While previous experimental studies have indicated oxidation of the surface of InP nanoparticles occur, a thorough investigation of the types, growth, depth, and connectivity of the oxide species has not been conducted.

In this chapter, a study on the nature of the oxidation layer in lyothermally grown InGaP nanocrystals before and after HF etching using ^{31}P solid-state NMR is reported. Solid-state NMR is a powerful technique for elucidating complex surface information such as ligand-crystal bonding arrangements, reconstruction, and structural variations.^{8,17,32-35,43-45} ^{31}P 1D and 2D solid-state NMR measurements reveal the similarity of the nature of oxidation on HF etched and unetched InGaP nanocrystals, including the species of oxidized phosphorus, depth of oxidation and spatial proximities. The similarities in the surfaces following etching suggest that a surface reconstruction event with changes in the nature of the vacancies and bonding at the surface is triggered by the HF treatment step and may be responsible for the enhanced PL, with the oxide layer acting as a high band-gap shell rather than a trap center for PL.

5.2. Experimental Section.

5.2.1. Synthesis of InGaP Nanocrystals (unetched).

InGaP nanocrystals (unetched) were prepared as described previously.³⁻⁵ Briefly, 0.3826 g (1.31 mmol) indium (III) acetate, and 0.0481 g (0.131 mmol)

gallium (III) acetylacetonate, were degassed at 120°C in 45.5 g n-hexadecylamine (HDA) for approximately 30 minutes. $\text{P}(\text{Si}(\text{CH}_3)_3)_3$ (0.63 M, 2.17 mmol) was injected via syringe at 120 °C under Ar, and the temperature was ramped to 280 °C over ~7 hrs. The reaction was run ~8 hrs while the size and dispersity was monitored by UV-vis absorbance spectroscopy. The reaction was quenched by cooling to 60 °C, followed by collection via the addition of approximately 100 mL of dry methanol and centrifugation. Purification was accomplished by dissolution in a minimum amount of dry toluene, re-precipitation by addition of dry methanol, and centrifugation under Ar (3×) and dried under a flow of argon overnight. The unetched HDA passivated InGaP particles were spherical, Zn blende 4.5 nm particles and did not exhibit a detectable PL ($\Phi_{\text{EM}} < 0.01$) The absorbance spectrum and TEM image are shown in Figures 5.1 and 5.2, respectively. Transmission electron microscopy (TEM) measurements were conducted on a JEOL 2010 microscope operating in bright field mode.

5.2.2. Etching of InGaP Nanocrystals.

Etched InGaP nanocrystals were prepared by dissolving 10 mg of the un-dried nanocrystals from the above reaction in ~35 mL of toluene under ambient conditions. The dilute conditions are necessary to ensure a more uniform etching of the particles under lower power excitation. To maintain solubility during etching, hexadecanoic acid (~200 mg) was added and the mixture was sonicated to produce an optically

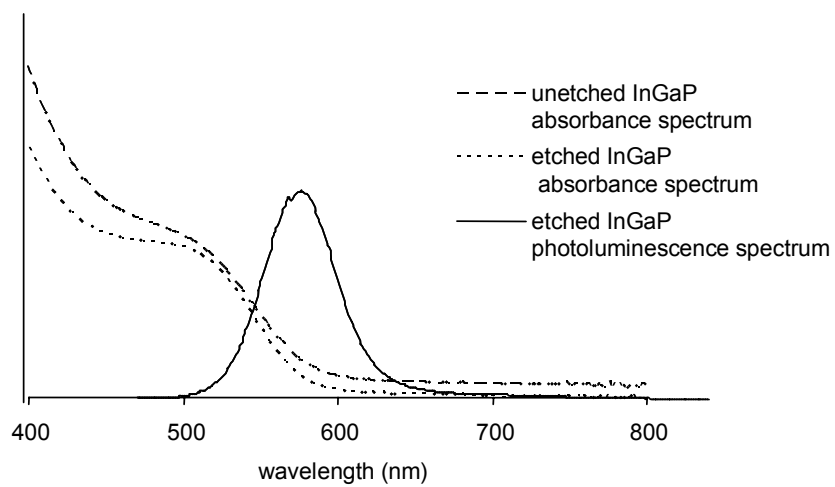


Figure 5.1. Absorbance spectra of unetched and HF etched InGaP nanocrystals. Emission spectrum of etched InGaP nanocrystals ($\lambda_{\text{ex}} = 420$ nm). The unetched particles do not emit.

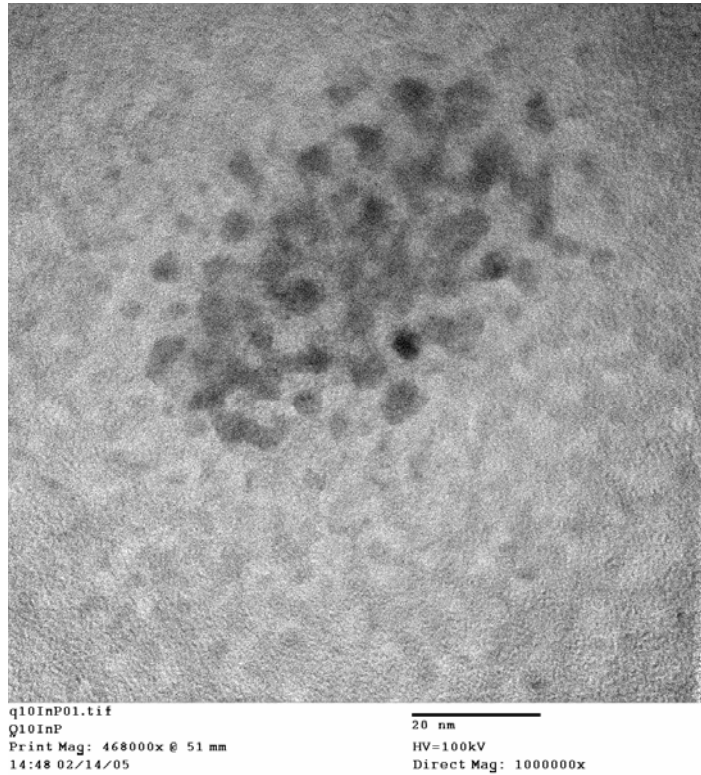


Figure 5.2. TEM image of unetched 4.5 nm InGaP nanocrystals. The poor quality of the TEM image is due to a propensity for beam damage and sample aggregation.

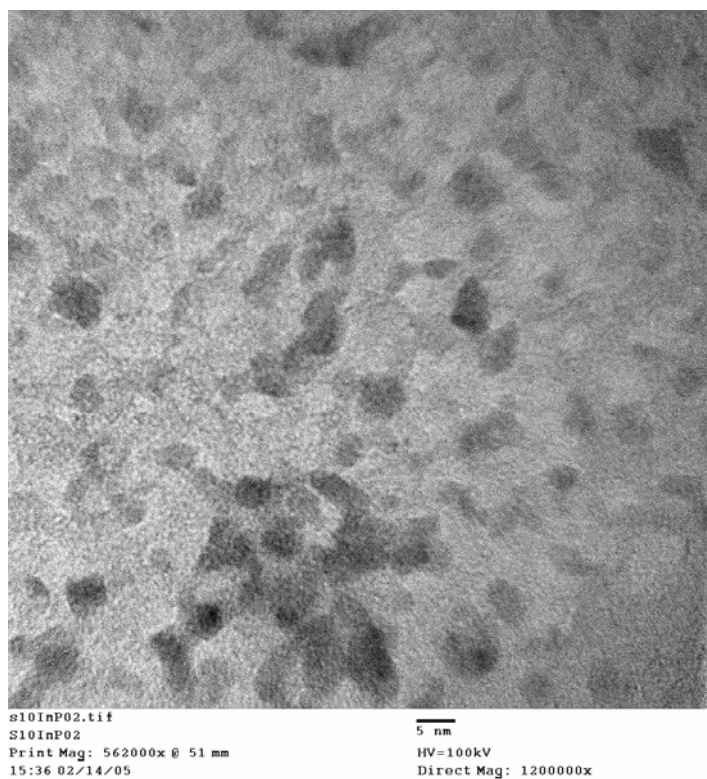


Figure 5.3. TEM image of etched 4.5 nm InGaP nanocrystals. The poor quality of the TEM image is due to a propensity for beam damage and sample aggregation.

clear solution. Etching was carried out in an aerated solution by the addition of ~30 μL of a 5% HF solution in MeOH and excitation using a low-power Hg lamp at 365 nm for ~3 minutes, followed by precipitation with methanol and centrifugation. The isolated nanomaterials were purified by dissolution in a minimum amount of toluene, re-precipitated by addition of methanol, centrifuged ($3\times$), and the solid precipitate dried overnight under Ar. The InGaP nanoparticles are spherical Zn blende nanoparticles with a size of 4.5 nm. A TEM image of the etched particles is shown in Figure 5.3. The samples emit after etching with a PL quantum yield of 8% (in dry degassed toluene) when excited at 420 nm. The absorbance and emission spectra are shown in Figure 5.1.

5.2.3. NMR.

Solid state NMR experiments were carried in a 4mm packed MAS rotor containing ~75 mg of materials. Solid-state ^{31}P MAS NMR experiments were performed at room temperature on a Bruker 300 MHz Avance spectrometer with a 4-mm broadband MAS probe tuned to 121.5 MHz, 300 MHz, and 282.3 MHz for ^{31}P , ^1H , and ^{19}F respectively. A spinning speed of 12 kHz was used in all experiments and the chemical shifts of ^{31}P , ^1H , and ^{19}F were referenced to 85% H_3PO_4 , TMS, and CFCl_3 , respectively.

The ^{31}P single pulse MAS experiments were performed with an acquisition time of 2.1 ms, a recycling delay of 30 s, and a 90° pulse of 2.75 μs . The ^1H - ^{31}P

CPMAS experiments were acquired using TPPM ^1H decoupling, ramped cross-polarization (CP), an acquisition time of 2.1 ms, a recycle delay of 3 s, contact time ranging from 0.1 to 20 ms, and a ^1H 90° pulse length of 5.25 μs .

The 2D $^{31}\text{P}\{^1\text{H}\}$ heteronuclear correlation (HETCOR) experiments were performed with a frequency-switched Lee-Goldberg (FSLG)⁴⁶ irradiation of 85 kHz applied to the ^1H spins during the t_1 evolution period, ramp CP during mixing, a TPPM ^1H decoupling during the data acquisition of 2.1 ms, a recycling delay of 1 s, and a ^1H 90° pulse length of 3 μs .

The 2D $^{31}\text{P}\{-^{31}\text{P}\}$ double quantum (DQ) MAS NMR experiments were acquired using a rotor-synchronized BABA pulse sequence⁴⁷ with an excitation time of 1.66 ms to reintroduce dipole-dipole couplings. The $\pi/2$ radio frequency (rf) pulses were set to a length of 4 μs . TPPM decoupling was applied during the acquisition and the dipole-dipole recoupling periods and States-TPPI was used in t_1 for phase sensitive detection. Long T_1 relaxation times were circumvented by cross polarization of ^1H magnetization to nearby ^{31}P surface sites so that a recycle delay of 1 s was sufficient. The ^1H radio frequency field of the CP was ramped between 80 and 100% of its maximum value.

The ^{19}F single pulse MAS experiment was performed with an acquisition time of 7.3 ms, a recycling delay of 4 s, a 90° pulse of 6 μs and required 160 scans for adequate signal to noise due to the small amount of fluorine present.

5.3. Results and Discussion.

5.3.1. Total Phosphorous Site Identification (^{31}P MAS NMR).

^{31}P MAS single-pulse NMR spectra, which measure all of the ^{31}P in the material, of unetched and etched InGaP nanocrystals are shown in Figure 5.3A and 5.3B, respectively. ^{31}P NMR peaks at 24, 1, -9 (shoulder), and -210 ppm are present in both spectra. The shoulder at -9 ppm is more clearly observable in the inset in Figure 5.3. The peaks were fit by a linear least squares analysis utilizing the Bruker software package assuming Gaussian lineshapes.

Based upon the chemical shift and line width, the ^{31}P peak at -210 ppm is assignable to a ^{31}P occupying a tetrahedral lattice site ($T_d - \text{P}$ site) bound to either In or Ga in the Zn blende lattice of the InGaP nanoparticle. The chemical shift of ^{31}P in bulk InP and GaP appears at -147⁴⁸ and -142⁴⁹ ppm. The chemical shift for the tetrahedral ^{31}P site in the nanocrystal appears upfield from bulk due to a domination of the paramagnetic contribution (σ_p) to the chemical shielding parameters in the material. The shift in the NMR resonance exhibits an inverse relationship to the band-gap energy of the nanoparticle, and therefore the observed shift can be correlated with the size of the nanoparticle.^{8,50} The breadth of the -210 ppm $T_d\text{-P}$ site (linewidth $\delta_{1/2} = 60$ ppm) is

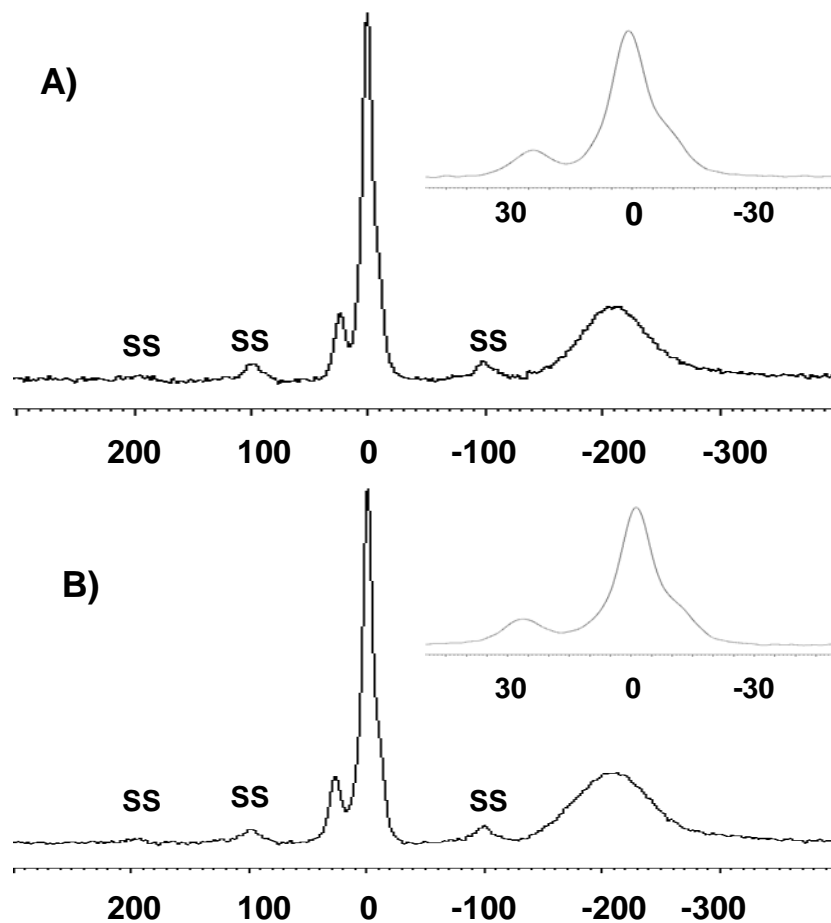


Figure 5.4. Solid-state ^{31}P single-pulse spectra recorded under MAS at 12kHz, indicating 3 distinct phosphorus sites at 24, 1 and -210 ppm with a shoulder at -9ppm. (A) unetched and (B) HF etched InGaP nanocrystals. (Spinning sidebands are marked with ss.) The shoulder at -9 ppm is more clearly observable in the inset in both spectra.

likely due to chemical shift distribution, as well as the indirect exchange interaction with the quadrupolar indium ($S=9/2$) and/or gallium ($S=3/2$) nuclei in close proximity to the tetrahedral P lattice site. Broadening of the $S=1/2$ ^{31}P nuclei due to exchange interactions have been reported in bulk InP⁴⁸ and in InP nanocrystals.⁸ Significant contributions to the broadening from chemical shift anisotropy is excluded due to the observation that decreasing the spinning speed from 12 kHz to 5 kHz does not give rise to spinning sidebands which suggests an even distribution of electron density around the internal phosphorus atoms, as expected for the tetrahedral environment in a Zn blende lattice site.

The observation of three downfield ^{31}P resonances at 24 ppm, 1 ppm, and -9 ppm are assignable to oxidized phosphorus sites based upon interpretation of the chemical shifts, intensity growth in time with exposure to air, and literature supporting the presence of a relatively thick native oxide in bulk,³⁶⁻⁴² nanocrystalline,⁶⁻⁸ and micron sized InP.⁴³ The formation of an oxide is further supported by the observation of spinning side bands on the ^{31}P resonances due to the asymmetrical electron density about the phosphorus site, as expected due to breaking of the T_d symmetry of the P site in the Zn blende lattice following oxidation (Figure 5.4). This assumption is supported by the observation of a changing numbers of spinning side bands that are dependent on the spinning frequency indicative of the symmetry breaking about these P centers, which was not observed in the T_d site P at -210 ppm. This is independent of the etching treatment.

To analyze the differences in the oxide population for unetched and etched InGaP samples, the samples ^{31}P spectra were measured immediately after isolation and exhibit a relative population of oxidized phosphorus to T_d -site phosphorus of 1:1.15 and 1:1.11, respectively. To allow a quantitative analysis of the P sites, full T_1 relaxation of the P sites was acquired by using a relaxation delay of 30 s. The oxidized phosphorous population was the combined values of integration of the 3 phosphorus sites (and corresponding spinning sidebands) at 24, 1, and -9 ppm and the T_d -site P peak integration corresponds to the integrated peak value of the peak at -210 ppm. In view of the fact that integration values from ^{31}P MAS NMR experiments give an accurate measurement of the relative population of the oxidized phosphorus sites to the T_d -site phosphorus, this technique was used to monitor the time-dependent changes in the population of these sites. After approximately one month, the unetched and etched integration of oxidized phosphorus phosphorus changed to 1: 0.88 and 1: 0.96, respectively. Approximately 2 weeks after this, the integration of oxidized to internal phosphorus was 1: 0.79 and 1: 0.82 for the unetched and etched samples, respectively. No changes in peak position for the four sites were observed over the time period; only the integrated area showed a change for the oxidized to unoxidized sites. This suggests that the oxide thickness approaches a limiting value in the nanoparticle corresponding to \sim 1-2 monolayers using a simple calculation of surface to core atoms based upon an InP unit cell.¹⁷

The oxidation ratios represent qualitative arguments. To accurately assess the results of the time-dependent oxidation analysis, sample handling must be taken into

consideration. In these experiments, the samples were not exposed continuously to air, so oxidation is a slow process. For the initial ^{31}P MAS experiment, the materials were taken directly from drying, ground to a fine powder (for stable MAS spinning) in air, packed in a rotor and measured. For the next measurement a month later, the samples had been stored under argon but air was present due to sample preparation for the measurements. The lack of controlled O_2 concentration does not allow the kinetics of the process to be analyzed. However, it is worth noting that the experiments were also repeated on various samples, and in all cases, significant oxidation growth was observed and the rate of oxidation was dependent on sample handling.

The observation of a higher amount of oxidized phosphorous sites following wet-chemical etching in air and the time-dependent increase in oxidized P sites is expected if the oxidation is occurring primarily at the surface of the nanoparticle, since oxidation should proceed as a diffusional process into the core on the InGaP surface. However, the nature of the oxidation process on a nanomaterial must be different than bulk, since the native oxide is $\sim 2\text{nm}$ or nearly equivalent to the nanoparticle radius, which would predict complete particle oxidation and loss of the optical properties with time. The lack of a significant change in size in the TEM spectra (Figures 5.2 and 5.3) or the absorbance spectra (Figure 5.1) for the InP nanocrystals suggest that the oxide layer must lie within only the top few monolayers. This is further shown by the insignificant shifts in the NMR for the -210 ppm peak whose position is dependent on the nanocrystal size. This suggests the assignment of

the T_dP sites to the core of the nanoparticle and the oxidized P sites to the outermost atoms of the nanocrystals. The lack of native oxidation thickness in the nanocrystal compared to bulk may be due to strain in the surface or differences in the nature of the oxide at the surface(ie. In₂O₃ vs InPO_x).³⁶⁻⁴² To establish the assignment of the phosphorus sites, HETCOR NMR experiments were performed.

5.3.2. Surface ³¹P Oxidation Identification by 2D ³¹P{¹H} HETCOR NMR.

Given that the ³¹P MAS single-pulse NMR experiments strongly suggest oxidation arises at the surface of the InGaP nanocrystal based upon the observed chemical shifts, CSA, and integrated peak intensities in time; the use of 2D ³¹P{¹H} frequency-switched-Lee-Goldberg (FSLG) HETCOR NMR (Figure 5.5) was used to further confirm the identity of the ³¹P NMR peaks at 24, 1, -9, and -210 ppm. 2D ³¹P{¹H} FSLG HETCOR NMR uses cross polarization (CP) to probe the proximities of ¹H nuclei on the passivant shell to the ³¹P nuclei in the InP nanocrystals. HETCOR measurements allow a depth profile of the material due to the distance dependence of the cross-polarization employed in the pulse sequence. The longer a cross polarization time, the weaker the dipole-dipole couplings that can be measured and, hence, the further the distance between two nuclei that can be detected. This allows ³¹P surface sites which are in close proximity to the protons of the passivating HDA ligands to be discreetly identified.

The ³¹P{¹H} FSLG HETCOR NMR spectra of unetched InGaP, with a 2 ms contact time of cross-polarization, is shown in Figure 5.5, with separately measured

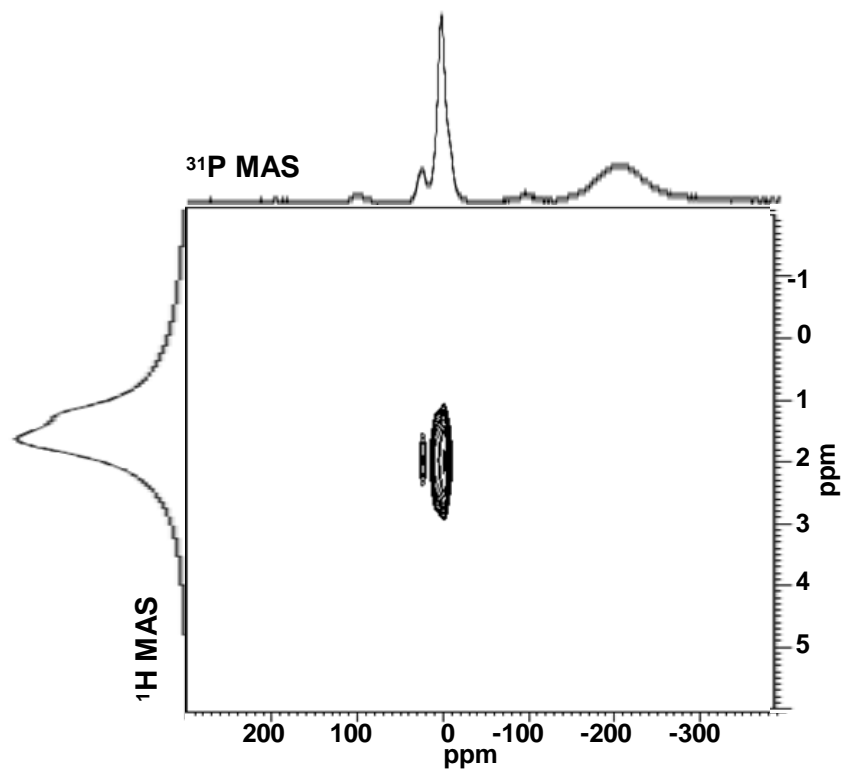


Figure 5.5. $^{31}\text{P}\{^1\text{H}\}$ FSLG HETCOR spectrum of unetched InGaP nanocrystals recorded under MAS at 12kHz with a cp contact time of 2ms. Separate single pulse ^{31}P MAS and ^1H MAS spectra reside along the horizontal and vertical axis, respectively. The observed strong correlations of the ^{31}P peaks at 24 and 1 ppm with the HDA protons confirm an oxidized surface in the nanocrystals by establishing a close spatial proximity of the passivating layer with oxidized phosphorus sites.

single pulse MAS ^{31}P and ^1H spectra on the horizontal and vertical axis, respectively, to aid in interpretation of the data. Because the HETCOR spectra are nearly identical between unetched and etched InGaP, only the HETCOR data for the unetched InP is presented. The ^1H NMR peaks between ~ 0 and 3 ppm on the vertical axis in Figure 5.5 corresponds to the protons on the HDA passivating layer. HDA was confirmed as the passivating layer through examination of ^{13}C MAS NMR which indicates the ^{13}C resonances of HDA as well as broadened α , β , and γ carbons consistent with decreased rotation and chemical shift distribution from binding to the surface of the particle (Figure 5.6). Inspection of the HETCOR spectra indicate strong correlations between the ^{31}P resonances at 24 ppm and 1 ppm but not the -210 ppm T_d site resonance with the protons of the HDA chain centered at 1.6 ppm. This demonstrates the oxidized P sites at 24 and 1 ppm are at surface sites in close spatial proximity to the protons on the passivating ligands, while the T_d site is occupying internal sites at least one monolayer down. It is difficult to conclude if there is a correlation between the HDA protons and the peak at -9 ppm due to the overlapping of the peaks at 1 ppm and -9 ppm. From the correlations present, it is evident that the passivating layer is interacting strongly with at least two of the oxide ^{31}P peaks which confirm these are surface oxides, rather than core-oxidation or impurities in the sample.

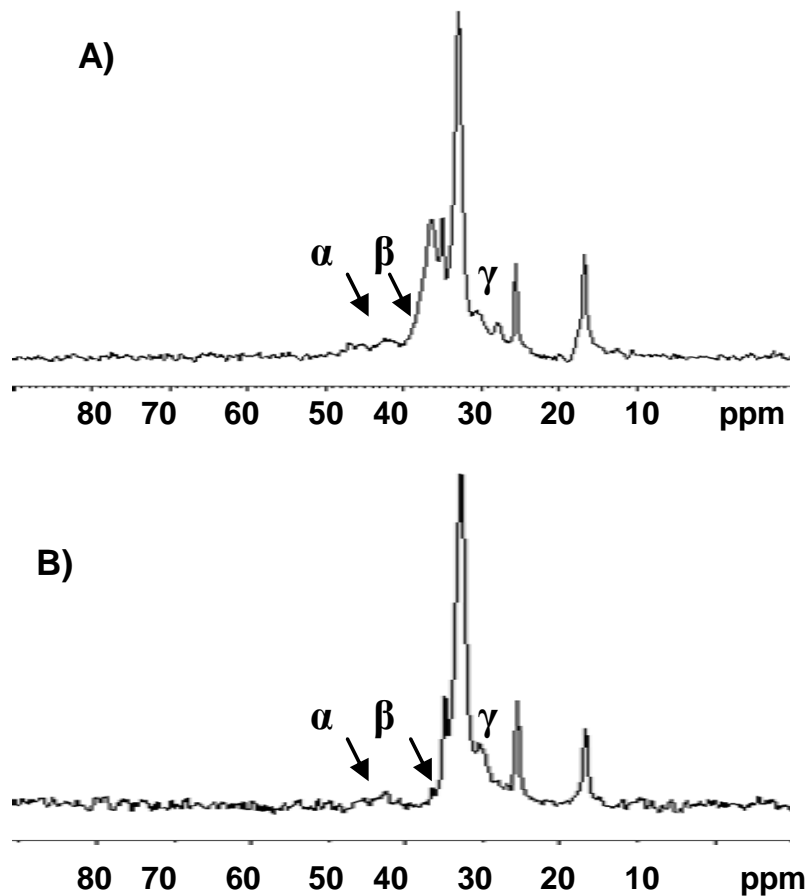


Figure 5.6. Solid-state ^{13}C single pulse spectra of HDA capped InGaP nanocrystals recorded under MAS at 12kHz. (A) unetched. (B) HF etched. The α , β , and γ -carbons of HDA are broadened due to binding to the surface of the particle.

5.3.3. Oxidation Site Characterization using ^{31}P CPMAS.

The HETCOR NMR data in combination with the ^{31}P resonance positions clearly establishes the formation of an oxide at the nanoparticle surface. More critically, the observation of no significant change between the HF etched and pre-etched InGaP nanocrystals for either the intensity of the oxidized to unoxidized P sites in the ^{31}P MAS or HETCOR data suggests the oxidation thickness and identity is identical. Further insight into the nature of the phosphorus sites can be gained by a thorough study of the chemical shifts with relation to literature precedence, and the ^1H - ^{31}P cross-relaxation time constants, T_{PH} . Many studies to date have utilized XPS to characterize the oxidation species of bulk InP,³⁶⁻⁴² where the oxidation species are InPO_4 and InPO_3 on the surface of InP crystals, although In_2O_3 has also been identified. A chemical review on oxidation of bulk III-V semiconductors by Wilmsen *et al.*^{40a} summarizes the thermal oxidation species of GaP as predominately GaPO_x with the possibility of Ga_2O_3 occurring primarily only at high temperatures. From these studies on bulk materials, a likely assignment of the phosphorus species at 24 ppm is PO_3 . A study from Bujoli-Doeuff *et al.*⁵¹ strongly supports this with the measured ^{31}P chemical shift of 25.6 ppm for $\text{Ga}(\text{OH})(\text{O}_3\text{PCH}_2\text{C}_6\text{H}_5)$. The resonances at 1 and -9 ppm are most likely due to PO_4 resonances. Recently, Kulshreshtha *et al.*⁵² has measured the ^{31}P NMR chemical shift of bulk GaPO_4 at -8.5 ppm, while Alivisatos *et al.*⁸ has indicated a surface $^{31}\text{PO}_4$ resonance at 5 ppm for trioctylphosphine oxide passivated InP quantum dots. This suggests the P species at 1 ppm and -9 ppm arise from PO_4 species with slight chemical shift differences from

the previous sites in literature most likely due to ligand effects and the mixed metal (gallium and indium) $^{31}\text{PO}_4$ species expected from the ternary InGaP material.

Although it is tempting to make the assumption the peaks at 1 ppm and -9 ppm arise from segregated InPO_4 and GaPO_4 species on the surface, further analysis of ^1H - ^{31}P cross-relaxation time constant suggests the chemical shift difference is due to P sites at different depths relative to the HDA passivant, with the -9 ppm site occurring deeper than the 1 ppm site.

Further analysis of the nature and depth of oxidation of the phosphorus sites can be gained through determination of the ^1H - ^{31}P cross-relaxation time constants, T_{PH} . The values of the ^1H - ^{31}P cross-relaxation time constants, T_{PH} , have a $1/R^6$ distance dependence and can be used to compare intermolecular distances between ^1H and ^{31}P nuclei; ⁵³ closer spatial proximities of the protons on the ligands to the phosphorus sites gives stronger dipole-dipole couplings and the maximum integrated peak intensity for CPMAS will be reached at a shorter contact time yielding lower values of T_{PH} . The cross-relaxation time constant can be calculated by measuring ^1H - ^{31}P cross-polarization magic-angle spinning (CPMAS) with contact times between 0.1 and 20 ms.

^{31}P CPMAS spectra of unetched InGaP nanocrystals with cp contact times of 2 and 15 ms, demonstrating signal intensity changes with differences in the distant dependent ^1H - ^{31}P contact times are shown in Figure 5.7A and 5.7B. As noted in the HETCOR section because similarity of the data, only the spectra for the unetched InGaP nanocrystals is shown.

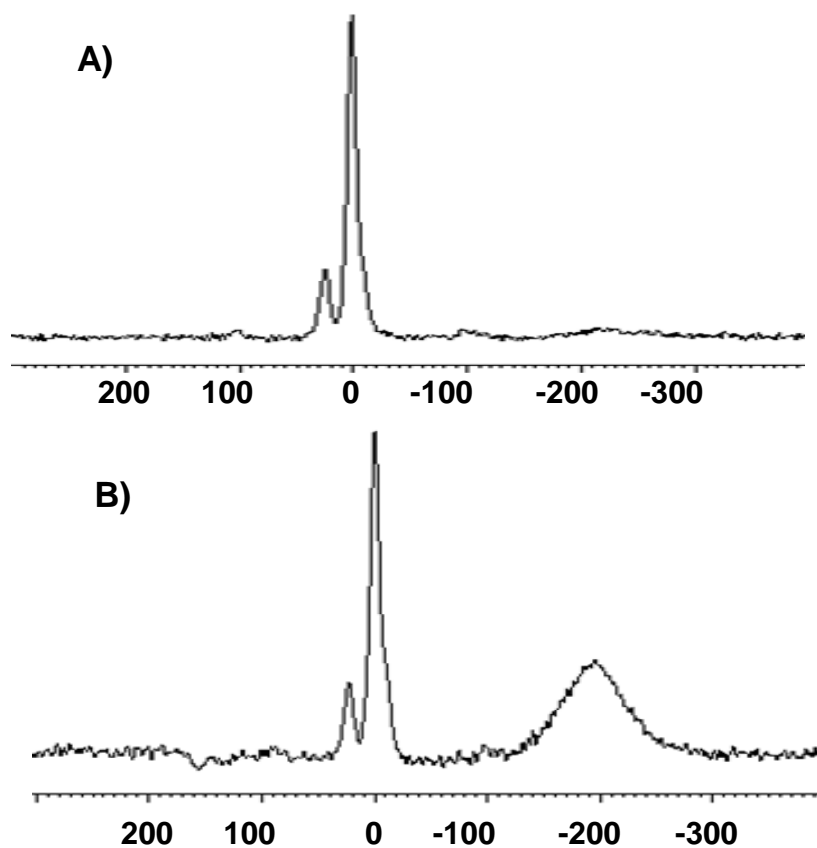


Figure 5.7. ^{31}P CPMAS spectra of unetched InGaP nanocrystals with cp contact times of (A) 2 ms and (B) 15 ms. demonstrating variations in signal intensity with increased distant dependent ^1H - ^{31}P contact times.

Integrated ^{31}P peak intensities from ^1H - ^{31}P CPMAS were plotted as a function of the contact time, τ , and fit to equation 1⁵⁴ using a nonlinear least-squares analysis to determine T_{PH} .

$$M(\tau) = M_0(\exp(-\tau/T_{1\rho\text{H}}) - \exp(-\tau/T_{\text{PH}}))/(1 - T_{\text{PH}}/T_{1\rho\text{H}}) \quad (5.1)$$

The proton spin-lattice relaxation time constants, $T_{1\rho\text{H}}$, were determined following a procedure from an earlier publication.⁵⁵ The fitted plots are shown in Figure 5.8 and the values are shown in Table 5.1. The PO_3 and PO_4 sites at 24 and 1 ppm have nearly identical CPMAS build-up curves (Figure 5.8) and the lowest T_{PH} values ($260 \pm 50 \mu\text{s}$ and $130 \pm 100 \mu\text{s}$, respectively) of all the phosphorus sites (Table 5.1). This supports the assumption that these P sites are on the surface of the particle and at approximately the same distance from the protons of the HDA chain. The CPMAS curve (Figure 5.8) for the PO_4 species at -9 ppm exhibits a slower build up and has a higher T_{PH} value of $560 \pm 100 \mu\text{s}$. The slower build-up for the same nuclei species indicates that the P site at -9 ppm is at a deeper depth relative to the protons on the $-\text{CH}_2 / -\text{NH}_2$ groups on the HDA chain suggesting oxidation also occurs within the particle. It is important to note, this only suggests near surface oxidization processes occurring from self-terminating oxide formation and does not

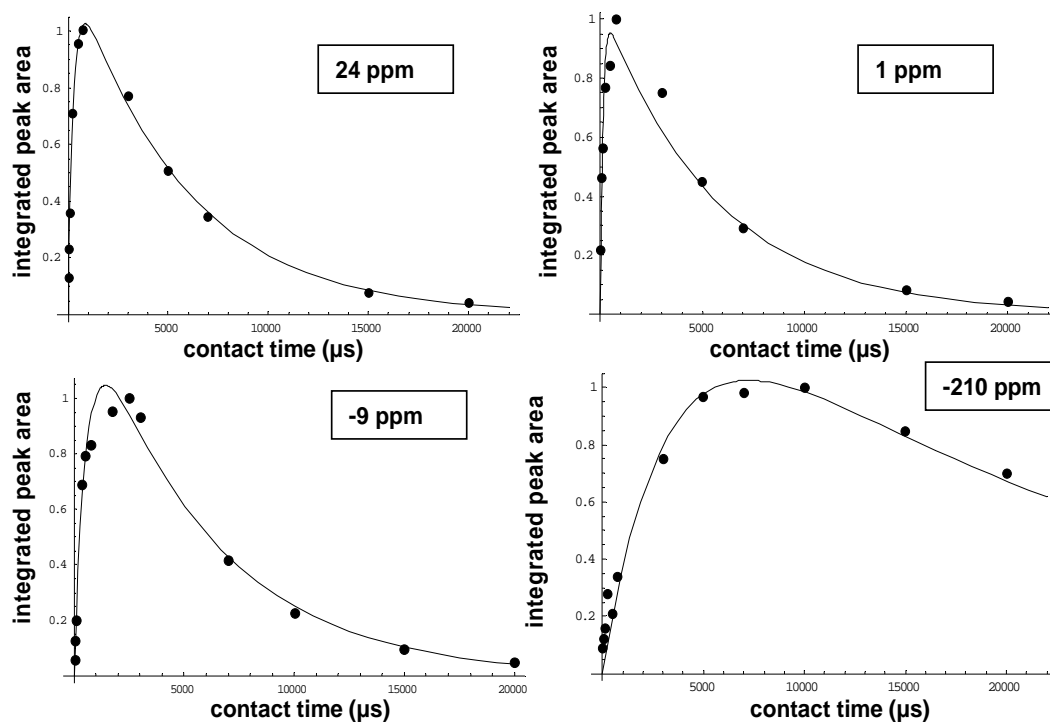


Figure 5.8. The InGaP nanocrystal integrated ^{31}P peak intensities from ^1H - ^{31}P CPMAS are plotted as a function of cp contact time, τ . This data was fit to equation 5.1 using a least-squares analysis to determine the ^1H - ^{31}P cross-relaxation time constants, T_{PH} displayed in Table 5.1.

^{31}P peak (ppm)	T_{PH} (μs)
24	260 ± 50
1	130 ± 100
-9	560 ± 100
-210	3200 ± 500

Table 5.1. InGaP nanocrystal ^1H - ^{31}P cross-relaxation time constants, T_{PH} , determined from a least-squares analysis of the data in Figure 5.8, indicating varying distances of the passivating ligands from the 4 phosphorous sites.

³¹ P Chemical Shift	Species Assignment	Position	Characterization Methods
24 ppm	PO ₃	surface	³¹ P MAS integration in time, bulk InP and GaP oxidation products, ³⁶⁻⁴² chemical shift correlation with Ga phosphonate materials, ⁵¹ HETCOR, shortest (same as 1 ppm) $T_{\rho H}$ value from CPMAS data
1 ppm	PO ₄	surface	³¹ P MAS integration in time, bulk InP and GaP oxidation products ³⁶⁻⁴² chemical shift correlation with GaPO ₄ and ³¹ PO ₄ on InP NCs, ^{52,8} HETCOR, shortest (same as 24 ppm) $T_{\rho H}$ from CPMAS data
-9 ppm	PO ₄	near surface	³¹ P MAS integration in time, bulk InP and GaP oxidation products ³⁶⁻⁴² chemical shift correlation with GaPO ₄ and ³¹ PO ₄ on InP NCs, ^{52,8} HETCOR, median $T_{\rho H}$ from CPMAS data
-210 ppm	T _d	internal	³¹ P MAS chemical shift correlation with InP and GaP, ^{48,49} HETCOR, longest $T_{\rho H}$ from CPMAS data, optical data

Table 5.2. Summary of ³¹P site assignments, positions and corresponding methods of characterization for HF etched and unetched InGaP Nanocrystals.

suggest oxidation is occurring in the core of the particle, since the -210 ppm resonance has a significantly longer build up time (T_{PH} value of $3200 \pm 500 \mu\text{s}$). This indicates that the upfield shift from the $^{31}\text{PO}_4$ peak at 1 ppm is likely from the change in electronic environment from the surface PO_4 rather than a segregated GaPO_4 species. The ^{31}P peak identifications and characterization methods are summarized in Table 5.2.

With the characterization of the oxidation sites as PO_4 and PO_3 , integration on these ^{31}P species was done to compare the amount of phosphorus in these sites as well as their rate of growth. Interestingly, the rate of growth of PO_3 is faster than PO_4 in the unetched and etched samples, with the etched sample beginning with a slightly higher amount of PO_4 . Approximately 2 months after synthesis, however, the ratio of PO_3 to PO_4 of 1:6.5 and 1:6.0 is very close for the unetched and etched samples, respectively.

5.3.4. Spatial Proximities of PO_4 and PO_3 on the Surface.

For a deeper structural elucidation of the positions of the PO_4 and PO_3 sites on the surface of the InGaP nanomaterials, 2D dipole-dipole mediated solid-state double quantum ^{31}P NMR was employed to explore the spatial proximities of the PO_3 and PO_4 sites (Figure 5.9). Since the creation of a double quantum coherence (DQC) between two ^{31}P nuclei relies on a sufficiently strong dipole-dipole coupling between them, it provides information about through-space ^{31}P - ^{31}P proximities. If two

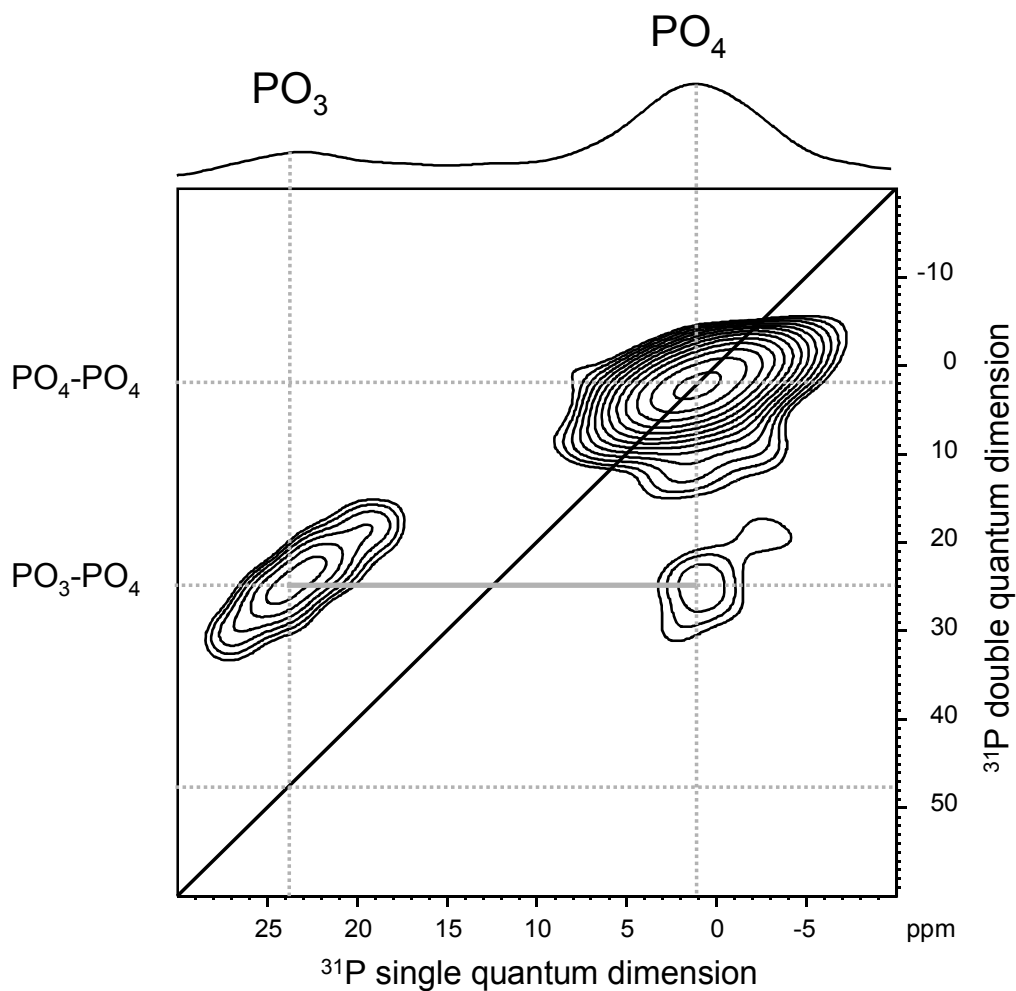


Figure 5.9. 2D Double-Quantum $^{31}\text{P}\{^{31}\text{P}\}$ NMR spectrum of unetched InGaP nanocrystals recorded under MAS at 12 kHz and an excitation time of 1.66 ms, indicating spatial proximity of PO_3 and PO_4 sites, as well as PO_4 with other PO_4 sites but not between PO_3 sites. (The one-dimensional spectrum plotted at the top is the sum-projection of the single quantum dimension.)

phosphorus sites are in close proximity in the material, they will share the same double-quantum frequency, which is the sum of the single quantum frequencies of the two nuclei involved. Thus, DQCs between the same phosphorus sites appear as so-called auto peaks on the diagonal of the DQ spectrum, while DQCs of different phosphorous sites appear as so-called cross peaks. As before, because of the similarity of the data only the unetched spectrum is shown.

The sum-projection of the single quantum dimension is shown at the top of the spectrum. Since the BABA pulse sequence must be acquired with rotor-synchronization, the spectral width in the indirect dimension is limited by the spinning speed.⁴⁷ Even at 30 kHz MAS the spectral width would be too small to fit in the whole ^{31}P spectrum. Therefore, only the surface ^{31}P sites were investigated, while the bulk ^{31}P resonance at -210 ppm was eliminated by employing cross-polarization with a contact time of 2 ms. In this way possible fold over effects of the bulk ^{31}P resonance are prevented. In addition, the cross polarization circumvents long ^{31}P T_1 relaxation times and allows for a much shorter recycle delay.

Analysis of the spectrum in Figure 5 reveals a close proximity of PO_4 and PO_3 species as revealed by the cross peaks at a double quantum frequency of 25 ppm, marked with a solid grey connecting line. Also present, is an auto peak at a DQ frequency of 2 ppm, indicating a close spatial proximity of PO_4 with other PO_4 sites. The shoulder at -9 ppm, as observed in the single-pulse experiments (Figure 5.4), is

not resolved well enough in the DQ spectrum so that no conclusions can be drawn about possible spatial proximities to the other ^{31}P sites. If PO_3 sites were in close proximity to each other, an auto peak at a double quantum frequency of 48 ppm would be expected, which is not observed. Therefore, 2D solid-state double quantum ^{31}P NMR analysis indicates close spatial proximity of the PO_3 and PO_4 sites, as well as the PO_4 with other PO_4 sites, but not PO_3 with other PO_3 sites. Importantly, this suggests that the PO_3 sites are not occupying a specific face or step-edge in the material. The PO_4 species is the predominate oxidation species as seen in the MAS spectra, and the PO_3 site is most likely a partial oxidation site on the surface, or possibly a vertex on the nanocrystal.

5.4. Conclusions.

Solid-State NMR experiments provide vital information on the nature of the structure and surface oxidation of InGaP nanocrystals. It is clear from correlation of the NMR experiments that oxidation is primarily a surface process and is constrained to the top most layers in either etched or unetched samples of the nanoparticle. This suggests that the improved PL behavior following etching is not the result of F ions at the surface or removal of the oxide layer. The observation of identical surface oxidized species present in both the etched and unetched samples is surprising in light of the work on bulk InP. Kikuchi *et al.*³⁶ has indicated through the use of XPS that chemically cleaning InP(100) surfaces in aqueous HF solutions removes the native

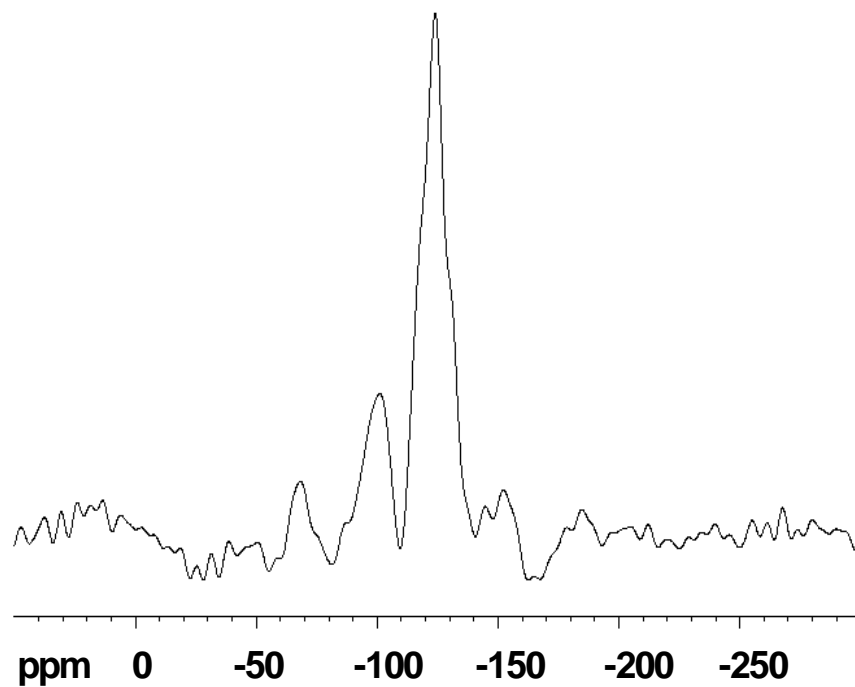


Figure 5.10. Solid-state ^{19}F single-pulse spectrum of etched InGaP nanocrystals recorded under MAS at 12 kHz (160 scans) indicating small amounts of fluorine bound to the particles post HF etching.

oxide layer and leaves behind a surface terminated by fluorine. The results on the nanoparticles suggest HF etching initially removes the oxide present in the unetched particles leaving a transient fluoride species. In fact, ^{19}F NMR (Figure 5.10) of etched InGaP nanocrystals following sample isolation indicate the presence of the small amounts of fluorine atoms after particle re-oxidation. The ^{19}F peaks in the MAS NMR spectrum cannot be adequately assigned without further correlated or time-dependent NMR measurements.⁵⁶ This suggests the fluoride ion must be labile resulting in re-oxidation of the particle after exposure to air. Fluoride ion liability is a known process for HF etched Si-wafers in the electronics industry. The re-oxidation process may result in a reconstructed surface, which would indicate the reconstruction is the more critical process for enhanced PL.

With this hypothesis, the similarity of the unetched and etched oxidized phosphorus peaks at 24, 1, and -9 ppm therefore indicate a propensity of InGaP nanocrystals to oxidize to a specific structure. The surface oxide on etched and unetched InGaP nanocrystals is PO_3 and PO_4 in a ratio of $\sim 1:6$ with PO_3 growing at a slightly higher rate than PO_4 over time when exposed to air. The PO_4 species is present on the surface, as well as within the quantum dot. The study also supports the close proximity of PO_4 sites with other PO_4 sites as well as PO_3 , while PO_3 is not in close proximity to other PO_3 sites. Thus, the PO_3 sites must be surrounded by PO_4 . From these results on the phosphorus sites and oxidation, it is apparent that an investigation into the gallium and indium sites is necessary for a full understanding of

the relation of surface structure and quantum efficiency in HF etched and unetched InGaP nanocrystals, which will be discussed further in Chapter 6.⁵⁶

5.5. References.

1. Colvin, V. L. *Nature Biotech.* **2003**, *21*, 1166-1170.
2. Derfus, A.M.; Chan, W.; Bhatia, S. *Nano Lett.* **2004**, *4*, 11-18.
3. Battaglia, D.; Peng, X. *Nano. Lett.* **2002**, *2*, 1027-1030.
4. Talabin, D.V.; Rogach, A.L.; Mekis, I.; Haubold, S.; Kornowski, A.; Haase, M. Weller, H. *Colloids and Surfaces*, **2002**, *202*, 145-154.
5. a) Micic, O.I.; Sprague, J.R.; Curtis, C.J.; Jones, K.M.; Machol, J.L.; Nozik, A.J.; Giessen, H.; Fluegel, B. Mohs, G.; Peyghambarian, N. *J. Phys. Chem.* **1995**, *99*, 7754-7759. b) Micic, O.I.; Sprague, J.; Lu, Z.; Nozik, A.J. *Appl. Phys. Lett.* **1996**, *68*, 3150-3152.
6. Guzelian, A.A.; Katari, J.E.B; Kadavanich, A.V.; Banani, U.; Hmad, E.; Juban, E.; Alivisatos, A.P. *J. Phys. Chem.* **1996**, *100*, 7212-7219.

7. a) Adam, S.; Weller, H. et al. *Eur. Phys. J. D.* **2003**, *24*, 373-376. b) Talapin, D.; Gaponik, N.; Borchert, H.; Rogach, A. L.; Haase, M.; Weller, H. *J. Phys. Chem. B.* **2002**, *106*, 12659-12663.
8. Tomaselli, M.; Yarger, J.L.; Bruchez, M.; Havlin, R.H.; deGraw D.; Pines, A.; Alivisatos, A.P. *J. Chem. Phys.* **1999**, *110*, 8861-8864.
9. Fu, H.; Zunger, A. *Phys. Rev. B.* **1997**, *56*, 1496-1508.
10. Langof, L.; Ehrenfreund, E.; Lifshitz, E.; Micic, O.I.; Nozik, A.J. *J. Phys. Chem. B.* **2002**, *106*, 1606-1612.
11. Micic, O.I.; Nozik, A.J.; Lifshitz, E.; Rajh, T.; Poluektov, O.G.; Thurnauer, M.C. *J. Phys. Chem. B.* **2002**, *106*, 4390-4395.
12. Kim, S.; Bawendi, M.G. *J. Am. Chem. Soc.* **2003**, *125*, 14652-14653.
13. Zezza, F.; Comparelli, R.; Striccoli, M.; Curri, M. L.; Tommasi, R.; Agostiano, A.; Della Monica, M. *Synth. Met.* **2003**, *139*, 597-600.
14. Guo, W.; Li, J. J.; Wang, Y. A.; Peng, X. *J. Am. Chem. Soc.* **2003**, *125*, 3901-3909.

15. Jang, E.; Jun S.; Chung, Y.; Pu, L. *J. Phys. Chem. B* **2004**, *108*, 4597-4600.
16. Kityk, I. V.; Kassiba, A.; Tuesu, K.; Charpentier, C.; Ling, Y.; Makowska-Janusik, M. *Mater. Sci. Eng., B* **2000**, *B77*, 147-158.
17. Berrettini, M.G.; Braun, G.; Hu, J.G.; Strouse, G.F. *J. Am. Chem. Soc.*, **2004**, *22*, 7063 -7070.
18. Meulenberg, R. W.; Bryan, S.; Yun, C. S.; Strouse, G. F. *J. Phys. Chem B* **2002**, *106*, 7774-7780.
19. Meulenberg, R. W.; Strouse, G. F. *J. Phys. Chem. B* **2001**, *105*, 7438-7445.
20. Puzder, A.; Williamson, A.J.; Reboredo, F.; Galli G. *Phys .Rev. Lett.* **2003**, *9*, 157405.
21. Puzder, A.; Williamson, A.J.; Gygi, F.; Galli G. *Phys .Rev. Lett.* **2004**, *92*, 217401.
22. Pokrant, S.; Whaley K.B. *Eur. Phys. J. D.* **1999**, *6*, 255-267.
23. Raola, O.; Strouse, G.F. *Nano Lett*, **2002**, *2*, 1443-1447.

24. Hamad, K.S.; Roth, R. Rockenberger, J.; van Burren, T.; Alivisatos, A.P. *Phys. Rev. Lett.* **1999**, *83*, 3474.
25. Zhang, J.; Wu, Z. Y.; Ibrahim, K.; Abbas, M. I.; Ju, X. *Nucl. Instrum. Methods Phys. Res., Sect. B* **2003**, *199*, 291-294.
26. Wei, Z.; Sun, L.; Jiang, X.; Liao, C.; Yan, C.; Tao, Y.; Zhang, J.; Hu, T.; Xie, Y. *Chem. Mater.* **2003**, *15*, 3011-3017.
27. Page, K.; Proffen, T.; Terrones, H.; Terrones, M.; Lee, L.; Yang, Y.; Stemmer, S.; Seshadri, R.; Cheetham, A. K. *Chem. Phys. Lett.* **2004**, *393*, 385-388.
28. Borchert, H.; Haubold, S.; Weller, H.; McGinley, C. Riedler, M.; Moller, T. *Nano. Lett.* **2002**, *2*, 151-154.
29. Asami, H.; Abe, Y.; Ohtsu, T.; Kamiya, I.; Hara, M. *J. Phys. Chem. B* **2003**, *107*, 12566-12568.
30. Rodriguez-Lopez, J.; Montejano-Carrizales, J.; Pal, U.; Sanchez-Ramirez, J.; Troiani, H.; Garcia, D.; Miki-Yoshida, M.; Jose-Yacaman, M. *Phys. Rev. Lett.* **2004**, *92*, 196102.

31. Li, R.; Lee, J.; Yang, B. ; Horspool, D. ; Aindow, M.; Papadimitrakopoulos, F. *J. Am. Chem. Soc.* ASAP.
32. Mayeri, D.; Phillips, B.L.; Augustine, M.; Kauzlarich, S.M. *Chem. Mater.* **2001**, *13*, 765-770.
33. Elbaum, R.; Vega, S.; Hodes, G. *Chem. Mater.* **2001**, *13*, 2272-2280.
34. Ladizhansky, V.; Vega, S. *J. Phys. Chem. B* **2000**, *104*, 5237-5241.
35. a) Mikulec, F. V.; Kuno, M.; Bennati, M.; Hall, D. A.; Griffin, R. G.; Bawendi, M. *G. J. Am. Chem. Soc.* **2000**, *122*, 2532-2540. b) Becerra, L. R.; Murray, C. B.; Griffin, R. G.; Bawendi, M. *G. J. Chem. Phys.* **1994**, *100*, 3297-3000.
36. Kikuchi, D.; Adachi, S. *Mat. Sci. Eng.* **2000**, *B76*, 133-138.
37. Hollinger, G. ; Bergignat, E.; Joseph, J.; Robach, Y. *J. Vac. Sci. Technol. A* **1985**, *3*, 2082-2088
38. Chen, G.; Visbeck, S.B.; Law D.C.; Hicks, R.F. *J. Appl. Phys.* **2002**, *19*, 9362-9367.

39. a) Simpson, W.C.; Yarmoff, J.A. *Annu. Rev. Phys. Chem.*, **1996**, *47*, 527. b) Thurgate, S.M.; Erickson, N.E. *J. Vac. Sci. Technol. A* **1990**, *8*, 3669-3675.
40. a) Wilmsen, C.W. *J. Vac. Sci. Technol.* **1981**, *19*, 279-289. b) Wilmsen, C.W. *J. Vac. Sci. Technol.* **1996**, *19*, 279-289.
41. Guivarch, A.; Haridon, L.; Pelous, G. *J. Apply. Phys.* **1984**, *55*, 1139-1148.
42. a) b) Wager, J.F.; Geib, C.M.; Wilmsen, C.W.; Kazmerski, L.L. *J. Vac. Sci. Technol.* **1983**, *1*, 778-783. Goehring, L.; Michal, C.A. *J. Chem. Phys.* **2003**, *119*, 10325-10329.
44. Christiansen, S. C.; Zhao, D.; Janicke, M. T.; Landry, C. C.; Stucky, G.; Chmelka, B. F. *J. Am. Chem. Soc.* **2001**, *123*, 4519-4529.
45. Hedin, N.; Graf, R.; Christiansen, S.C.; Gervais, C.; Hayward, R.C.; Eckert, J.; Chmelka, B.; *J. Am. Chem. Soc.* **2004**, *126*, 9425-9432.
46. van Rossum, B.J.; Foerster, H.; de Groot, H. J. M. *J. Magn. Reson.* **1997**, *124*, 516.

47. Feike, M; Graf, R.; Schnell, I.; Jäger, C.; Spiess, H. W. *J. Am. Chem. Phys.* **1996**, *118*, 9631.
48. Tomaselli, M; deGraw D.; Yarger, J.L.; Augustine, M.P.; Pines, A. *Phys. Rev. B.* **1998**, *58*, 8627-8633.
49. Sears, R.E. *J. Phys. Rev.* **1978**, *18*, 3054-3058.
50. Thayer, A. M.; Steigerwald, M. L.; Duncan, T. M.; Douglass, D. C. *Phys. Rev. Lett.* **1988**, *60*, 2673-2676.
51. Bujoli-Doeuff, M.; Evain, M.; Fayon, F.; Alonso, B.; Massiot, D.; Bujoli, B. *Eur. J. Inorg. Chem.* **2000**, 2497-2499.
52. Kulshreshtha, S.K.; Jayakumar, O.D.; Sudarsan, V. *J. Phys. Chem. Sol.* **2004**, *65*, 1141-1146.
53. Klein Douwel, C. H.; Maas, W. E. J. R.; Veeman, W. S.; Werumeus Buning, G. H.; Vankan, J. M. J. *Macromolecules* **1990**, *23*, 406-412.
54. Mehring, M. *High-Resolution NMR Spectroscopy in Solids*; Springer-Verlag: New York, 1976.

55. Voelkel, R. *Angew. Chem., Int. Ed. Engl.* **1988**, 27, 1468-1483.

56. Berrettini, M.G.; Raab, C.; Strouse, G.F.; Chmelka, B. manuscript in preparation

Chapter 6. HF etching and the Surface Structure of InGaP Nanocrystals.

6.1. Introduction.

With the development of synthetic protocols that produce high quality III-V semiconductor nanocrystals¹⁻⁶ which are being looked to for applications in electrical and opto-electrical devices, characterization of the surfaces and interfaces in these nanomaterials becomes crucial for development of an understanding of structure-property relationships. Interestingly, hydrogen fluoride (HF) etching of III-V semiconductor nanocrystals has been shown to greatly improve the quantum efficiency of the material. In recent years, there have been studies investigating the correlation between optical properties and molecular structure in pre and post HF etched InP quantum dots,⁷⁻¹² and various models have been suggested; for example, Nozik *et al.* has suggested through analysis of photoluminescence, optically detected magnetic resonance (ODMR) studies and electron paramagnetic resonance (EPR)^{7, 10-11}, that HF etching of InP nanocrystals fills surface phosphorus vacancies, which dominate unetched samples, with fluoride ions as well as replace oxygen in the oxide layer, while leaving behind a small amount of phosphorus vacancies in the core. Utilizing surface sensitive photoelectron spectroscopy (PES) technique with synchrotron radiation, Weller *et al.*⁸ has indicated the removal of unpassivated phosphorus atoms from the nanocrystal surface, followed by increased passivation with

trioctylphosphine oxide or fluorine from the etching process, as significant in the observed increase in quantum efficiency.

Recent studies have proven ^{13}P solid-state nuclear magnetic resonance (NMR) spectroscopy an excellent spectroscopic tool for analyzing surfaces and interfaces in InP^{13} and InGaP^{14} nanocrystals. Analysis of hexadecylamine (HDA) passivated InGaP nanocrystals has shown identical phosphorus species, proximities, and depth of phosphorus oxidation on pre and post HF etched materials through 1D and 2D ^{31}P NMR experiments (Chapter 5). With the establishment of indistinguishable phosphorus identities from solid-state NMR analysis, investigation into the indium and gallium sites in the unetched and etched material is necessary for a better understanding of molecular structure and quantum efficiency.

In this chapter, a solid-state NMR study of pre and post HF etched thermally grown HDA passivated InGaP nanocrystals is reported. Through ^{71}Ga and ^{115}In NMR experiments, insight into the nature and position of the gallium and indium sites, as well as the associated surface reconstruction from HF treatment, was gained. In conjunction with the previous work on the characterization of the phosphorus sites in this material (Chapter 5),¹⁴ this study strongly suggests the significance of an HF treatment driven surface reconstruction to a more ordered environment surrounding the surface atoms with the increased quantum efficiency observed in HF etched InGaP nanocrystals.

6.2. Experimental Section.

6.2.1. Synthesis of InGaP Nanocrystals.

InGaP nanocrystals (unetched) were prepared with modifications to previously published procedures for InP and InGaP nanocrystals¹⁵⁻¹⁷ and as reported in Chapter 5. The unetched HDA passivated InGaP particles were spherical, Zn blende 4.5 nm particles and did not exhibit a detectable PL ($\Phi_{EM} < 0.01$) The absorbance spectrum and TEM image are shown in Figures 5.1 and 5.2 (Chapter 5).

6.2.2 Etching of InGaP Nanocrystals.

The etched InGaP nanocrystals were prepared by the addition of a 5 % HF MeOH solution with illumination (365 nm) as described in Chapter 5. The etched InGaP nanoparticles are spherical Zn blende nanoparticles with a size of 4.5 nm and emit with a PL quantum yield of 8% (in dry degassed toluene) when excited at 420 nm. The TEM images and absorbance and emission spectra are shown in Figure 5.1 and 5.3 (Chapter 5).

6.2.3. NMR.

Solid-state ^{71}Ga and ^{115}In MAS NMR experiments were performed at room temperature on a Bruker 500 MHz Avance spectrometer with a 4-mm broadband MAS probe operating at 152.7 MHz for ^{71}Ga and for 109.6 MHz ^{115}In . A spinning speed of 14 kHz was used in all experiments and the chemical shifts of ^{71}Ga and ^{115}In were referenced to $\text{Ga}(\text{NO}_3)_3$ and $\text{In}(\text{NO}_3)_3$, respectively.

The ^{71}Ga spin-echo experiments were performed with an acquisition time of 4.2 ms, a recycling delay of 2 s, and a 90° and 180° pulse of 1.6 μs and 3.2 μs , respectively.

The ^{115}In spin-echo experiments were performed with an acquisition time of 1.7 ms, a recycling delay of 1 s, and a 90° and 180° pulse of 0.64 μs and 1.28 μs , respectively.

6.3. Results and Discussion.

6.3.1. Gallium Occupation and Molecular Order.

^{31}P solid-state NMR experiments have provided fundamental information on the nature of phosphorus surface oxidation of in thermally grown HDA passivated InGaP nanocrystals before and after HF etching (Chapter 5).¹⁴ These results suggest that the large increase in quantum yield after etching is not likely caused from phosphorus oxidation because of the considerable similarity of the oxide structure of unetched and HF etched InGaP nanocrystals. The structure

involves PO₃ and PO₄ surface species that are in a ratio of ~1:6 with PO₄ also present sub-surface. The study also supports the close proximity of PO₄ sites with other PO₄ sites as well as PO₃, while PO₃ is not in close proximity to other PO₃ sites. From this information, a need for a study of the gallium and indium sites becomes evident for a more complete understanding of the relation of surface structure and quantum efficiency in HF etched and unetched InGaP nanocrystals. Solid-state NMR experiments of ⁷¹Ga and ¹¹⁵In were acquired in order to investigate any structural changes within these sites with HF etching.

⁷¹Ga spin-echo NMR spectra, of unetched and HF etched HDA passivated InGaP nanocrystals are shown in Figure 6.1A and 6.1B, respectively; this NMR technique is beneficial for broad peaks and probes the entire the nanocrystal (surface and core). The site occupation of gallium atoms in the particles is unknown and therefore probing the entire nanocrystal is necessary. The unetched InGaP nanocrystals had a weak ⁷¹Ga NMR signal during measurement and therefore, a large numbers of scans (216,096 scans for 75 mg of sample) were necessary for adequate signal to noise in the spectrum (Figure 6.1A). The largest peak centered at 300 ppm with a linewidth $\delta_{1/2} = 170$ ppm corresponds closely to the chemical shift for bulk GaP (Figure 6.2) of 302 ppm ($\delta_{1/2} = 3$ ppm) allowing for the assignment of this peak as gallium tetrahedrally coordinated to phosphorus as determined from the zinc blende cubic structure of GaP and InGaP; although, the depth of the gallium atoms in the nanocrystal are still unknown from this

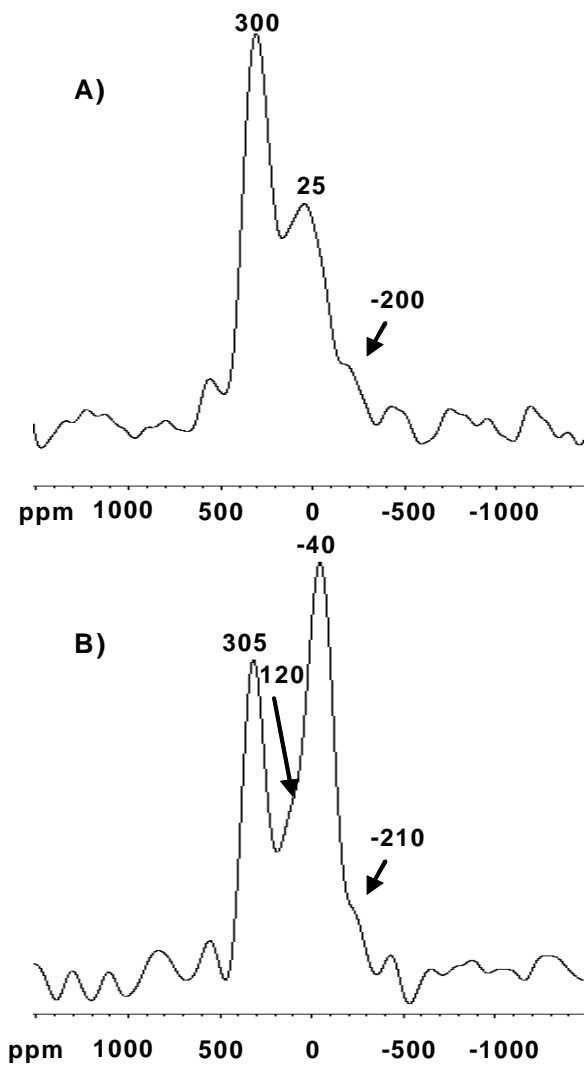


Figure 6.1. Solid-state ^{71}Ga spin-echo MAS NMR spectra of InGaP nanocrystals demonstrating a change in the population and increase in order of the Ga sites of the particle after HF etching (A) unetched (216,096 scans; 75 mg) (B) HF etched (81088 scans; 64 mg). (Spinning speed, 14 kHz)

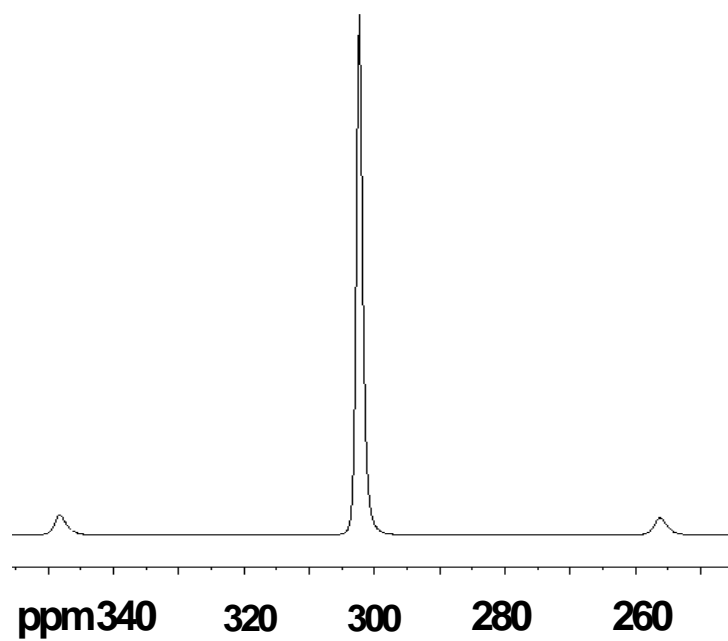


Figure 6.2. ^{71}Ga spin-echo MAS NMR spectra of bulk GaP. (Spinning speed, 14 kHz)

determination as they could reside in the core or only one layer down from the oxidized surface with this coordination. The upfield components have a large peak centered at approximately 25 ppm, with possibly a small shoulder peak at -200 ppm, although the signal to noise makes this difficult to decipher. With known PO_4 and PO_3 oxidation on the surface of the particle as well as PO_4 oxidation in the near surface region of the particle (Chapter 5),¹⁴ a likely assignment of the large upfield component at 25 ppm is gallium atoms at the oxidized surface and near surface which can be supported by investigation of ^{71}Ga NMR chemical shifts of gallium based phosphonate hybrid materials. For example, Bujoli *et al.*¹⁸ measures the ^{71}Ga NMR chemical shifts of $\text{Ga}(\text{OH})(\text{O}_3\text{PCH}_3)$, and $\text{Ga}(\text{OH})(\text{O}_3\text{PCH}_2\text{C}_6\text{H}_5)$ at $-13 \text{ ppm} \pm 10 \text{ ppm}$ and $10 \text{ ppm} \pm 10 \text{ ppm}$, respectively, which corresponds well to the chemical shift of the upfield component at 25 ppm for gallium bound to oxidized phosphorus species in the particles. Although phosphorus oxidation is known from investigation of ^{31}P NMR experiments,¹⁴ this technique does not give information on oxidation in the form of Ga_2O_3 . A chemical review on oxidation of bulk III-V semiconductors by Wilmsen *et al.* summarizes the thermal oxidation species of GaP as predominately GaPO_x with the possibility of Ga_2O_3 , mostly at high temperatures.¹⁹ With this information and the ^{71}Ga NMR chemical shifts of 40 ppm and 200 ppm²⁰ reported for gallium in tetrahedral and octahedral sites, respectively, for $\beta\text{-Ga}_2\text{O}_3$, the possibility of a Ga_2O_3 species on the InGaP particles cannot be ruled out. Hence, the broad upfield ^{71}Ga signal centered at 25 ppm could have overlapping peaks of

both gallium oxidation species. Due to the large signal to noise, the peak at -200 ppm is difficult to clearly determine as a resonance; but, it appears in the HF etched spectrum (Figure 6.1B) also, suggesting a valid ^{71}Ga NMR resonance. Taking into account the upfield chemical shift, a likely assignment is some type of a reconstructed gallium site which is also bound to an oxidized phosphorus species. Some possibilities include gallium in a vertex or edge site on the surface of the particle because of the small population in this particular peak.

With HF treatment on the unetched particles, a slight decrease in surface atoms may be expected with etching and therefore a weaker ^{71}Ga NMR signal than observed in the unetched particles could be expected. But, intriguingly, a dramatically stronger signal was observed (Figure 6.1B) in HF etched InGaP nanocrystals; even with a smaller sample size of the etched InGaP sample (75mg for etched vs. 64 mg for unetched), which also decreases signal intensity, the etched sample had similar signal to noise of the unetched sample with approximately a third number of scans (81,088 vs. 216096 scans) in the ^{71}Ga spin-echo NMR experiments. The peak corresponding to the gallium tetrahedrally coordinated to phosphorus appears at 305 ppm with a smaller linewidth ($\delta_{1/2} = 130$ ppm) than the unetched sample suggesting a change in this sight. The upfield region associated with oxidized phosphorus bound gallium and gallium oxide sites, is significantly different than in the unetched spectrum. There is a large peak centered at -40 ppm with a smaller overlapping peak at 120 ppm. As well as

having differing chemical shifts, these upfield peaks appear sharper, suggesting less chemical shift distribution and more order. Also, the gallium population ratio of the upfield region to the bulk-like peak is much greater in than in the unetched sample. With the appearance of the two peaks at -40 ppm and 120 ppm, and taking into consideration the chemical shifts of gallium phosphonates¹⁸ and Ga₂O₃²⁰ and the population differences with more gallium expected to be in the form of GaPO_x,¹⁹ a likely characterization of these peaks gallium bound to the oxidized phosphorus species present (PO₄ and PO₃) and Ga₂O₃, respectively. The smaller broad peak remains in the etched spectrum also with a very slight shift to -210 ppm.

In order to fully interpret these ⁷¹Ga NMR results including signal intensity change with etching, an in depth look at quadrupolar nuclei interactions, such as ⁷¹Ga (spin 3/2), had to be explored. Unlike spin ½ systems, these nuclei possess a spheroidal distribution of nuclear charge which is described by the nuclear electric quadrupole moment, eQ , that is an intrinsic property of the nucleus, and is the same regardless of the molecular environment. However, the quadrupolar nucleus is affected by the interaction with the electric field gradient (spatial changes in electric field) caused by surrounding atoms. Thus, in sites where a substantial electric field gradient is present, this quadrupolar interaction becomes significant and can broaden the signal of these nuclei so greatly that the spins just appear as broad humps in the baseline which become “invisible” with any baseline distortion; but, with an increasing spherical or undistorted

environment of charge from the surrounding molecular environment, the electric field gradients can cancel each other, giving a smaller interaction and smaller electric field gradient felt at the nucleus; these “invisible” spins become less broad with this increasing spherical or “ordered” environment of charge about the nuclear site and can become detected in the NMR spectra.²¹ Therefore, this indicates in the InGaP nanocrystal system that HF etching drives an ordered reconstruction of the surface. The ⁷¹Ga quadrupole interactions decrease with the more spherical environment from surface reconstruction resulting in more order in the surface and therefore, the “invisible” gallium sites which were broadened beyond detection in the unetched particles become visible and we get a stronger signal in a much shorter amount of time.

As HF etching is a surface treatment, only the surface or near surface atoms should be affected by the removal of atoms and the associated reconstruction. Therefore, with the significant change in the peaks in the upfield region of the ⁷¹Ga spin-echo spectra with etching, this supports the characterization of these peaks as gallium coordinated to the oxidized surface or near surface. The peak associated with bulk GaP coordination (~300 ppm) is more difficult to verify as a surface site or near surface as the change in this sight is not as great with etching; although, the decrease in the linewidth suggests a decrease in chemical shift distribution which would support this being a near surface site which is affected by the surface reconstruction with etching. Additional experiments, including spin counting and Rotational-Echo DOuble

Resonance (REDOR) at a higher field, are underway to measure the increase in ^{71}Ga measured with etching in each site as well as the relative distance of the gallium sites to the surface ligands in order to confirm their identities.

6.3.2. Indium Occupation.

Investigation into the indium sites of the material was accomplished by measuring ^{115}In spin-echo NMR spectra, of unetched and HF etched HDA passivated InGaP nanocrystals, shown in Figure 6.3A and 6.3B, respectively. Both spectra stretch over a large chemical shift range (~ -250 - 1100 ppm) and do not show distinctly separated peaks as in the gallium spectra (Figure 1). This is likely due to a large chemical shift distribution and a relative lesser sensitivity of the ^{115}In nuclei chemical shift to environment than ^{71}Ga . Although, as with the gallium spectra, it is apparent in the ^{115}In spectra that a stronger signal was observed (Figure 6.3B) with less scans and a smaller sample size (unetched: 128,000 scans, 75 mg; HF etched: 96,640 scans, 64 mg), suggesting a decrease in the quadrupolar interactions from an ordered reconstruction of the surface and near surface following HF treatment indicating the presence of some indium in this region. The largest peak centered at 780 ppm in both spectra, corresponds closely to the chemical shift for bulk InP ($\delta = 787$ ppm; Figure 6.4) allowing for the assignment of this peak as indium tetrahedrally coordinated to phosphorus as determined from the crystal structure of InP and InGaP. There is a shoulder peak

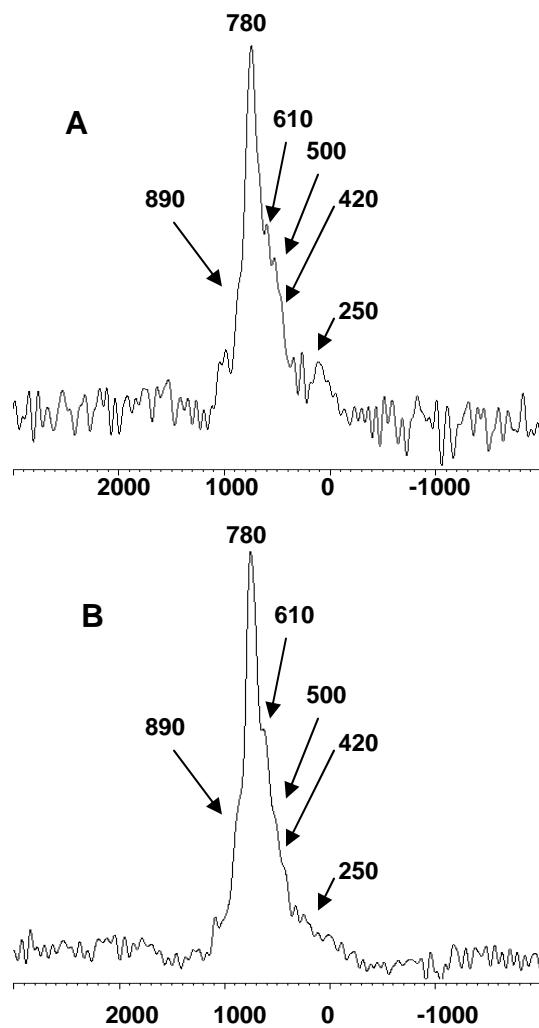


Figure 6.3. ^{115}In spin-echo MAS NMR spectra of InGaP nanocrystals indicating more order in the In sites after HF etching. (A) Unetched (128,000 scans; 75 mg) (B) HF etched (96,640 scans; 64 mg) (Spinning speed, 14 kHz)

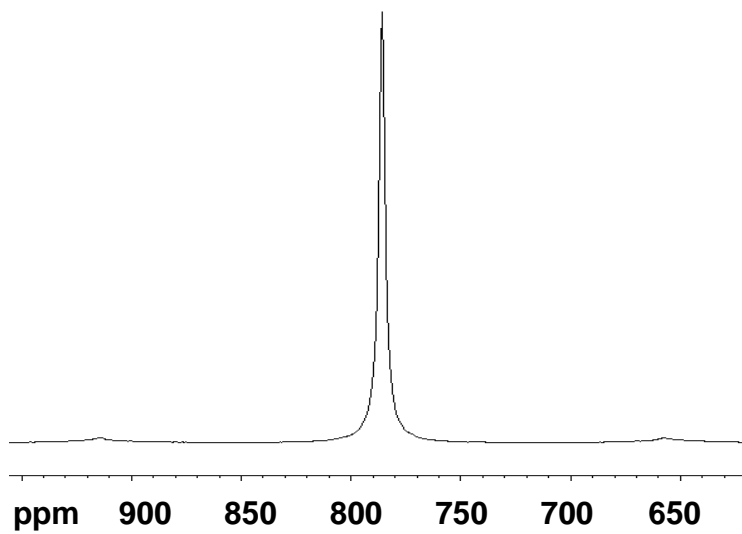


Figure 6.4. ^{115}In spin-echo MAS NMR spectra of bulk InP. (Spinning speed, 14 kHz)

downfield of this appearing at ~ 890 ppm in both spectra, which is difficult to characterize but could possibly be a reconstructed indium site near the oxidation/core interface still tetrahedrally coordinated to phosphorus from the chemical shift. The upfield components of both spectra appear as shoulder peaks at approximately 610, 500, and 420 ppm, with a very broad component at ~ 250 ppm; with the ^{115}In NMR chemical shift for indium containing beta zeolites ($\text{SiO}_2/\text{In}_2\text{O}_3$) reported at 236 ppm²² and the upfield portion in the ^{71}Ga spin-echo NMR spectra (Figure 6.1) corresponding to surface sites, it is likely that the upfield components of the ^{115}In spectra (Figure 6.3) correspond to surface or near surface indium. Wilmsen *et al.* indicates the thermal oxidation species of bulk InP as predominately InPO_x (likely a phosphate) and In_2O_3 ¹⁹ suggesting that both species are possible in our system. Accurate spin counting and REDOR NMR experiments are underway at higher fields to fully explore these possibilities.

6.4. Conclusions.

The results of ^{71}Ga spin-echo NMR experiments suggest that gallium atoms reside on the surface and near surface of colloiddally-prepared HDA passivated InGaP nanocrystals. Characterization of the gallium sites include gallium tetrahedrally coordinated to phosphorus atoms, gallium bound to the oxidized phosphorus species present (PO_4 and PO_3) and gallium likely in the form of Ga_2O_3 ; an additional minor site with a small population of gallium is also present which is most likely a reconstructed edge or vertex gallium. ^{71}Ga spin-

echo NMR comparison of unetched and HF etched particles reveal more order in the gallium sites after etching as detected from a decrease in quadrupole interactions, suggesting HF treatment drives an ordered reconstruction of the surface. Intriguingly, HF has been found to promote crystallization of organic amine templated indium phosphate phases.²³ Analysis of ¹¹⁵In NMR also suggests more order in indium surface sites post etching as well, although the results are not as pronounced as the ⁷¹Ga results. A large chemical shift distribution and a decreased sensitivity of chemical shift to electronic environment are present for the ¹¹⁵In NMR data. Approximately 6 indium sites can be detected with the most upfield region likely representing indium bound to the oxidized phosphorus species and in the form of In₂O₃ at the surface or near surface. Investigation of the indium, gallium, and phosphorus¹⁴ sites in HDA passivated InGaP nanocrystals reveal the largest structural difference observed by solid-state NMR of HF etched and unetched particles is the increased order in the surface sites post etching which is likely a significant factor in the increase in quantum yield with HF etching.

6.5. References

1. Micic, O.I.; Sprague, J.R.; Curtis, C.J.; Jones K.M.; Machol, J.L.; Nozik, A.J.; Giessen, H.; Fluegel, B.; Mohs, G.; Peyghambarian, N. *J. Phys. Chem.* **1995**, *99*, 7754-7759.
2. Guzelian, A.A.; Katari, J.E.B; Kadavanich, A.V.; Banani, U.; Hmad, E.; Juban, E.; Alivisatos, A.P.; Wolters, R.H.; Arnold, C.C.; Heath, J.R. *J. Phys. Chem.* **1996**, *100*, 7212-7219.
3. Borchert, H.; Haubold, S.; Haase, M.; Weller, H.; McGinley, C.; Riedler, M.; Moller T. *Nano. Lett.* **2002**, *2*, 151-154.
4. Talabin, D.V.; Rogach, A.L.; Mekis, I.; Haubold, S.; Kornowski, A.; Haase, M. Weller, H. *Colloids Surf.*, **2002**, *202*, 145-154.
5. Battaglia, D.; Peng, X. *Nano. Lett.* **2002**, *2*, 1027-1030.
6. Gerbec, J.; Strouse, G.F.; manuscript in preparation.
7. Micic, O.I.; Sprague, J.; Lu, Z.; Nozik, A.J. *Appl. Phys. Lett.* **1996**, *68*, 3150-3152.

8. Adam, S.; Weller, H. et al. *Eur. Phys. J. D.* **2003**, *24*, 373-376.
9. Fu, H.; Zunger, A. *Phys. Rev. B.* **1997**, *56*, 1496-1508.
10. Langof, L.; Ehrenfreund, E.; Lifshitz, E.; Micic, O.I.; Nozik, A.J. *J. Phys. Chem. B.* **2002**, *106*, 1606-1612.
11. Micic, O.I.; Nozik, A.J.; Lifshitz, E.; Rajh, T.; Poluektov, O.G.; Thurnauer, M.C. *J. Phys. Chem. B.* **2002**, *106*, 4390-4395.
12. Talapin, D.; Gaponik, N.; Borchert, H.; Rogach, A. L.; Haase, M. ; Weller, H. *J. Phys. Chem. B.* **2002**, *106*, 12659-12663.
13. Tomaselli, M; Yarger, J.L.; Bruchez, M.; Havlin, R.H.; deGraw D.; Pines, A.; Alivisatos, A.P. *J. Chem. Phys.* **1999**, *110*, 8861-8864.
14. Berrettini, M.G.; Raab, C.; Rapp A.; Braun G.; Gerbec, J.; Chmelka, B.; Strouse, G.F.; manuscript in preparation.
15. Battaglia, D.; Peng, X. *Nano. Lett.* **2002**, *2*, 1027-1030.

16. Talabin, D.V.; Rogach, A.L.; Mekis, I.; Haubold, S.; Kornowski, A.; Haase, M. Weller, H. *Colloids and Surfaces*, **2002**, *202*, 145-154.
17. Micic, O.I.; Sprague, J.R.; Curtis, C.J.; Jones, K.M.; Machol, J.L.; Nozik, A.J.; Giessen, H.; Fluegel, B. Mohs, G.; Peyghambarian, N. *J. Phys. Chem.* **1995**, *99*, 7754-7759.
18. Bujoli-Doeuff, M.; Evain, M.; Fayon, F. ; Alonso, B. ; Massiot, D. ; Bujoli, B. *Eur. J. Inorg. Chem.* **2000**, 2497-2499.
19. Wilmsen, C.W. *J. Vac. Sci. Technol.* **1981**, *19*, 279-289.
20. Massiot, D.; Farnan, I.; Gautier, N.; Trumeau, D. ; Trokiner, A. ; Coutures, J.P. *Sol. St. Nucl. Mag. Reson.* **1995**, *4*, 241-248.
21. Bovey, F. A. ; Jelinski, L.; Mirau, P.A. *Nuclear Magnetic Resonance Spectroscopy*, Academic Press, Inc.: California, 1988.
22. Chatterjee, M.; Bhattacharya, D.; Hayashi, H.; Ebina, T.; Onodera, Y.; Nagase, T.; Sivasanker, S.; Iwasaki, T. *Microporous Mesoporous Mater.* **1998**, *20*, 87-91.

23. Du, H.; Chen, J.; Pang, W.; Yu, J. ; Williams, I.D. *Chem. Comm.* **1997**, 781-782.

